STRONG MGII ABSORBERS AND THEIR RELATION TO GALAXIES

by

Lorenzo G. Rimoldini

M.S., University of Pittsburgh, 2001

Submitted to the Graduate Faculty of

the Department of Physics & Astronomy in partial fulfillment

of the requirements for the degree of

Doctor of Philosophy

University of Pittsburgh

2007

UNIVERSITY OF PITTSBURGH

DEPARTMENT OF PHYSICS AND ASTRONOMY

This dissertation was presented

by

Lorenzo G. Rimoldini

It was defended on

April 23, 2007

and approved by

David A. Turnshek, Professor and Chair, Dept. of Physics & Astronomy, UPitt

Andrew J. Connolly, Associate Professor, Dept. of Physics & Astronomy, UPitt

Rupert A.C. Croft, Associate Professor, Dept. of Physics, CMU

Donna L. Naples, Associate Professor, Dept. of Physics & Astronomy, UPitt

Sandhya M. Rao, Research Associate Professor, Dept. of Physics & Astronomy, UPitt

Ravi K. Sheth, Associate Professor, Dept. of Physics & Astronomy, UPenn

Dissertation Advisors: David A. Turnshek, Professor and Chair, Dept. of Physics & Astronomy, UPitt,

Ravi K. Sheth, Associate Professor, Dept. of Physics & Astronomy, UPenn

ABSTRACT

STRONG MGII ABSORBERS AND THEIR RELATION TO GALAXIES

Lorenzo G. Rimoldini, PhD

University of Pittsburgh, 2007

The largest catalog of strong MgII absorbers to date derived from the Sloan Digital Sky Survey (SDSS) quasar spectra was employed to describe statistical properties of absorbers and their clustering along sight lines as a function of redshift and rest-equivalent width (REW). The association of SDSS galaxies with MgII systems was investigated by cross-correlating the spectroscopic MgII catalog with the imaging catalog of galaxies surrounding quasar sight lines. The quasar-galaxy cross-correlation was estimated for various subsets in redshift, REW, and magnitude intervals as a function of impact parameter from quasar sight lines. The distribution of luminosities of MgII-absorbing galaxies was described using a background subtraction method. Photometric properties of absorbing galaxies, such as colors and integrated fluxes in various bands, were analyzed as a function of REW. An analytical model for the absorbers was developed and constrained by the statistical properties of the MgII catalog and observational features of high-redshift galaxies from the Hubble Ultra Deep Field (HUDF), which were also employed to determine the evolution of absorption cross-section.

Clustering was detected for absorbers separated by less than $\sim$500 km s^{-1}, with indications of a stronger signal at larger REW and growing clustering at lower redshift. An anti-correlation feature was found at absorption pair separations of about 10^3 km s^{-1}. The shallow nature of SDSS galaxy imaging limited the analysis of MgII-galaxy associations to lower redshift absorbers and only the bright end of the luminosity distribution of absorbing galaxies was recovered. The quasar-galaxy cross-correlation showed evidence for a MgII-

galaxy association and was stronger and steeper at small impact parameters for larger REW absorption lines. Stronger absorbers were found to be associated with bluer and less luminous galaxies, while weaker systems were associated with redder and more luminous galaxies. The cross-section of absorbers inferred from the distribution of HUDF galaxies confirmed smaller impact parameters and increasing evolutionary effects for stronger absorbers. Modeling absorbers indirectly via HUDF galaxies led to a versatile tool able to guide measurements toward a deeper understanding of the origins of MgII absorption.

TABLE OF CONTENTS

LIST OF TABLES

LIST OF FIGURES

PREFACE

This thesis would not have been possible without the contribution from many people. I am thankful to Dave Turnshek for suggesting the topic and indicating possible routes of investigation, Ravi Sheth for his theoretical insights and helpful advices on many subjects, Sandhya Rao for her careful reading and commenting, Andy Connolly, Rupert Croft, and Donna Naples for their constructive suggestions. I thank Dan Nestor for assisting with his MgII-detection routine and its results, Anna Quider for going through several thousands of spectra meticulously leading to a reliable MgII catalog, and Ewan Cameron for sending his photometric redshifts and absolute magnitudes of HUDF galaxies. I am grateful to Voica for brightening up the whole way and sharing all these years with a positive perspective.

1.0 INTRODUCTION

1.1 ABSORPTION LINES IN QUASAR SPECTRA

Quasi-stellar object (QSO), or quasar, spectra offer unique opportunities to probe the gaseous content of the Universe. The large luminosities of QSOs ($\sim$10–100 times the luminosity of our Galaxy) emitted from regions as compact as our Solar System make them among the most distant objects detected. Intervening matter along lines-of-sight (LOS) to QSOs is detected in the form of absorption lines in QSO spectra, which contain information on metal abundances, physical conditions, and the kinematic properties of the interstellar and intergalactic gas within a wide range of environments and as a function of cosmic look-back time.

Detection of gaseous structures in absorption is independent of the luminosity of the intercepted medium, enabling us to reach much greater depths than imaging observations with similar integration times and to study low-density gas which may not be detectable by any other technique. Flux-limited imaging is subject to selection effects due to surface brightness limitations and k-corrections, and only the most luminous objects can be described at large distances, while objects detected in absorption is based on gas cross-section selection.

Some of the biases and restrictions involved in luminosity-limited observations do not apply to absorption lines, but others are introduced, including dependence on the QSO brightness, spectral resolution, range, and sensitivity. But the most important limiting factor lies on sampling only a one dimensional pencil beam towards background QSOs.

By studying absorption environments at lower redshifts, the connection between absorption and galaxy properties (like luminosity, impact parameter, redshift evolution, morphology, metal abundance, star formation, etc.) can be investigated. The understanding of the

role of gas associated with galaxies at low redshifts may then be extrapolated to higher redshifts and integrated into the more global context of galaxy formation and evolution.

1.1.1 Absorption Line Profile

When a parcel of gas at redshift z_{abs} is intercepted by the LOS to a QSO, it absorbs flux from the QSO continuum at wavelength λ_{rest} corresponding to a particular energy-level transition, and the absorber is detected at $\lambda_{obs} = \lambda_{rest}(1 + z_{abs})$.

In principle, the shape of an absorption line can be described in terms of a Voigt profile, obtained by convolving the Lorentzian natural (quantum-mechanical) broadening with a Gaussian Doppler broadening. The contribution by collisional broadening is neglected because of the extremely rarified gas in interstellar and intergalactic media. Thus, the core of the line profile is Gaussian, while the far wings are Lorentzian. The Gaussian contribution arises from the convolution of broadening from the thermal Maxwell-Boltzmann distribution and a turbulent component. Both kinematic contributions may be characterized by a Doppler parameter b, resulting from the sum in quadrature of the thermal $b_{therm} = v_{rms}\sqrt{2} = \sqrt{2k_BT/m}$ (where k_B is Boltzmann constant, T denotes the temperature of the gas, and m represents the mass of the atom) and turbulent b_{turb} components: $b^2 = b_{therm}^2 + b_{turb}^2$. Finally, the measured absorption profile is a convolution of the Voigt profile with the instrumental broadening (usually assumed Gaussian as well) [Petitjean 1998, Charlton et al. 2000].

An absorption line may be characterized in a very concise way by a single parameter, independent of the actual line profile or spectral resolution: its rest equivalent width (REW). The REW represents the width of an equivalent line with an inverted top-hat profile (with intensity changing suddenly from the continuum level to zero throughout, as shown in Fig. 1.1) such that it removes the same amount of rest-frame energy from the continuum as the observed absorption line. Since the energy removed from a line is $E = \int(I_c - I_\lambda)d\lambda$ and it identifies the area between the measured spectral intensity I_λ and the fitted continuum level interpolation at that wavelength I_c, dividing E by I_c equals the width of the rectangular area enclosed by the inverted top-hat profile. Thus, the REW of an absorption at redshift

z_{abs} can be expressed in terms of the integral of the normalized line profile at rest, or as a function of the optical depth, as follows:

$$\mathrm{REW} = \frac{1}{1+z_{abs}} \int \left(\frac{I_c - I_\lambda}{I_c} \right) d\lambda = \frac{1}{1+z_{abs}} \int \left(1 - e^{-\tau_\lambda} \right) d\lambda, \tag{1.1}$$

where the optical depth τ_λ results from the product of the column density N and the absorption coefficient α_λ: $\tau_\lambda = N\alpha_\lambda$.

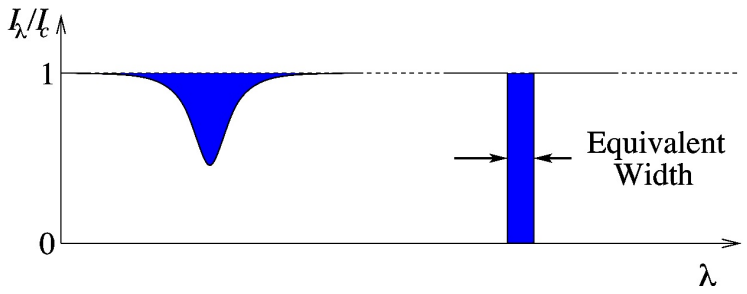

Figure 1.1: The equivalent width of an absorption line equals the amount of energy absorbed by the line (identified by the area filled in blue) divided by the spectral intensity I_c of the continuum level at the absorption wavelength.

The relationship between REW and column density N is described by the so-called curve of growth. Generally, three regimes are identified:

(i) **Linear regime:** For optically thin absorbing gas ($\tau \ll 1$), the flux absorbed by the line increases linearly with N, i.e., $REW \propto N$. As N increases, the optical depth increases as well, until all of the photons at the core of the line are removed (when the absorption profile saturates).

(ii) **Logarithmic or saturated regime:** When the gas is sufficiently dense to saturate the absorption (with $10 < \tau < 10^3$), damping wings of the Lorentzian profile are negligible with respect to the Gaussian Doppler and turbulent contributions. The dependence of REW on N is very weak (logarithmic), since only atoms in the tail of the velocity distribution define the width of the absorption profile. Thus, the REW is roughly proportional to the velocity dispersion of the gas: $REW \propto b\sqrt{\ln(N/b)}$.

(iii) **Square root or damped regime:** At even higher column densities ($\tau > 10^4$), line profiles develop strong and broad damping wings (from natural broadening) which dominate the absorption, and the REW increases as the square root of N: $REW \propto \sqrt{N}$. Practically, only the Lyman-α transition is observed in this regime (such as in damped Lyman-α systems).

For N(MgII) $> 10^{14}$ atoms cm^{-2}, MgII absorption lines become saturated and the Voigt profile is dominated by kinematic contributions. As described above, in this regime the line-of-sight velocity dispersion of multiple MgII subcomponents is responsible for most of the absorption, and MgII column densities cannot be measured accurately.

1.2 MGII ABSORBERS

Magnesium is an α-group element synthesized primarily by Type II supernovae in the earliest stages of stellar evolution, when most massive stars form and quickly evolve toward their violent end, and it is not produced significantly in secondary or later stages. Thus, it is expected to be associated with galaxies up to the highest redshifts, with no further build up over cosmological time scales.

Observational evidence has led to a general consensus on the connection between metal absorbers and galaxies, but the exact relation between absorption properties and the physical origin, distribution, and kinematics of the absorbing gas is still uncertain.

This thesis involves the study of strong MgII absorbers. The MgII doublet transition at rest wavelengths $\lambda\lambda$2796, 2803 AA is easy to identify, and strong absorbers are defined by rest-frame equivalent widths (REW) of the 2796 Å component greater than 0.3 Å. Historically, this threshold arose as a consequence of observational sensitivity [Steidel & Sargent 1992], but it also roughly corresponded to the transition point between optically thin and optically thick HI column densities [Rigby et al. 2002]. MgII absorbers with REW greater than 0.3 Å were found to trace HI column densities greater than 3×10^{17} atoms cm^{-2} [Churchill et al. 2005]. Such regions are opaque ($\tau > 1$) below the Lyman limit, because N(HI) is large enough to absorb all photons capable of ionizing HI (i.e., with $\lambda_{rest} < 912$ Å).

MgII arises in structures spanning at least six decades of HI column density (for $N(\mathrm{HI}) \sim 10^{15.5} - 10^{21.5}$ atoms cm^{-2}) [Rao 2005, Bergeron & Stasinska 1986, Steidel & Sargent 1992, Churchill et al. 2000a]. Because of the low ionization level of MgII, it is expected to trace typical neutral hydrogen column densities associated with galaxies. Indeed, a one-to-one correspondence was observed between optically thick HI and strong MgII systems. In particular, MgII absorbers with REW>0.6 Å were shown to be good tracers of particularily large $N(\mathrm{HI})$ densities, like those involved in damped Lyman-α systems [Chen 2005, Rao 2005, Chen & Lanzetta 2003, Rao et al. 2003, Rao & Turnshek 2000] (corresponding to $N(\mathrm{HI}) > 2 \times 10^{20}$ atoms cm^{-2}). By probing such a wide range of galactic environments, the potential value from understanding the physical properties of MgII absorbers is enhanced, but at the same time disentangling correlations between absorption properties and galaxy properties constitutes a complex task.

Weak MgII systems (with REW<0.3 Å) are found to generally correspond to sub-Lyman limit systems with $N(\mathrm{HI}) < 6 \times 10^{16}$ atoms cm^{-2} and show single absorption lines, although a few have multiple components spreading over 10–100 km s^{-1} [Churchill et al. 2005]. Initially, imaging work failed to identify galaxies at the absorption redshift, suggesting that weak absorption could possibly be due to tidally stripped material, extragalactic clouds, low surface brightness galaxies [Churchill et al. 1998], dwarf galaxies [Zonak et al. 2004], failed galaxies, pre-galaxy fragments, remnant material left over from the formation of galaxies, or intergalactic star-forming pockets [Rigby et al. 2002]. However, recent Hubble Space Telescope images of MgII absorbing galaxies indicated that normal galaxies were associated with weak absorption lines over a wide range of impact parameters [Churchill et al. 2005]. Extrapolating the galaxy luminosity vs. halo radius relation derived for strong absorbers to small REW (see Eq. 1.2, assuming each galaxy is surrounded by a galactic halo with unitary filling factor), the observed incidence of weak MgII systems implies that gaseous halo radii are about twice as large as for strong absorbers (e.g., [Churchill et al. 2005]). Alternatively, weak absorbers might be associated with a population of dwarf galaxies [Petitjean 1998].

1.2.1 Historical Background

The study of the relation between galaxies and QSO absorbers (suggested to arise in large gaseous halos around galaxies [Bahcall & Spitzer 1969]) began with the investigation of MgII systems, mostly for practical reasons. The near-UV MgII $\lambda\lambda$2796, 2803 Å is one of the longest-wavelength resonance transitions among the dominant ions in HI gas, allowing ground-based detections at redshifts $z > 0.11$, and thus follow-up imaging of neighboring galaxies. However, more recently the Hubble Space Telescope has been used to probe MgII at redshifts lower than 0.1 as well [Churchill 2001].

Initial surveys of the statistical properties of strong MgII absorbers found marginal or no evolution in the number density (per unit redshift) of absorbers in redshift ranges 1.25–2.15 [Lanzetta et al. 1987] and 0.2–1.5 [Tytler et al. 1987, Sargent et al. 1988b], respectively. Also, no evidence for evolution of the absorption REW was found. A later study on a larger set of 107 strong systems within the redshift range 0.23–2.06 [Steidel & Sargent 1992] provided the largest systematic survey until the advent of the Sloan Digital Sky Survey (SDSS). Evidence for evolution of the number density of absorbers was found only for the very strongest ones, decreasing faster than the non-evolutionary case with decreasing redshift (i.e., the mean REW increased with redshift).

The first galaxies responsible for metal absorbers were identified by imaging fields around QSOs with MgII detections, measuring redshifts of nearby galaxies and matching them to the absorption redshift [Boksenberg & Sargent 1977, Bergeron 1986a, Bergeron et al. 1987, Cristiani 1987, Bergeron & Boissé 1991]. From a sample of 58 MgII detections, a normal bright $\sim L_*$ galaxy (with morphology drawn from a variety of types) was found within sky-projected distances $\sim$ 50 kpc[1] from the QSO sight-line [Steidel et al. 1994, Steidel 1995]. Galaxies clustered around QSOs were excluded from consideration because of possible clustering between QSOs and galaxies, and the possibility that galactic gaseous halos could be stripped away by tidal interactions or become highly ionized as a result of the proximity effect [Steidel 1993]. The covering factor of the gas was found to be near-unity, and the projected cross-section radius R of gas scaled weakly with the galaxy K-band luminosity

[1]Throughout this thesis, a standard ΛCDM cosmology is assumed, with $\Omega_M = 0.3$, $\Omega_\Lambda = 0.7$, and Hubble constant $H_o = 70$ km s^{-1} Mpc^{-1}.

L_K. Assuming a Holmberg-like relation [Holmberg 1975] and minimizing the number of absorbing galaxies at impact parameters greater than $R(L)$ and non-absorbing ones closer than $R(L)$, it resulted:

$$R(L_K) \approx (50 \text{ kpc})(L_K/L_{K,*})^{0.15}. \tag{1.2}$$

The galaxy gaseous halos were several times larger than the typical optical (Holmberg) sizes of the galaxies, while the mean rest-frame luminosity of absorbing galaxies was found to be about $0.5L_{K,*}$ and $0.7L_{B,*}$, in a sample including K-band luminosities as faint as $0.05L_{K,*}$ (with $L_{K,*}$ corresponding to absolute magnitudes $M_{K,*} \sim 25$). Other studies confirmed that absorbing galaxy morphologies and luminosities varied greatly, from sub-L_* to L_* galaxies [Le Brun et al. 1997, Rao et al. 2003] and included low surface brightness galaxies [Bowen et al. 2001].

While the above mentioned works [Steidel et al. 1994, Steidel 1995] initiated a statistical description of the association of MgII absorbers with galaxies, some of its assumptions and methods were later considered too simplistic. In particular, the identification of absorbing galaxies as only the nearest ones, the incompleteness of spectroscopic redshifts of galaxies in absorbing fields, and their pre-selection based on colors (consistent with the absorber redshift) could have missed potential absorbing galaxies at both small and large impact parameters [Bowen et al. 1995].

From semi-analytic and Monte Carlo modeling [Lin & Zou 2001] it was argued that selection effects (especially the apparent magnitude limit) were responsible for weakening the R–L_K dependence by roughly a factor of two in the power law index of Eq. 1.2. Different selection criteria of candidate absorbing galaxies for spectroscopic follow-up were believed to have played a role in the much larger impact parameters (∼100 kpc) reported by an analysis of the same class of absorbers [Churchill et al. 2005]. Indeed, the identification of galaxies responsible for absorption depended on several factors, including the imaging depth, galaxy clustering, geometry and kinematic properties of absorbing galaxies as well as metal-enriched gases. Moreover, evidence for galaxy groups was found in several cases [Churchill et al. 2005], while [Steidel et al. 1994, Steidel 1995] considered only the nearest galaxy with redshift matching that of the absorption.

More recently, [Tripp & Bowen 2005] pointed out that the evaluation of the covering

factor could be biased by searching for absorbing galaxies near QSO sight-lines where MgII absorbers were already detected. After measuring the redshift of a sample of 30 galaxies in the redshift range 0.31–0.55 and with impact parameter up to ∼50 kpc from bright SDSS QSOs (with $g < 20$), it was found that half of the QSO spectra showed no MgII absorption at the redshifts of the intercepted galaxies [Tripp & Bowen 2005]. This result was thought to indicate that MgII absorbing gas was not distributed smoothly around galaxies, favoring the idea of patchy gaseous cross-sections, consistently with other recent findings from high quality Hubble Space Telescope images of absorbing galaxies [Churchill et al. 2005]. Such a scenario could arise naturally from gas stirring, e.g. as a consequence of gravitational interactions among galaxies (see § 1.2.2), matching the more familiar patchy distribution of the small interstellar clouds in our own Galaxy (e.g., [Tripp & Bowen 2005]).

It is intriguing that that prior knowledge of the existence of an absorber enhances relevantly the likelyhood to find the absorbing galaxy, while the converse does not always hold. In fact, optical and infrared colors of absorbing galaxies and their spectra suggest they cover the whole range of spectroscopic types, which rules out simple selection criteria. Future studies are expected to investigate possible environmental dependences in more detail (e.g., galaxies embedded in a hot intracluster gas may host mostly highly ionized halos, or their gas content may be stripped by intracluster ram pressure), as well as compare the properties of absorbing and non-absorbing galaxies (say within 50 kpc).

An inverse correlation between REW and the impact parameter between the QSO sight-line and the absorbing galaxy centroid was noted for absorbers with REW$>$ 1 Å [Steidel 1995, Lanzetta & Bowen 1990], though most of the trend was attributed to damped Lyman-α absorbers (which constituted most of the galaxies detected at small impact parameter).

While average colors of absorbing galaxies appeared to be consistent with present-day intermediate type galaxies (such as Sb spirals), it was suggested that global colors arose from the superposition of red passive and blue star-forming galaxies, associating red and blue galaxies with weaker and stronger absorbers than REW∼1 Å, respectively [Zibetti et al. 2007]. Also this study found that stronger systems were significantly more concentrated at smaller impact parameters with respect to weaker ones. As a consequence, it was speculated that scenarios involving metal-enriched gaseous outflows from star-forming

galaxies were favored. In fact, high-speed winds in the neighborhood of starbursting regions, leading to large kinematic Doppler broadening in blue and small cross-section environments (as observed in strong absorbers), were believed to evolve in less energetic outflows encompassing larger cross-sections around older and thus redder galaxies (consistently with the weaker absorption findings). The interpretation of absorption strength varying as a function of galaxy evolution was supported by indications that absorbing galaxies spanned the full range of spectroscopic types.

Models involving gas infall (e.g., [Mo & Miralda-Escude 1996]) onto massive and passively evolving galaxies were disfavored because of the peculiar star-formation history which would follow in order to reproduce the observed MgII environment [Zibetti et al. 2007]. Also, accretion scenarios predicted that the comoving number density of absorbers declined at high redshift, when typical halo masses were smaller than those required for strong MgII absorbers ($\sim 10^{12} M_{\odot}$ owing to [Mo & Miralda-Escude 1996]), but this trend disagreed with observational results [Nestor et al. 2005a, Prochter et al. 2006]. However, it is important to remember that the accretion model [Mo & Miralda-Escude 1996] addressed mostly MgII absorbers with REW$\sim$ 0.3 Å, so mixed scenarios for strong absorbers cannot be ruled out.

It was suggested that merger-driven starburst activity could provide a better match to observational results [Prochter et al. 2006], especially if the galaxy merger rate evolved as indicated by a recent study using spectroscopic galaxy redshifts [Lin et al. 2004]. However, the evolution of statistical properties of absorbers is expected to arise from a combination of numerous processes, including growth of structures, star formation, galaxy evolution, kinematics, mergers, outflows on galactic scales, which should all be considered in order develop a consistent model for MgII absorbers.

1.2.2 Kinematic Structure of Absorbers

MgII absorption profiles arising from systems rich in HI (such as damped Lyman-α) are fully saturated, generally span a kinematic range between 100–200 km s^{-1}, and they rarely present any velocity substructure (e.g., [Churchill et al. 2005]). At lower HI column densities (but still greater than 3×10^{17} atoms cm^{-2}, i.e., for Lyman-limit systems), MgII profiles at high

resolution show complex substructures with kinematic spreads of the order of 50–400 km s^{-1}.

As described in § 1.1.1, the REW of strong MgII systems is characterized mostly by the velocity spread of the absorbing gas, which is expected to depend on both galaxy velocity dispersion and kinematic model of the absorbers (as explained in § 1.2.2.1). Simple models adopted to interpret the kinematics of MgII absorbers so far included an extended spherical halo (arising from either galactic-scale outflows or gas accretion in galactic halos of massive galaxies [Lanzetta & Bowen 1990, Bergeron & Boissé 1991, Steidel 1993, Steidel 1995, Mo & Miralda-Escude 1996]) or a component with disk-like geometry (motivated by the gaseous rotating disks of spiral galaxies [Charlton & Churchill 1998, Charlton & Churchill 1996, Bowen et al. 1995]). A combination of both contributions is expected to explain the ensemble of observed line profiles [Charlton & Churchill 1998].

1.2.2.1 Radial and Rotational Kinematics

Radial and rotational motions of absorbing clouds give rise to different velocity spreads, even if embedded within similar galactic potential wells. If absorption profiles are observed at high spectral resolution, differences in their pattern may be appreciated as well. When lines-of-sight intercept gaseous halos with clouds moving radially, both redshifted and blueshifted absorption lines occur with respect to the halo rest-frame, forming double-peak profiles spreading over velocity ranges of the order of velocity dispersions of the galactic halos (or even more, if cloud motions are not achieved purely gravitationally, as for supernova-driven winds). Instead, sight-lines passing through rotating disks intercept kinematic spreads almost an order of magnitude smaller (speculated typically within 20–60 km s^{-1} [Charlton et al. 2000]), either redshifted *or* blueshifted.

Early results [Lanzetta & Bowen 1992] based on smaller and more incomplete samples suggested that small impact parameters corresponded to disk-like rotation kinematics, while large impact parameters indicated infall-like motions. A later study [Churchill & Vogt 2001] of high resolution spectra of 23 strong MgII absorbers over the redshift range 0.4–1.2 showed that absorption profiles were broken up into multiple components, characterized by dominant subsystems (with REW>0.2 Å and velocity spreads of a few tens of km s^{-1}) accompanied by significantly weaker subsystems separated up to 400 km s^{-1} from the dominant one.

Despite the variety of absorption profiles within each sight-line, it was noticed that the distribution of small subsystems around the strongest one was often asymmetric. Then, [Churchill & Vogt 2001] speculated that sight-lines passing through rotating disks gave rise to dominant components (with velocity offsets depending on disk orientations), while weaker subcomponents arose from clouds randomly distributed in the halo.

A subsequent analysis by some of the same authors found no clear connection between gas velocity spread and the orientation of galaxies with respect to sight-lines [Churchill et al. 2004, Churchill et al. 2005]. However, absorption properties were correlated to the level of asymmetry in galaxies, suggesting that gravitational disturbances (like mergers) could be responsible for more chaotic absorbing gas kinematics.

Mergers might trigger starburst events leading to ionized winds by shock-heating during the interaction [Cox et al. 2004]. Such scenarios would also be consistent with the large variety of the properties of galaxies and the difficulty of finding systematic trends with absorption properties [Churchill et al. 2000b]. Evidence for interacting galaxies arose also from the analysis of ultra-strong MgII absorbers (with REW>4 Å) detected in SDSS QSO spectra at sufficiently low redshifts to permit direct study [Nestor et al. 2005b, Nestor et al. 2007].

1.2.2.2 Galactic Outflows

When high resolution spectra revealed pairwise symmetries in MgII absorption profiles with several hundred km s^{-1} velocity spread, it was speculated that galactic-scale outflows of gas (or "superwinds") powered by massive stars through correlated supernova explosions and stellar winds were responsible for the observed absorption features [Bond et al. 2001, Ellison et al. 2003]. Large scale outflows associated with such winds were expected to occur in a variety of environments including Lyman break galaxies [Pettini et al. 2001, Pettini et al. 2002], high-redshift galaxies (because of the magnification from strong gravitational lensing [Frye et al. 2002]), and local starburst galaxies [Heckman et al. 2000].

Superbubbles are believed to form from star formation activity in starburst galaxies and sweep-up interstellar gas as they expand (e.g., [Mac Low & McCray 1988]). If they are sufficiently energetic (or are nested in a shallow potential well) and succeed to reach the galactic halo, the expanding shells fragment as a consequence of Rayleigh-Taylor insta-

bilities and a bipolar outflow of hot material forms in the halo [Tomisaka & Bregman 1993, Suchkov et al. 1994, Strickland 1998, Tenorio-Tagle & Munoz-Tunon 1998]. Terminal velocities of superwinds are estimated of the order of 400–800 km s^{-1} [Heckman et al. 2000], comparable with or exceeding the escape velocity from L_* dwarf galaxies. Also, outflow speeds in the range of 10^2–10^3 km s^{-1} were implied by detections of interstellar metal absorption in local starburst galaxies [Phillips 1993, Lequeux et al. 1995, Heckman & Leitherer 1997, Sahu & Blades 1997, Kunth et al. 1998, Gonzalez-Delgado et al. 1998].

While the central engine of the superwind reaches very high temperatures ($\sim 10^7$ K) leading to x-ray emissions and highly ionized gases, the edges of the outflow are expected to have temperatures of the order of 10^4 K and so able to host low-ionization absorbers [Heckman et al. 2000], including MgII systems. Metals entrained by superwinds include those produced by supernova activity as well as previously existing ones. The multicomponent absorption troughs observed in strong MgII absorbers [Churchill & Vogt 2001] might result from clumping of fragments originated from Rayleigh-Taylor instabilities and such a mechanism could explain a substantial fraction of stronger absorbers [Bond et al. 2001].

While the observed symmetric pairwise structures of absorption lines at high resolution, with an inversion feature at the center of the profile, were exactly what was expected from absorbers at the edges of expanding gas shells (with little or no absorbing material moving at the systemic velocity of the wind), alternative explanations could invoke pairs of galaxies within groups or clusters, or large galaxies and their satellites [Churchill 2000].

The expected loss of metals from shallower potential wells could constitute a significant source of metal enrichment in the intergalactic medium [Madau et al. 2001, Ellison et al. 2000, Ferrara et al. 2000, Giroux & Shull 1997, Scannapieco et al. 2002, Furlanetto & Loeb 2003]. Also, winds from early generations of Population III stars at redshift $z > 10$, protogalaxies at $6 < z < 10$, and larger galaxies at $3 < z < 6$ could have contributed to the enrichment of intergalactic medium [Aguirre et al. 2001], so that in principle metal absorbers at lower redshifts might be detectable even without the presence of a galaxy at the same redshift (anymore). However, metal enrichment of galactic environments is expected to have continued till present time because of various processes, including galactic winds, tidal stripping from mutual gravitational interactions among galaxies, and ram-pressure stripping from galaxies

passing through the intracluster medium.

The large scatter observed in absorbing galaxy properties might indicate that MgII systems arose in a variety of situations, from large quiescent galaxies with gaseous clouds in their halos, to more active galaxy mergers and starburst events leading to galactic-scale outflows and fountains. A further complication concerning velocity separations greater than ~ 200 km s^{-1} is due to the contribution of the large-scale spatial distribution, so that the velocity spread of absorbers arises from both peculiar velocities and structures at different cosmological redshifts [Shi 1995, Crott et al. 1997].

1.2.3 MgII Absorbers and the Sloan Digital Sky Survey

Direct imaging of fields around QSOs with metal absorbers may provide detailed features of absorbing galaxies, but it is an expensive process usually limited to tens of selected systems. The statistical significance of results on MgII absorbers increased steeply with the advent of the SDSS, from the Early Data Release [Nestor et al. 2005a] to the Third Data Release [Prochter et al. 2006]. Indeed, the ambitious goal of measuring 10^5 QSO spectra opened a new era for QSO absorption-line statistics, especially for those metal systems whose statistical properties were hindered by low number counts.

This thesis took advantage of a MgII absorber catalog extracted from the Fourth Data Release [Adelman-McCarthy et al. 2006], leading to sample sizes about two orders of magnitude larger than those available from pre-SDSS MgII surveys. Such a wealth of data made it possible to investigate further the nature of MgII absorbers and test possible relations between absorption properties and galaxy properties.

The MgII-investigation capabilities of the SDSS data set were limited by mostly the following reasons:

(i) The spectral resolution of QSOs allowed only the detection of several absorption profiles blended together: only strong doublets were identified and kinematic details of the absorbers could not be addressed;

(ii) The SDSS imaging was too shallow for a proper assessment of galaxies associated with MgII absorbers.

On the other hand, the large MgII-sample size allowed to achieve unprecedented accuracy in the measurement of absorber number density as a function of redshift and REW, as well as study the clustering signal of absorbers in redshift and REW intervals (see Chapter 2). Moreover, average galaxy distribution and photometric properties were derived for a subset of absorbers at lower redshift, and some galaxy properties (such as impact parameter, luminosity, and color) were related to the absorption REW (see Chapter 3).

In order to fully exploit the statistical results achieved from the MgII catalog, the SDSS galaxy imaging was complemented by the deepest galaxy imaging to date — the Hubble Ultra Deep Field (see Chapter 4), which allowed to derive the evolution of absorbing halo cross-sections and constrain properties of a new statistical model.

A detailed summary of results from Chapters 2, 3, and 4 is presented in the concluding Chapter 5, which further outlines future prospects by improving analysis methods and extending them to new data sets.

2.0 MGII ABSORBERS IN QSO SPECTRA FROM THE SLOAN DIGITAL SKY SURVEY

This Chapter begins with a description of the sample of SDSS QSOs adopted for the analysis in § 2.1. The detection procedure of MgII absorbers is outlined, and the absorption catalog is presented. The absorber number density as a function of REW and redshift is computed and compared with previous results. In § 2.2, the distribution of absorption pairs along QSO sight-lines with multiple MgII detections is studied by evaluating the two-point correlation function for different REW and absorption redshift intervals.

Over the last few years, the Sloan Sky Digital Survey (SDSS) has increased the number of known QSOs with spectroscopy of sufficient quality to study QSO absorption lines by more than two orders of magnitude. The fourth Data Release (DR4) [Adelman-McCarthy et al. 2006] of the SDSS imaged 180 million objects within 6670 square degrees in five bandpasses, u, g, r, i, z, spanning the wavelength range from 3,000 to 10,000 Å [Fukugita et al. 1996]. The magnitude limits for 95% completeness for point sources in typical seeing were 22.0, 22.2, 22.2, 21.3, and 20.5, for the u, g, r, i, z bands, respectively. The median PSF width was 1.4 arcsec in the r–band, and the positions of most objects were accurate to better than 0.1 arcsec rms in each coordinate [Pier et al. 2003].

Spectroscopic targets were selected from the imaging data over 4783 square degrees, covering the wavelength range from 3800 Å to 9200 Å at a spectral resolution $R = \lambda/\Delta\lambda$ from 1800 to 2100 (with λ denoting the observed wavelength and $\Delta\lambda$ the full width at half maximum of the spectrograph line spread function). Optical fibers with diameter of 3 arcsec were used, and no objects closer than 55 arcsec from each other could be targeted on the same plate (only plate overlapping regions could host spectroscopy of closer pairs). Almost 850,000 spectra were processed by the SDSS DR4 spectroscopic pipeline, which

performed wavelength and flux calibration (with uncertainties of about 0.05 Å and 5%, respectively), subtracted sky emission, removed atmospheric absorption bands, and corrected for the Doppler shift due to the Earth's heliocentric motion. The QSO sample was selected by colors (see [Richards et al. 2002]) as well as point source matches to FIRST radio sources, and it included 76,483 spectra with emission redshifts up to ∼6.

2.1 MGII ABSORBERS FROM SDSS DR4 QSOS

2.1.1 The QSO Sample

SDSS DR4 QSOs were reduced by the SDSS spectroscopic and photometric pipelines and retrieved by querying the SDSS data archives. For this thesis, the photometry and redshift of QSOs were extracted from the SDSS table SpecPhoto, a joined view of spectroscopic and photometric objects that had clean spectra and included only the best version of duplicated objects. Also, this table contained up-to-date data-derived values as algorithms were improved (unlike SpecObjAll table). In order to limit noise effects and facilitate follow-up observations from ground-based telescopes, we required the i-band fiber magnitude to be brighter than 20. Excluding QSOs at redshifts lower than 0.36 (since no MgII systems could be detected in that range) as well as missing or failed redshift measurements (i.e., with the zstatus flag less than 2), the total number of QSO spectra (classified in SpecClass as QSO or high-redshift QSO) amounted to 44,620. Unfortunately, 14 spectra failed some step of the normalization or the line-finding process, so they were excluded from the final sample, which reduced to 44,606 objects. This sample included the Early Data Release (EDR; see [Stoughton et al. 2002]) objects, with plate number less than 417, but not the "extra", "special" and "extra-special" plates (regarding reobservations of main survey plates, spectra beyond the main survey targets, and reobservations of the special plates, respectively). No duplicate spectra were considered and special plates were excluded because their statistical properties were different from the main DR4 sample. In fact, such plates were not aimed at producing a complete and uniform survey, and the QSO target selection algorithm was

changed [Adelman-McCarthy et al. 2006] (e.g., it included fainter objects and thus also more stellar contamination).

2.1.2 The Detection of MgII Doublets

The SDSS spectrograph wavelength coverage from 3800 Å to 9200 Å allowed in principle detection of $\lambda\lambda$2796,2803 Å MgII doublets in the redshift range from 0.36 to 2.30. The actual spectral wavelength interval within which MgII systems could be detected was further restricted depending on the redshift of the QSO, the consequent location of the Lyman α forest, general noise and instrumental effects. Detection of MgII absorbers in each QSO spectrum was bounded at lower wavelengths (and redshift) by the redshifted QSO Lyman α emission (to exclude unreliable MgII identifications within the Lyman α forest region) and at higher wavelengths (and redshift) by the redshifted QSO MgII emission. In order to avoid detection of systems in the spectrum associated with the QSO, only MgII absorbers 3000 km s^{-1} blueward of the QSO MgII emission were considered; the same separation redward of the QSO Lyman α emission was applied. Within the allowed spectral range, the MgII detectability depended on noise levels. MgII doublets were deemed detected when the 2796 Å and 2803 Å line components were identified with a 5-σ and 3-σ or greater significance level, respectively.

The MgII doublet detection from SDSS DR4 QSOs (pursued by Turnshek, Nestor, Rao, and Quider) used the same algorithm already applied to the SDSS EDR [Nestor et al. 2005a], though strong absorbers were measured more accurately in the DR4 catalog. The first step involved computing the redshift path-length as a function of REW detection threshold and redshift. Then, absorption line candidates with the MgII doublet separation were identified, and only those doublets which satisfied the signal-to-noise levels requirements as described above and a reasonable doublet ratio (generally between 1 and 2) were accepted. Confirmation or rejection of MgII candidates was performed interactively, in order to account for QSO broad absorption line regions (excluded from the MgII search), other absorbers (like CIV and NV) whose line splittings might become similar to that of MgII by convolution with noise spikes unfortunately located near absorption features, and checks with other metals at

the same redshift of the MgII candidate.

Particular attention was given to systems that were not well fitted by a single Gaussian. Most of such cases were resolved by fitting the absorption profile with two Gaussians, while many of the very strongest absorbers (with REW>3.8Å) were described in terms of multiple Gaussians. The multiple components were just meant to describe the absorption profiles more accurately and give a more reliable measurement for the REW – they did not necessarily correspond to the number of physical subcomponents blended together. Due to the SDSS resolution, MgII systems separated by less than about $c\Delta\lambda/\lambda \sim 150$ km s^{-1} (from ~ 140 km s^{-1} to ~ 170 km s^{-1} at $\lambda \sim 9200$ Å and $\lambda \sim 3800$ Å, respectively) could not be distinguished, and significant line-blending might affect the detection completeness of systems pairs up to a few hundreds of km s^{-1}. The closest pair of MgII systems detected was separated by $c\Delta z_{abs}/(1+z_{abs}) \sim 130$ km s^{-1} (corresponding to $\Delta z_{abs} \sim 0.001$ at $z_{abs} \sim 1.2$), just under the minimum threshold expected from the instrument on average. Finally, note that all of the REWs quoted in this thesis refer to the 2796 Å component of the doublet.

2.1.3 The MgII Catalog

On average, at least one MgII system was detected in approximately one out of four QSO spectra, leading to a total of 14,536 MgII absorbers in 11,139 QSO sight-lines. Spectra of 33,467 QSOs had no MgII absorbers, including many with very small searchable path because of low signal-to-noise or small QSO redshift. In other spectra, one or more absorbers were found — as shown in Fig. 2.1, 1, 2, 3, 4, 5, 6 MgII absorbers per line-of-sight were detected in 8475, 2088, 449, 100, 24, 3 spectra, respectively.

The redshift of detected MgII absorbers spanned an interval from 0.367 to 2.281, while the measured REW ranged from 0.16 Å to 8.5 Å. The incidence of absorbers decreased with increasing REW roughly continuously until REW$\sim$ 6.34 Å; one more system was added with REW$\sim$ 8.5 Å. The latter was considered as one system though there were indications of three components blended together, with REW 1.5 Å, 3.8 Å, and 4.5 Å at redshift 1.866, 1.874, and 1.879, respectively. The distribution of MgII detections as a function of REW and are shown by the histograms in Fig. 2.4 and Fig. 2.7, respectively.

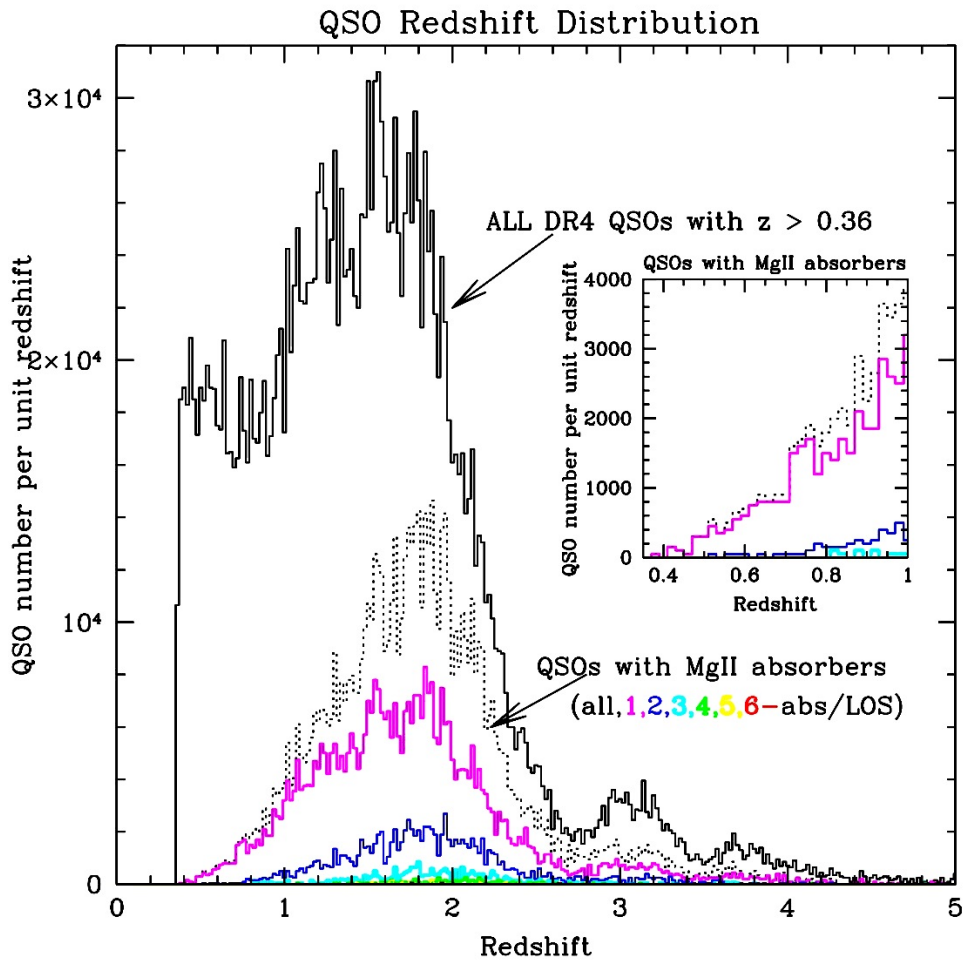

Figure 2.1: The solid black histogram shows the redshift distribution of 44,606 SDSS DR4 QSOs with redshift greater than 0.36 and i-band fiber magnitude brighter than ~ 20. The redshift distribution of 11,139 QSOs with 14,536 MgII detections is dashed, while subsets containing different number of absorbers per line-of-sight are color coded as indicated in the Figure, and include 8475, 2088, 449, 100, 24, 3 QSO spectra with only 1, 2, 3, 4, 5, 6 MgII absorbers per line-of-sight, respectively.

2.1.4 Number Density Distribution as a Function of REW and Redshift

In order to derive the true incidence of absorbers from the observed one, the sensitivity of the survey as a function of redshift and REW was evaluated. Possible sources of selection bias were considered first, since they might improperly lead to inclusion/exclusion of QSOs in/from the sample under consideration, thus altering the apparent incidence of absorbers.

The statistical bias due to gravitational lensing of background QSOs by intervening absorbers was neglected, following the conclusions of an analysis performed on MgII absorbers from the SDSS DR3 [Prochter et al. 2006] and DR4 [Ménard et al., in prep.], which detected no brightening of absorbing QSOs with respect to non-absorbing QSOs in different REW intervals.

An opposite bias on QSO detection from reddening by dust in the absorber was neglected as well. In fact, the above mentioned study on DR3 QSOs reported small effects affecting the strongest absorption REW only (REW>1.8 Å), which were estimated to correspond to a color excess $E(B-V) \sim 0.01$. However, a proper assessment of the incidence of the very strongest absorbers (within more reddened QSOs) needs to account for the bias introduced by the SDSS QSO selection [Ménard et al., in prep.], which is based on color and apparent magnitude for spectroscopic follow-up [Richards et al. 2002].

2.1.4.1 Redshift Path Density

Following the formalism by [Lanzetta et al. 1987], the redshift path density $g(W,z)$ is defined as the number of lines-of-sight (LOS) along which a MgII transition at redshift z and REW greater than W can be detected. Owing to the selection criteria outlined in § 2.1.2 and denoting the REW of the λ2796 Å line by W (if not otherwise indicated), it follows:

$$g(W,z) = \sum_{i}^{N_{LOS}} H(z - z_{\min(i)})\, H(z_{\max(i)} - z)\, H[W - 5\sigma/(1+z)]\, H[W_{\lambda 2803} - 3\sigma/(1+z)], \quad (2.1)$$

where N_{LOS} is the total number of sight-lines considered from the survey, and ($z_{\min}$, $z_{\max}$) depend on the Lyman α or MgII emission of QSOs within the survey limits. Eq. 2.1 does not include the interactive adjustments described in § 2.1.2.

The resulting redshift-path density is plotted together with the observed frequency of absorbers as a function of redshift and REW in Fig. 2.2. The Figure indicates that the sensitivity of the survey generally declines with increasing redshift and decreasing REW, as reflected by the *observed* incidence.

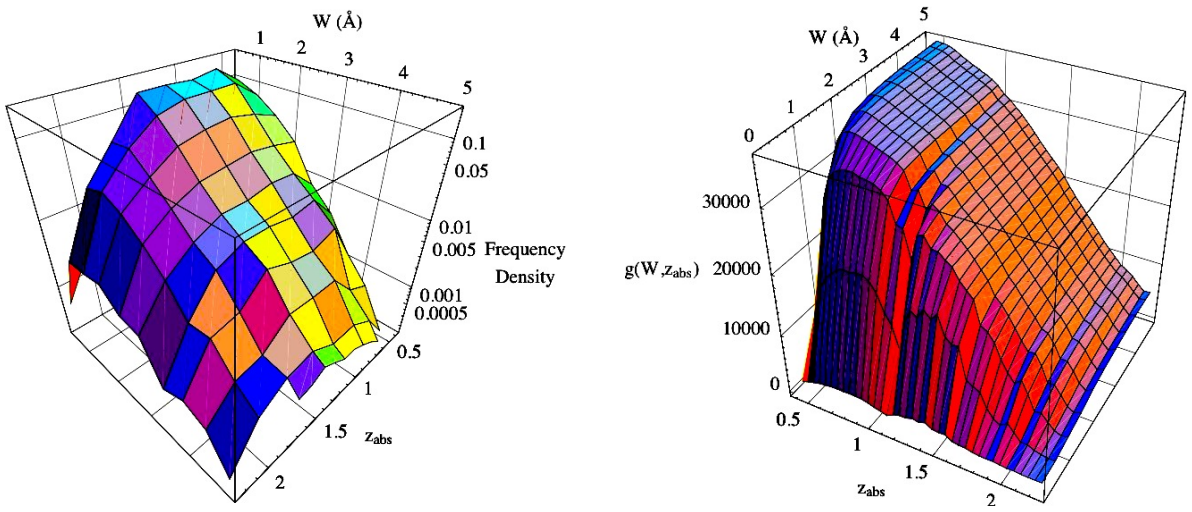

Figure 2.2: Left: Observed frequency density as a function of redshift and REW. It is binned in intervals of 0.05 and 0.5 Å, respectively, and normalized by the total number of sight-lines considered (44606). Right: The calculated redshift-path density $g(W, z)$ depicting the sensitivity of the survey as a function of redshift and REW. For a better view of some of the details, notice that z_{abs} and W axes are switched in the two panels.

The true density of absorbers (corrected by the observed redshift path density) per unit REW interval and per unit redshift is computed as follows:

$$\frac{d^2n}{dW\,dz} = \sum_{\substack{W_i \in (W, W+dW) \\ z_i \in (z, z+dz)}} \frac{1}{g(W_i, z_i)\,dW\,dz}. \tag{2.2}$$

The resulting number density of absorbers as a function of REW and redshift is shown in Fig. 2.3, and the best-fit surface is assumed to have the following form

$$\frac{d^2n}{dW\,dz} = \frac{N_*(z)}{W_*(z)} \exp\left[-\frac{W}{W_*(z)}\right], \tag{2.3}$$

following [Nestor et al. 2005a] for the parametrization of redshift evolution:

$$N_*(z) = N_{*,o}\,(1+z)^{\alpha}, \tag{2.4}$$

$$W_*(z) = W_{*,o}\,(1+z)^{\beta}. \tag{2.5}$$

The χ^2 merit function is minimized with the Levenberg-Marquardt method (which searches for the minimum χ^2 moving gradually from steepest descent to quadratic minimization). The best-fit values for the parameters $N_{*,o}$, $W_{*,o}$, α, and β result as follows

$$\begin{cases} N_{*,o} = 0.93 \pm 0.27 \\ W_{*,o} = 0.48 \pm 0.04 \text{ Å} \\ \alpha = -0.13 \pm 0.33 \\ \beta = 0.59 \pm 0.09 \end{cases} \tag{2.6}$$

with correlation matrix $\boldsymbol{\rho}$ expressed by:

$$\boldsymbol{\rho} = \begin{pmatrix} 1 & -0.76 & -0.96 & 0.67 \\ -0.76 & 1 & 0.76 & -0.95 \\ -0.96 & 0.76 & 1 & -0.73 \\ 0.67 & -0.95 & -0.73 & 1 \end{pmatrix}, \tag{2.7}$$

where the indices of ρ_{ij} refer to fit parameters in the following order: $(N_{*,o}, W_{*,o}, \alpha, \beta)$.

The fitted value for α is not a reliable result (with p-value$\sim$0.7 instead of $\ll$1), even if its large error makes it marginally consistent with the EDR results [Nestor et al. 2005a]. All of the other parameters are in agreement with the EDR analysis, though their accuracy is not improved. Differences in results arising from fitting procedures based on χ^2 minimization (described herein) vs. likelihood maximization (employed in the EDR case [Nestor et al. 2005a]) may be due to various reasons, including the size of data set, additional degrees of freedom (e.g., $N_{*,o}$ was not fitted for in the maximum likelihood approach), and dependence on the binning of data in REW and redshift intervals (only needed for the minimum χ^2 method).

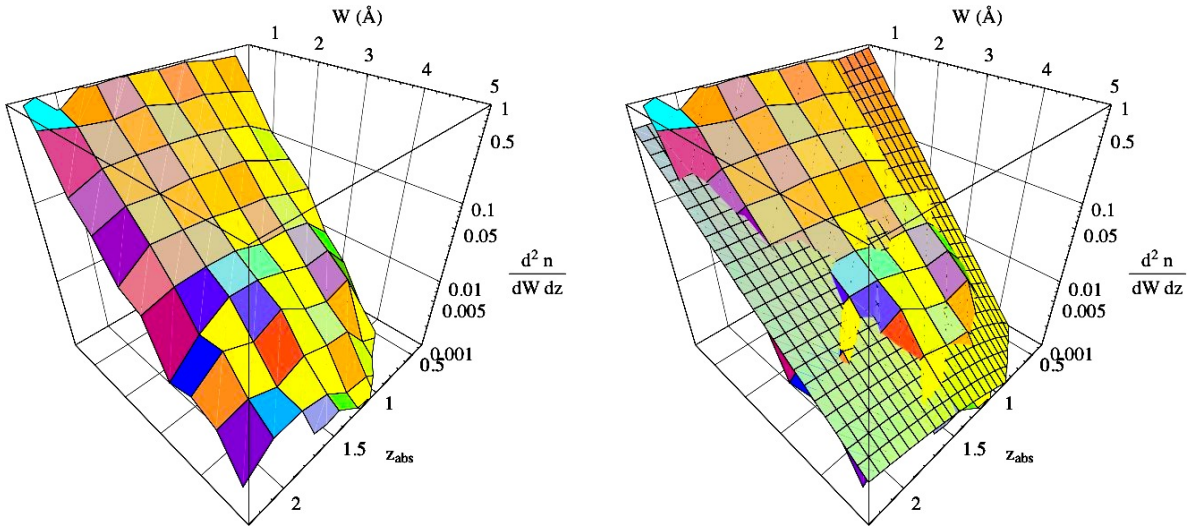

Figure 2.3: The true frequency density as a function of redshift and REW (binned in intervals of 0.25 and 0.5 Å, respectively, and divided by $g(W, z)$) is shown on the left. On the right is the best-fit surface, shown with respect to the measured distribution as a function of REW and redshift.

2.1.4.2 Rest-Equivalent Width Distribution

The total redshift path length is obtained by integrating $g(W, z)$ over the observed redshift range

$$g(W) = \int_0^\infty g(W, z)\, dz. \tag{2.8}$$

The measured $g(W)$ is shown in Fig. 2.4 together with the observed REW distribution. The Figure suggests that the MgII catalog is most sensitive to absorbers stronger than ~ 1 Å, on average.

The true distribution of REW for absorbers at all redshifts is computed by accounting for the observed redshift path as follows:

$$\frac{dn}{dW} = \sum_{W_i \in (W, W+dW)} \frac{1}{g(W_i)\, dW}. \tag{2.9}$$

The measured dn/dW is plotted in Fig. 2.5 for the entire redshift interval 0.37–2.28 and for three subsamples selected to constrain similar numbers of absorbers: 0.37–0.9, 0.9–1.3, and

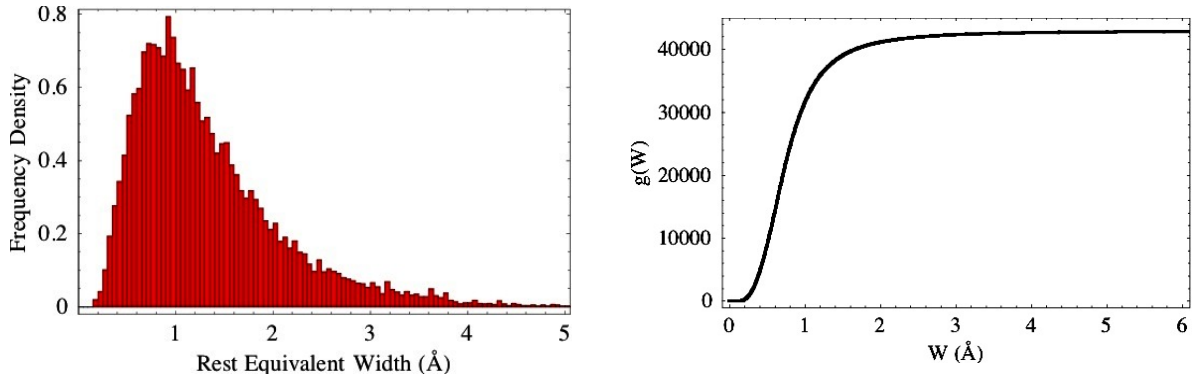

Figure 2.4: The observed frequency density of absorbers per unit Å is plotted as a function of REW on the left-hand side. The histogram is normalized so that the area subtended by the data is unitary. In the right-hand panel, the dependence of the cumulative path-length on REW is shown.

1.3–2.28. The REW distributions for all redshift bins shown in Fig. 2.5 are illustrated separately in Fig. 2.6. The Figures indicate a departure from the exponential trend in the limit of small REW, as expected from the conclusions of the EDR MgII study [Nestor et al. 2005a]. The excess above the exponential fit of systems with REW<0.3 Å was confirmed from MMT data as well [Nestor et al. 2006]. The larger number of absorbers in the DR4 permitted the identification of absorbers in the intermediate redshift range (0.9–1.3) as the main reason for this trend. However, SDSS MgII absorbers with REW∼0.3 Å are at the limit of detection and cannot provide compelling conclusions.

The fitting function outlined in Fig. 2.5–2.6 are assumed to have an exponential profile of the form

$$\frac{dn}{dW} = \frac{N_*}{W_*} \exp\left(-\frac{W}{W_*}\right). \tag{2.10}$$

The best-fit parameters N_* and W_* are listed in Table 2.1 and the joint confidence regions of the parameters are depicted in Fig. 2.5. Results generally agree within errors with the prior EDR analysis [Nestor et al. 2005a]; only in a few instances the offset reaches ∼10%. The steepening of REW distributions at lower redshifts is confirmed as well, though with a slightly weaker evolution of W_*, consistent with the smaller parameter β indicated by Eq. 2.6.

Table 2.1: The dn/dz best-fit parameters N_* and W_* shown in Fig. 2.5 are listed for each absorption redshift interval, together with asymptotic standard errors and correlation matrix element $\rho(N_*, W_*)$. Values referring to the whole sample are enhanced in bold.

Redshift Range	N_*	W_* (Å)	$\rho(N_*, W_*)$
0.37 – 2.28	**1.04±0.02**	**0.70±0.01**	**-0.65**
0.37 – 0.9	0.90±0.02	0.65±0.01	-0.69
0.9 – 1.3	1.09±0.02	0.71±0.01	-0.66
1.3 – 2.28	1.20±0.03	0.76±0.01	-0.63

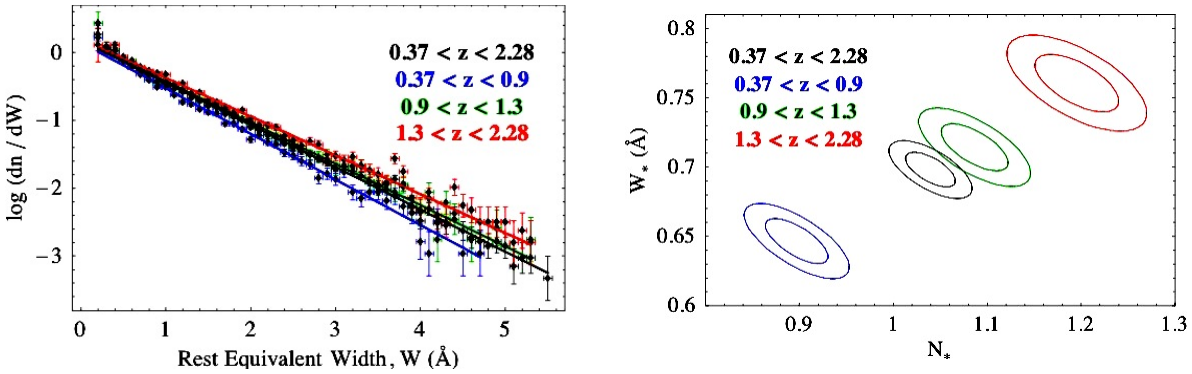

Figure 2.5: The left-hand panel presents the density of absorbers per unit redshift and per unit Å as a function of REW. Plots referring to various redshift intervals are color-coded and shown on the same Figure for comparison purposes. Detailed views of dn/dW in separate redshift bins are illustrated in Fig. 2.6. The best-fit function is overplotted on the data as a solid line assuming an exponential distribution. Vertical error bars denote 1-σ statistical uncertainities, while horizontal bars indicate bin sizes of 0.1 Å. The best-fit parameters and associated errors are shown in the right-hand panel with ellipsoidal joint confidence regions for 68% and 95% confidence levels.

2.1.4.3 Number Density of Absorption Redshifts

The histogram for the observed number density of absorbers as a function of redshift is

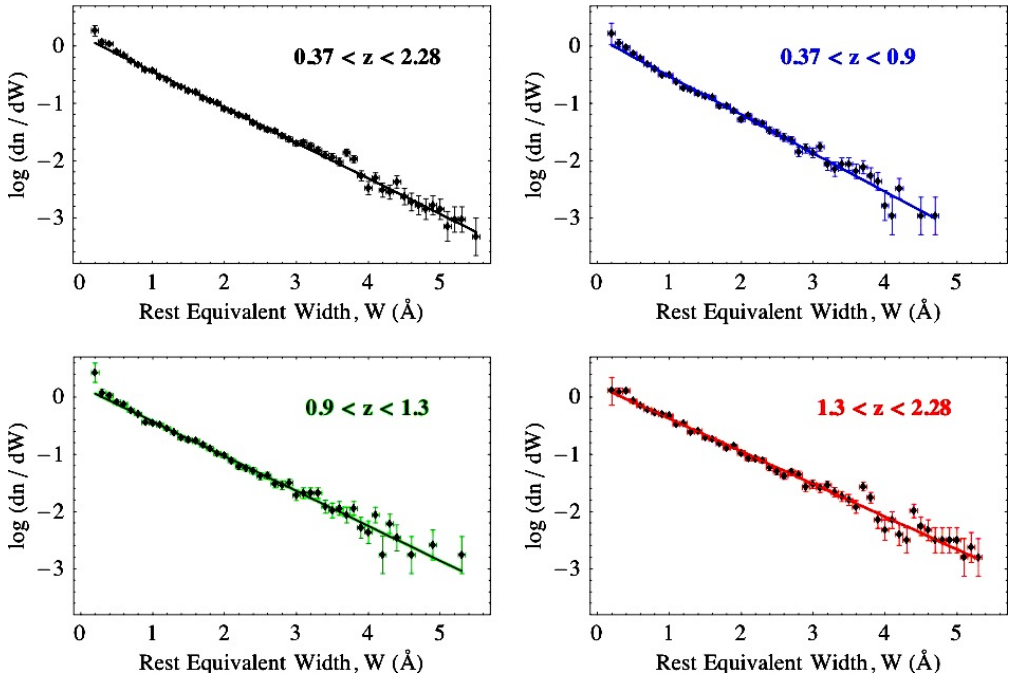

Figure 2.6: The REW distributions shown in Fig. 2.5 are presented separated in redshift intervals. It is noticed that the departure of the weakest REW bin from the overall exponential profile is mostly attributed to absorbers in the intermediate redshift range 0.9–1.3.

shown in Fig. 2.7. Instrumental and atmospheric noise effects are evident in the plot of the number of sight-lines with sufficient signal-to-noise ratio to detect absorbers stronger than a given threshold as a function of redshift. The sight-line coverage is plotted in Fig. 2.7 with various minimum REW, from 0.3 Å to 4 Å (as indicated in the Figure).

By taking into account the observed redshift path length, the real number density dn/dz is derived, which expresses the number of absorbers per unit redshift and with rest-equivalent width W within some interval, typically bounded from below by a minimum threshold $W_{\rm min}$:

$$\left.\frac{dn}{dz}\right|_{W>W_{\rm min}} = \sum_{W_i>W_{\rm min}} \frac{1}{g(W_i)}. \tag{2.11}$$

More detailed information is provided by the redshift distribution of the number density

$$\left.\frac{dn}{dz}\right|_{W>W_{\rm min}} = \sum_{\substack{W_i > W_{\rm min} \\ z_i \in (z, z+dz)}} \frac{1}{g(W_i, z_i)\, dz}, \tag{2.12}$$

whose variance σ^2 is given by the following:

$$\sigma^2 = \sum_{\substack{W_i > W_{\rm min} \\ z_i \in (z, z+dz)}} \left(\frac{1}{g(W_i, z_i)\, dz}\right)^2. \tag{2.13}$$

While only statistical errors are shown in the Figures, the large number of absorbers probably leads to a regime dominated by systematic errors.

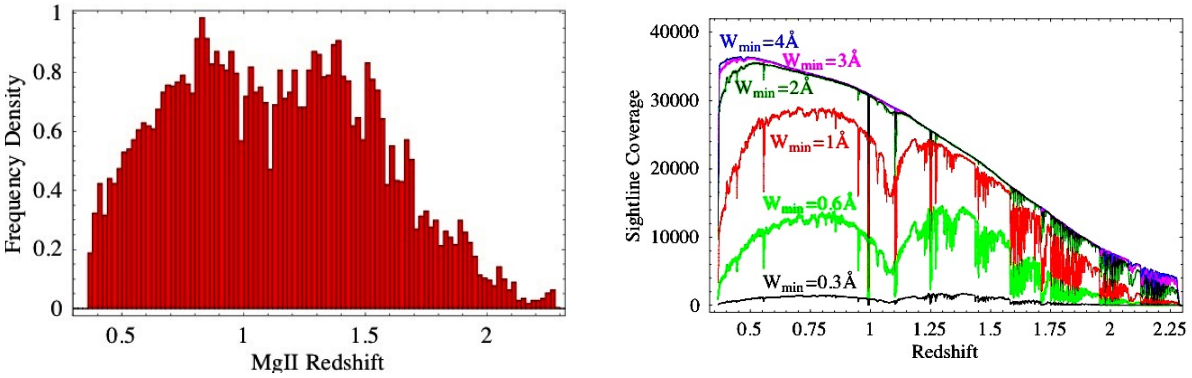

Figure 2.7: The observed redshift distribution of absorbers per unit redshift interval is plotted in the left-hand panel. The histogram is normalized so that the area subtended by the data is unitary. On the right-hand side, the sight-line coverage is shown for various minimum REW thresholds (from 0.3 Å to 4 Å, color-coded as indicated in the Figure).

The absorber number density describes the probability of intersecting an absorber of cross-section $s(z)$ and proper number density $\rho(z)$ at redshift z:

$$\frac{dn}{dz} = s(z)\, \rho(z)\, \frac{dl}{dz}, \tag{2.14}$$

where l denotes the proper length of the line-of-sight to the QSO. Thus, dn/dz is influenced by both the expansion of the Universe and the evolution of the absorbers. If $s(z) = s_o$

does not evolve in time and $\rho(z) = \rho_o(1+z)^3$ does not evolve in comoving volume, the "non-evolving" number density is proportional to the following expression:

$$\frac{dn}{dz} \propto (1+z)^3 \frac{dl}{dz} \propto \frac{(1+z)^2}{\sqrt{\Omega_M(1+z)^3+\Omega_\Lambda}}, \tag{2.15}$$

assuming a flat ΛCDM cosmology. In order to discern possible evolutionary trends of the absorbers easily, the redshift dependence of the purely cosmological contribution (assuming $\Omega_M = 0.3$ and $\Omega_\Lambda = 0.7$) is plotted in combination with the measured dn/dz in Fig. 2.8–2.9.

The number density of absorbers as a function of redshift is shown in Fig. 2.8 for REW greater than 0.3 Å, 0.6 Å, and 1 Å to 3.5 Å in steps of 0.5 Å. The non-evolutionary curves are indicated by dashed lines and normalized by minimizing the χ^2 to the binned data. Similar plots for dn/dz are repeated for REW within intervals bounded by the two nearest threshold levels indicated above, as shown in Fig. 2.9.

The larger statistical sample of DR4 in comparison with the EDR data set meant that a more refined binning in redshift space could be achieved, which allowed for the extraction of more detailed information on the evidence for evolution not easily detected in the EDR MgII catalog.

As shown in Fig. 2.8, a strong evolution in the absorber distribution is detected in the lowest redshift bin 0.37–0.57, with significance level greater than 5σ for REW greater than 0.6 Å (in the EDR study [Nestor et al. 2005a], instead, evolution was detected at 2–3σ level from REW>2 Å).

Similar trends are evident in the dn/dz distribution of absorbers with REW within the intervals indicated in Fig. 2.9, though the significance level of the evolution signal is reduced in some of the REW bins. Comparing with the EDR analysis, the detection of evolution is extended to smaller REW intervals, from REW bins above 3 Å to those above 1 Å.

A puzzling result from the EDR MgII study [Nestor et al. 2005a] concerned a particularly high incidence of absorbers (well above the non-evolutionary curve) in the lowest redshift bin for REW>0.3 Å as well as for REW within 0.3–0.6 Å, and it was argued that it might have been an artifact of the cutoff in the MgII sample at 0.3 Å. Such a signal disappeared from the dn/dz of absorbers at low-redshift bins and with REW>0.3 Å as shown in Fig. 2.8, while it was only marginally present for REW within 0.3–0.6 Å (as suggested from Fig. 2.9).

Finally, it is noted that the incidence of absorbers appears to decrease in the largest redshift bin of some of the dn/dz plots. However, that effect corresponds to the noisiest region of the redshift path and includes the least sight-line coverage, so the significance of such a signal is difficult to assess.

2.2 TWO-POINT CORRELATION FUNCTION OF MGII ABSORBERS ALONG QSO SIGHT-LINES

A simple statistical tool for studying the distribution of absorbers along QSO sight-lines is the absorber-absorber two-point correlation function ξ. The strength and extent of clustering signals are described by measuring the excess probability over random of detecting a pair of absorbers as a function of their separation.

On scales of galaxy groups and clusters, ξ appears more extended along the LOS as a consequence of large peculiar velocities within such non-linear structures. This causes an elongation of ξ in the radial with respect to tangential direction, which is often termed the *Finger of God* effect. Such an effect is expected to ease detection of clustering beyond the line-blending region, but at the same time it convolves spatial clustering with kinematic properties and the interpretation of correlation signals must contemplate both contributions.

Since peculiar motions are included in redshift measurements, ξ is evaluated in velocity space rather than distance, and it is estimated as follows [Peebles 1980]:

$$\xi(\Delta v) = \frac{N_{obs}(\Delta v)}{N_{ran}(\Delta v)} - 1, \tag{2.16}$$

where Δv is the velocity separation between two systems as measured at the cosmic time when the absorption lines are created. When $\Delta v/c \ll 1$, Δv may be approximated as [Sargent et al. 1980]

$$\frac{\Delta v}{c} \approx \frac{z_2 - z_1}{1 + (z_1 + z_2)/2}, \tag{2.17}$$

where $z_1 < z_2$, with z_1 and z_2 referring to the redshifts of a pair of absorbers. In Eq. 2.16, $N_{obs}(\Delta v)$ denotes the observed number counts of MgII pairs separated by Δv, while $N_{ran}(\Delta v)$ describes the corresponding number of pairs (within the same Δv interval) obtained by

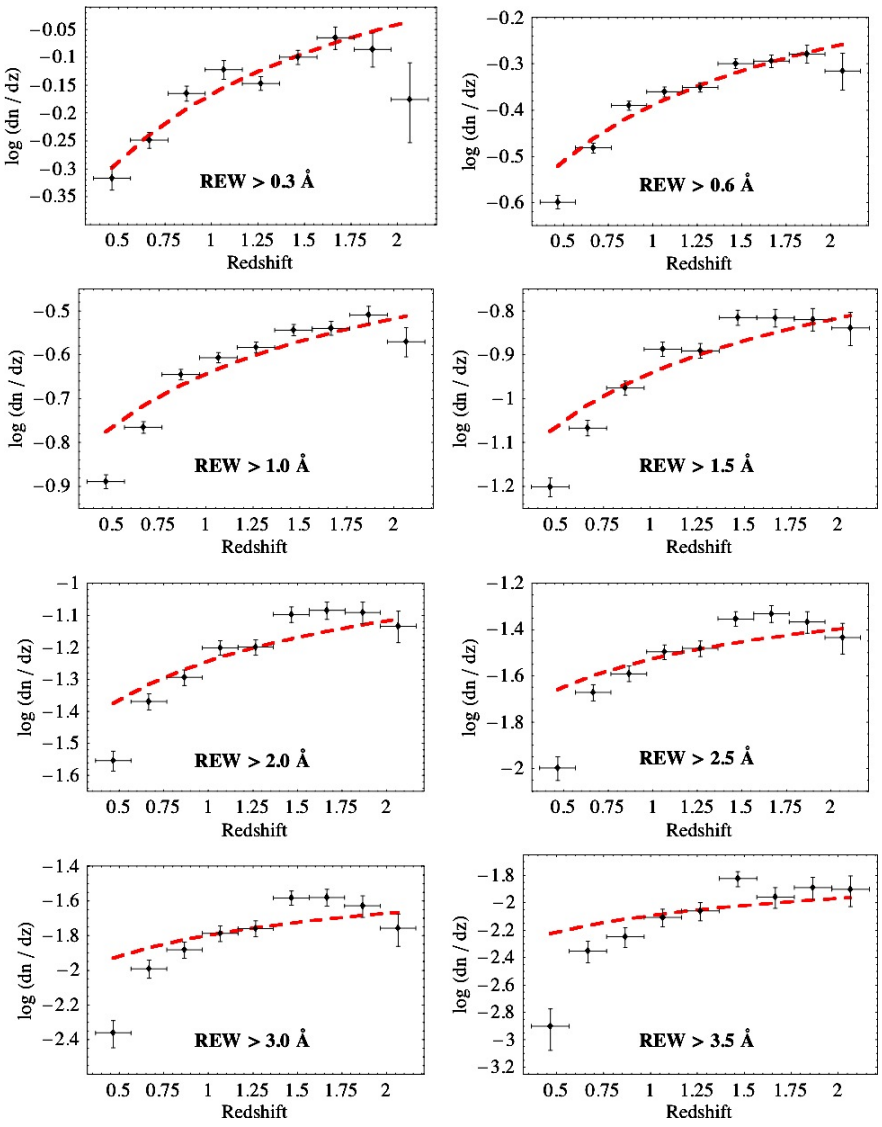

Figure 2.8: The redshift distribution of MgII number density dn/dz is shown for REW stronger than a minimum threshold $W_{\rm min}$ of 0.3, 0.6, 1.0, 1.5, 2.0, 2.5, 3.0, and 3.5 Å, as specified in each panel. The data are binned into redshift bins of width 0.2. Non-evolutionary reference curves are dashed and scaled to minimize the χ^2 to the binned data. Note that the largest redshift bin corresponds to the noisiest region including the least sight-line coverage, so the significance of possible trends is difficult to assess.

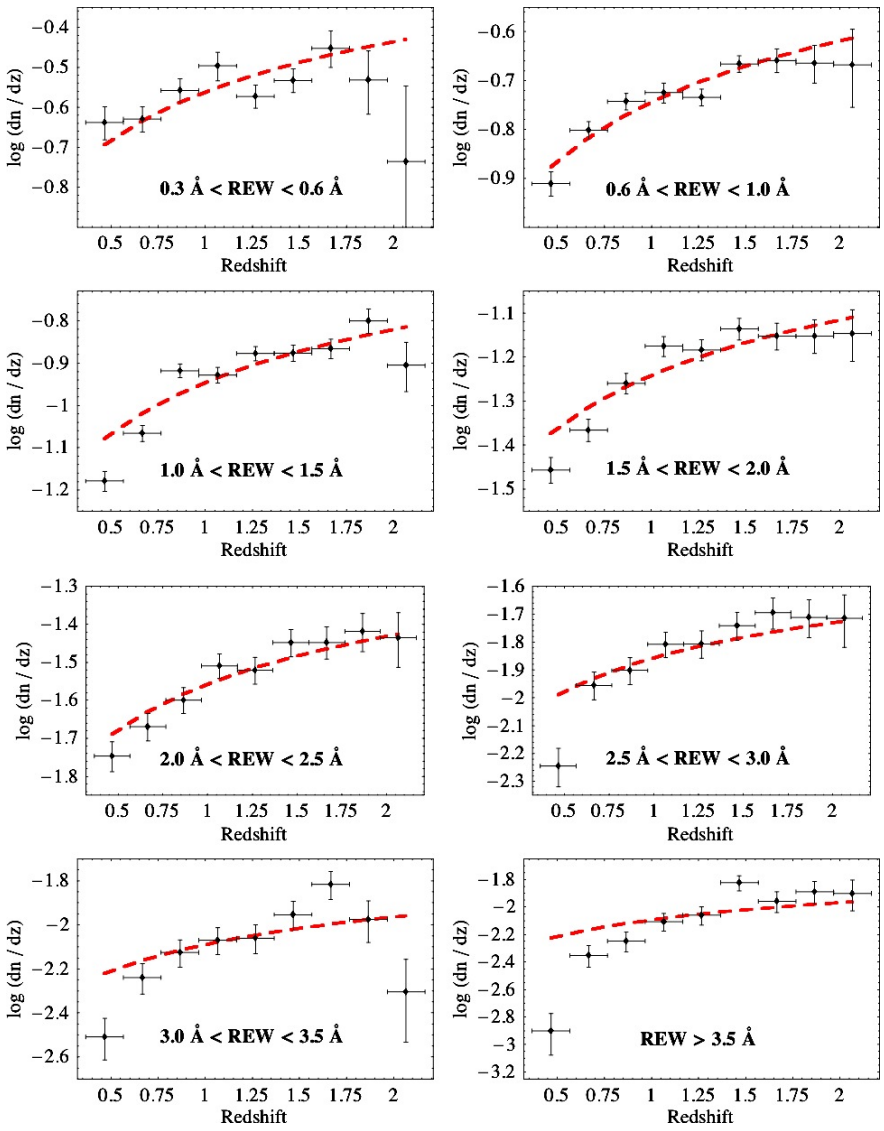

Figure 2.9: The redshift distribution of MgII number density dn/dz is shown for REW within the following intervals: 0.3–0.6 Å, 0.6–1.0 Å, 1.0–1.5 Å, 1.5–2.0 Å, 2.0–2.5 Å, 2.5–3.0 Å, 3.0–3.5 Å, and >3.5 Å (as specified in each panel). The data are binned into redshift bins of width 0.2. Non-evolutionary reference curves are dashed and scaled to minimize the χ^2 to the binned data. Note that the largest redshift bin corresponds to the noisiest region including the least sight-line coverage, so the significance of possible trends is difficult to assess.

averaging 100 Monte Carlo simulations of randomly distributed absorbers. Such "random" configurations are required to incorporate selection and evolutionary effects.

2.2.1 Numerical Simulations

In order to automatically reproduce the observed redshift and REW distributions, each of the 14,536 detected absorbers is placed randomly in one of the 44,606 LOS, making sure the MgII absorption lies between the Lyman α and MgII emissions in the QSO spectrum. Additionally, PSF i-band magnitudes of random QSOs are required to differ by not more than 0.5 magnitudes with respect to the original absorbing QSOs. The last condition is introduced to reproduce similar average signal-to-noise levels and, consequently, a higher likelihood of detecting weaker absorbers in brighter QSOs rather than fainter ones (as inferred from Fig. 3.1).

Out of all requirements, the one which had the most impact was $z_{abs} < z_{QSO}$, significantly suppressing $\xi(\Delta v)$ at all Δv (as expected as a consequence of denser line distributions, arising from the introduction of the constraint). Such a condition was then refined to reflect the detection criteria, and a minimum separation of 3000 km s^{-1} from both MgII and Lyman α emissions was set.

Scattering the observed absorbers in all of the QSO sight-lines, subject to the above mentioned conditions, lead to the same results (within statistical uncertainties) as the more conservative approach of simulating absorbers consistently with the noise conditions along each spectrum, which reduced computational time by a factor of $\sim 10^3$.

2.2.2 Observed Velocity Separations

In order to measure pair separations, only those sight-lines with at least two detected absorbers are considered. The observed sample of MgII-absorbed QSOs includes 2,664 of such sight-lines, and the redshift distribution of the 6,061 absorbers within them is compared with the overall population in Fig. 2.10. Both samples have very similar average redshift: $\langle z_{abs} \rangle \sim 1.13$ and $\langle z_{abs} \rangle \sim 1.17$ for all and at least two absorbers per line-of-sight, respectively.

Number counts of velocity separations Δv are binned in 100 km s^{-1} intervals for $\Delta v <$

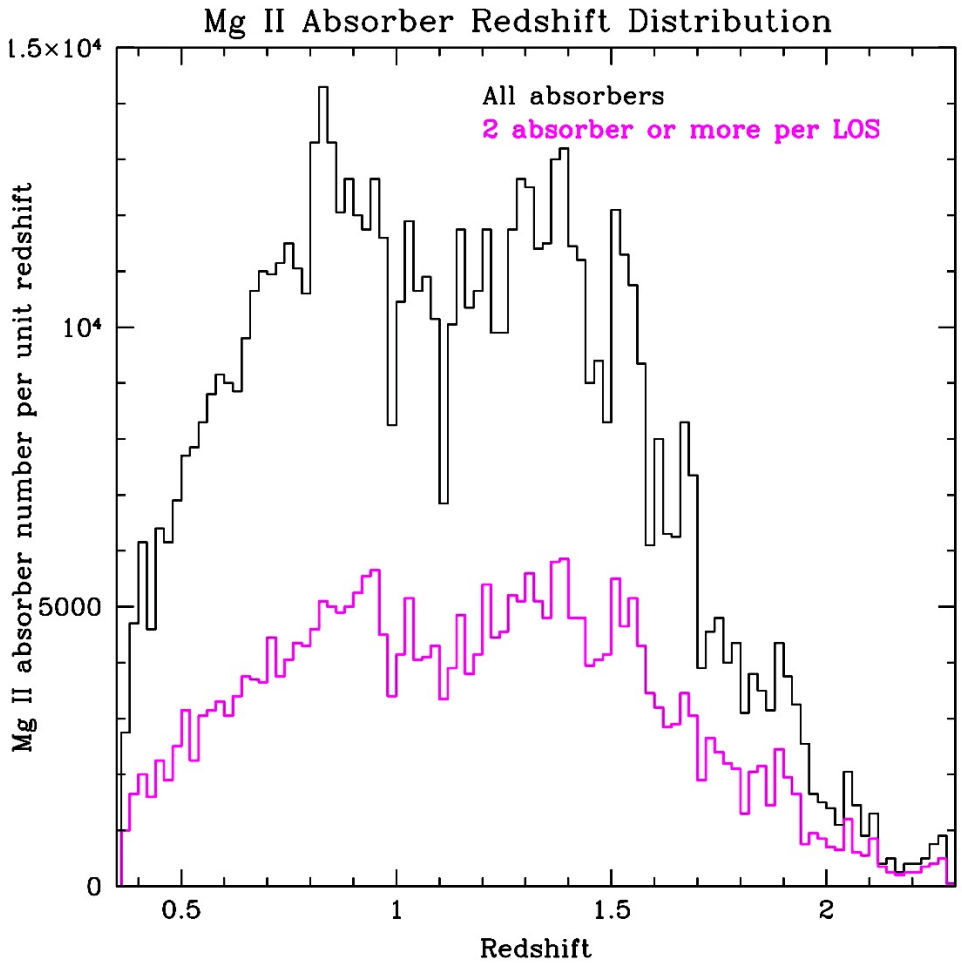

Figure 2.10: The black histogram shows the observed redshift distribution of all 14,536 MgII absorbers detected within the redshift interval (0.367, 2.281) in 11,139 QSO spectra, while the magenta colored histogram includes 6,061 MgII detections in 2,664 lines of sight with at least two systems per sight-line. The average redshift of absorbers in the two samples does not differ significantly: $\langle z_{abs} \rangle \sim 1.13$ and $\langle z_{abs} \rangle \sim 1.17$ for the cases of all and at least two absorbers per line-of-sight, respectively.

500 km s^{-1}, while for greater Δv values bin widths are 300, 500 and 1000 km s^{-1}, depending on sizes of samples (as a function of REW or redshift). Different bin widths are adopted to assure coverage of all the Δv range considered. In fact, if number counts are averaged within

too small bins leading to zero-counts in nearby bins, then the measured ξ is overestimated.

2.2.3 Error Evaluations

Since only very few MgII absorbers are detected per LOS, with most of the contribution arising from sight-lines with two or three systems, number counts are considered independent and Poisson errors are employed (in agreement with [Landy & Szalay 1993]). Since counts in Δv bins are generally small, errors bars are computed as follows. If $\pi = n/N$ is the (unknown) probability of counting n independent velocity separations Δv between absorbers within a sample of N QSO sight-lines, the observed counts $\tilde{n}$ in Δv intervals are expected to be distributed according to the binomial distribution with average $N\pi$, and standard deviation $[N\pi(1-\pi)]^{1/2}$. Assuming the range of variability of $\tilde{n}$ around the mean is less than τ times the standard deviation, i.e. $|\tilde{n} - N\pi| < \tau[N\pi(1-\pi)]^{1/2}$, the solution for π is:

$$\pi = \frac{\tilde{n} + \tau^2/2}{N + \tau^2} \pm \frac{\tau\sqrt{\tilde{n}\,(1 - \tilde{n}/N) + \tau^2/4}}{N + \tau^2}. \tag{2.18}$$

The range of error is not centered around the measured $\tilde{n}$ because of the asymmetry of the binomial distribution, but it becomes approximately Gaussian for large number counts ($\tilde{n} > 10$). The value of τ is calculated by integrating the binomial probability density function within the interval $N\Delta\pi$, with $\Delta\pi$ specified by the extreme values of Eq. 2.18, until a confidence level of 68% is reached. Because of averaging over a large number of simulated catalogs, errors on random reference counts are deemed negligible with respect to the observed ones.

2.2.4 Minimum Velocity Separation

The SDSS spectral resolution does not permit a measurement of individual systems separated by less than ∼140–170 km s^{-1} over the MgII absorber redshift range. Line-blending constitutes a further cause of incompleteness in the number counts of close pairs, and the resulting minimum detectable velocity separations are expected to increase as a function of

REW. However, this does not automatically imply that clustering at small Δv would be attributed mostly to weak absorbers. In fact, strong absorption lines might be more clustered than the weak ones, and their contribution to ξ at small Δv could still dominate.

A detailed account for line-blending effects is not included herein. Instead, a minimum separation $\Delta v_{\rm min}$ is set for all MgII pairs, and only those intervals $\Delta v > \Delta v_{\rm min}$ are considered, provided they do not enclose MgII detections within less than $\Delta v_{\rm min}$ from any of the pair components. As a consequence, a succession of detections, separated by less than $\Delta v_{\rm min}$ from any absorption line to the next one, is considered as a single system. Intervals with respect to such a system are computed from its most external lines as shown in Fig. 2.11, which illustrates accepted and rejected line separations in a specific case. On the other hand, the method adopted is not fully equivalent to combining two or more closely separated systems into one, since no common absorption redshift or REW are computed. Such a simplification makes the creation of simulated catalogs much faster, while still allowing the introduction of some smearing effect.

The two-point correlation function $\xi(\Delta v)$ is evaluated at several threshold values, with $\Delta v_{\rm min}$ ranging from zero to 500 km s^{-1}. Note that this is not equivalent to simply considering the same $\xi(\Delta v)$ for $\Delta v > \Delta v_{\rm min}$, since intervals greater than $\Delta v_{\rm min}$ but involving lines separated by less than the threshold are also excluded (see Fig. 2.11).

2.2.5 Results

The absorber-absorber correlation function $\xi(\Delta v)$ is evaluated for all absorbers, as a function of redshift, REW, and plotted in Fig. 2.12 (a)–(c), respectively, without setting a minimum $\Delta v_{\rm min}$ threshold. The same plots (a)–(c) are presented for $\Delta v_{\rm min}$ from 200 to 500 km s^{-1}, in steps of 100 km s^{-1}, in Fig. 2.13–2.16.

A clustering signal is detected for $\Delta v < 500$ km s^{-1} in all cases (apart from those with $\Delta v_{\rm min} = 500$ km s^{-1}), indicating an association of MgII absorbers with either galaxy-group scales or LOS velocity dispersions typical of galaxy clusters. Unfortunately, the information in this Δv range is degraded by line-blending, which is believed to be responsible for suppressing ξ until at least $\sim$300 km s^{-1}. Provided line-blending does not depend significantly

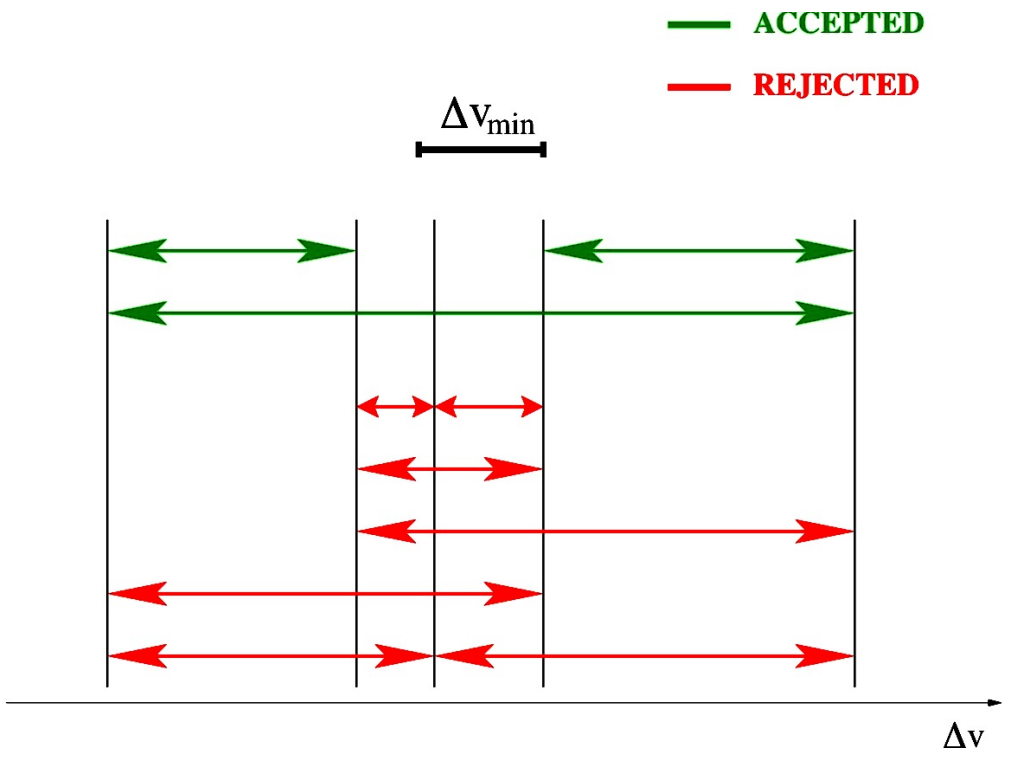

Figure 2.11: Accepted and rejected pair separations (in green and red colors, respectively) after imposing a minimum threshold $\Delta v_{\rm min}$. Vertical lines denote locations of absorption lines in Δv space. Note that several intervals greater than $\Delta v_{\rm min}$ are rejected as well, because they are deemed to refer redundantly to the "same" system (which includes the three internal lines in the case depicted in the Figure).

on redshift too, plots (b) in Fig. 2.12–2.14 suggest that ξ evolves with redshift. In fact, MgII absorbers in the lower redshift bin ($z_{abs} < 1$) exhibit a stronger clustering signal (though only at $\sim$1-σ significance level) with respect to higher-redshift systems. The growth of clustering at lower redshifts is expected from gravitationally induced growth of initial perturbations, and MgII systems may trace such an evolution.

Plots (c) in Fig. 2.12–2.14 indicate that stronger absorption lines (with REW>1.5 Å) may be more strongly clustered than weaker systems (with REW<1.5 Å) also at $\sim$ 1-σ significance level. The fact that such a conclusion holds also when no minimum $\Delta v_{\rm min}$ threshold is set (as in Fig. 2.12) strengthens the significance of the result, since line-blending

of close pairs is more likely for strong than weak absorbers.

The clustering signal vanishes at $\Delta v > 500$ km s^{-1} in all plots (for any $\Delta v_{\rm min}$). However, an anti-correlation feature at $\Delta v \sim 800$–1100 km s^{-1} is present in all figures, and it corresponds to a region in velocity space in which line-blending is expected to be negligible.

2.2.6 Discussion

Velocity separations Δv smaller than 200 km s^{-1} are expected to be mostly due to internal motions within galaxies [Sargent et al. 1988a, Heisler et al. 1989, Petitjean & Bergeron 1994, Rauch et al. 1996], but the few intervals detected in this range are heavily affected by line-blending, so their value for ξ is not considered.

Larger velocity separations (up to several hundreds of km s^{-1}) are believed to include contributions from both cosmological expansion and peculiar motions of absorbers within galaxy clusters [Shi 1995, Crott et al. 1997]. It is unclear which of the two components predominates, so $\xi(\Delta v)$ for Δv up to $\sim 10^3$ km s^{-1} is deemed to be due to either spatial clustering or LOS kinematics of absorbers in galaxy clusters (whose typical LOS velocity dispersions range from 300 to 1400 km s^{-1} [Zabludoff et al. 1993, Dinshaw & Impey 1996]).

If the contribution from peculiar motions is negligible at $\Delta v \sim 10^3$ km s^{-1}, the observed anti-correlation feature would mean that the probability of finding MgII absorbers near outer regions of galaxy clusters is low and most of the gas lies well within clusters. On the other hand, if the signal is of kinematic rather than spatial origin, it would indicate that high-velocity galaxies in galaxy clusters are deficient in gas content. Such a scenario may be explained in terms of ram pressure stripping of the interstellar medium of galaxies (exerted by the intracluster medium within which they orbit), which is likely to be stronger for galaxies with higher velocities (e.g., see [Gunn & Gott 1972, Hester 2006]).

2.2.7 Future Improvements

An implicit assumption of this clustering study is that QSO sight-lines are independent. However, the SDSS provides so many QSO spectra that the correlation of absorbers among LOS may probe clustering on scales where a signal is observed along QSO sight-lines. As-

suming the 11,139 DR4 QSOs with MgII detections are randomly scattered within the 4,783 square-degrees of the DR4 spectroscopic survey, the comoving transverse mean distance between nearest neighbors would range from 8 to 32 Mpc (estimated as $\sim 0.5/\sqrt{\sigma}$, with σ denoting the mean projected number density of QSOs) for absorption redshifts from 0.37 to 2.3, respectively. If absorbers are clustered, as found at $\Delta v < 500$ km s^{-1}, more transverse comoving distance intervals would be smaller than 8 Mpc and overlap with the region probed along sight-lines (LOS velocity separations of 500 km s^{-1} correspond to comoving LOS distances of 7–8 Mpc over the whole absorber redshift range).

It is planned to complement the results achieved in the radial direction with the transversal two-point correlation function. That would not only constitute a more complete treatment of the MgII clustering (probing larger scales in detail), but also remove the ambiguity between cosmological expansion and peculiar motion, and help interpret features like the one observed at $\Delta v \sim 10^3$ km s^{-1} (if confirmed to exist). Results will be compared to the galaxy-galaxy correlation function, in order to help the investigation of the association of MgII absorbers with galaxies.

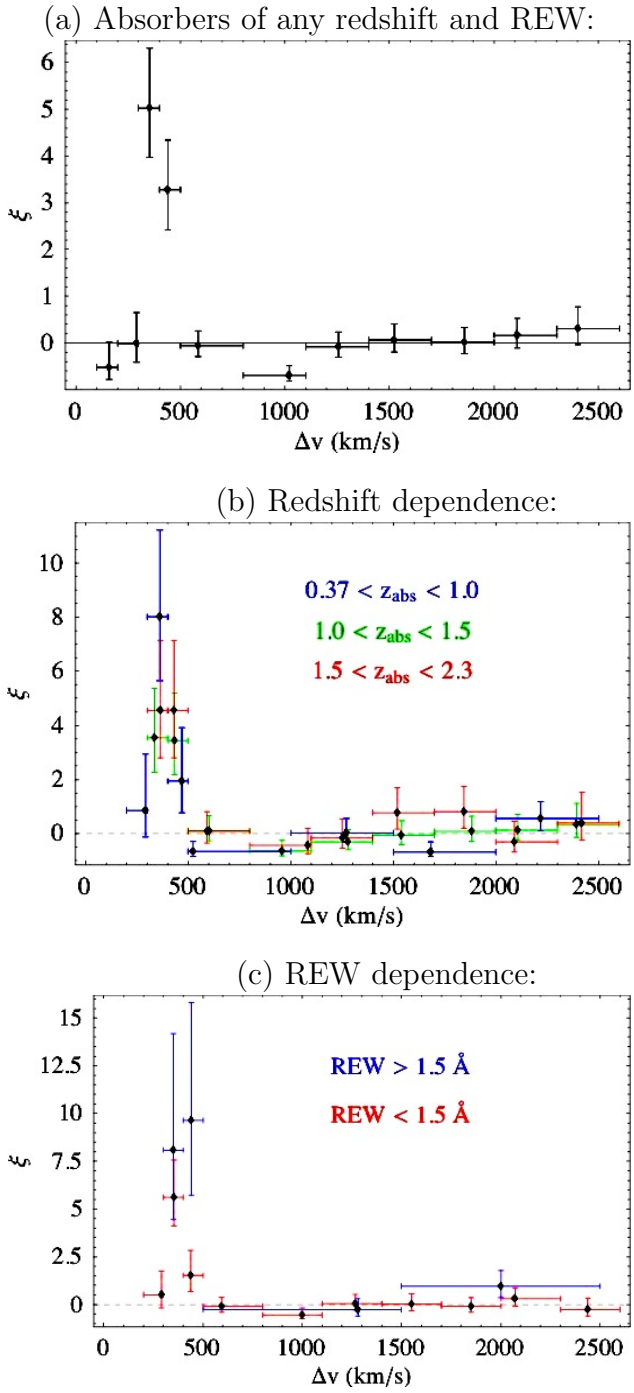

Figure 2.12: The two-point correlation function ξ is plotted as a function of velocity separation Δv. Panel (a) includes all detected MgII absorbers, while panels (b) and (c) compare absorption subsets depending on redshift and REW intervals, respectively, as indicated in the corresponding legends. The zero-correlation level is indicated by a dashed line. Features common to all plots are, in order of increasing Δv, line-blending suppression, positive clustering signal, and anti-correlation effect at $\Delta v \sim 10^3$ km s^{-1}. More detailed comments are described in the text.

(a) Absorbers of any redshift and REW:

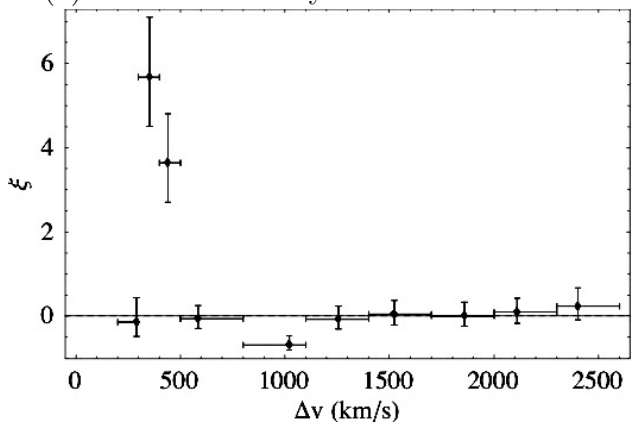

(b) Redshift dependence:

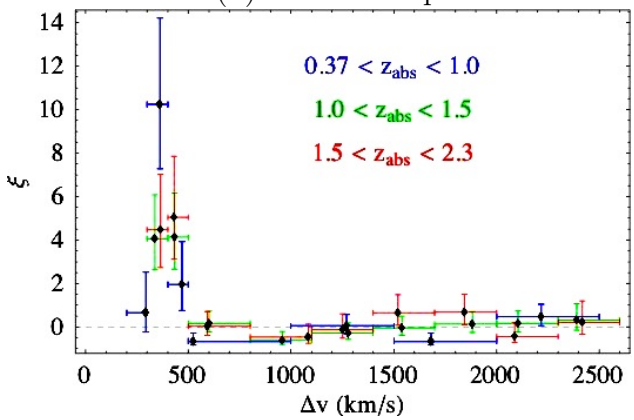

(c) REW dependence:

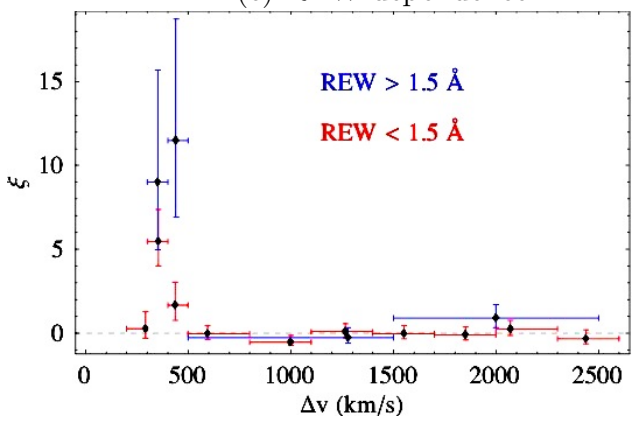

Figure 2.13: Same as Fig. 2.12, but setting a minimum velocity separation of 200 km s^{-1}.

(a) Absorbers of any redshift and REW:

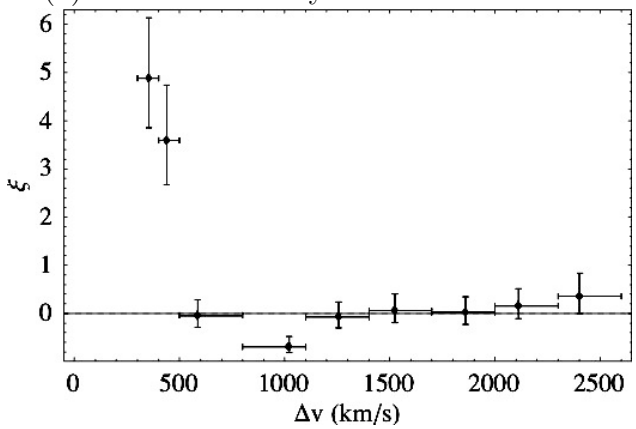

(b) Redshift dependence:

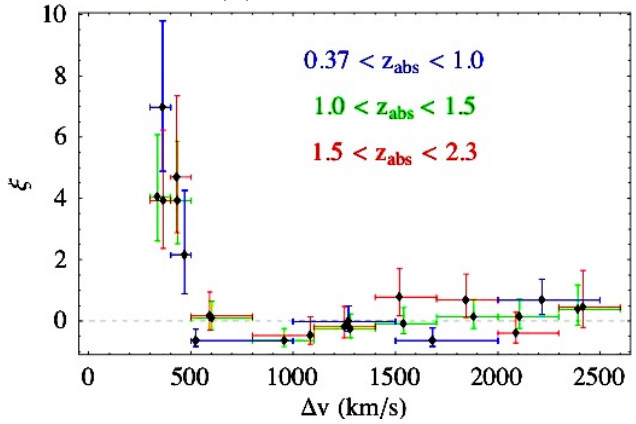

(c) REW dependence:

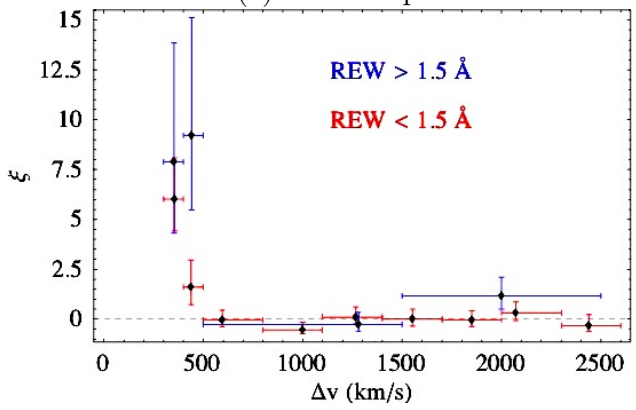

Figure 2.14: Same as Fig. 2.12, but setting a minimum velocity separation of 300 km s^{-1}.

(a) Absorbers of any redshift and REW:

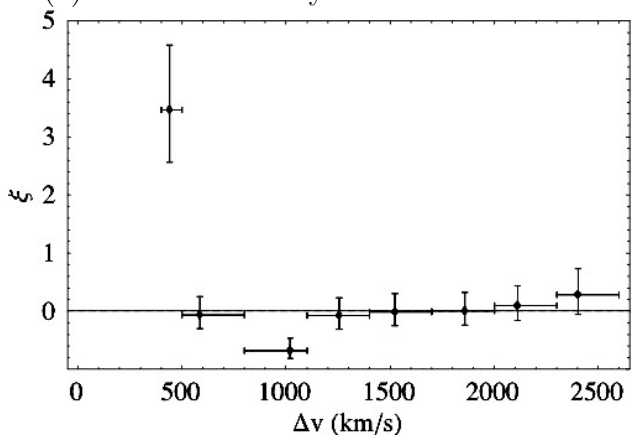

(b) Redshift dependence:

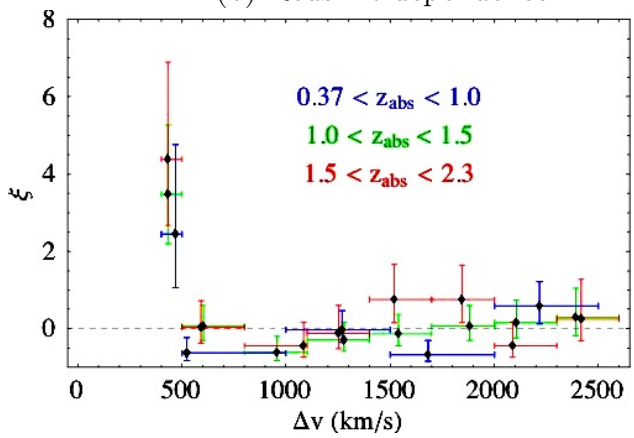

(c) REW dependence:

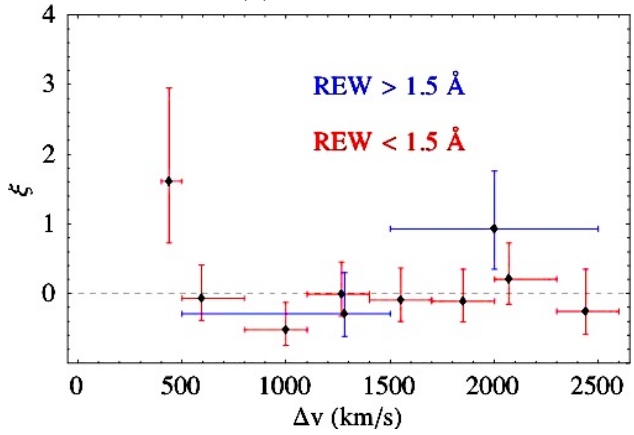

Figure 2.15: Same as Fig. 2.12, but setting a minimum velocity separation of 400 km s^{-1}.

(a) Absorbers of any redshift and REW:

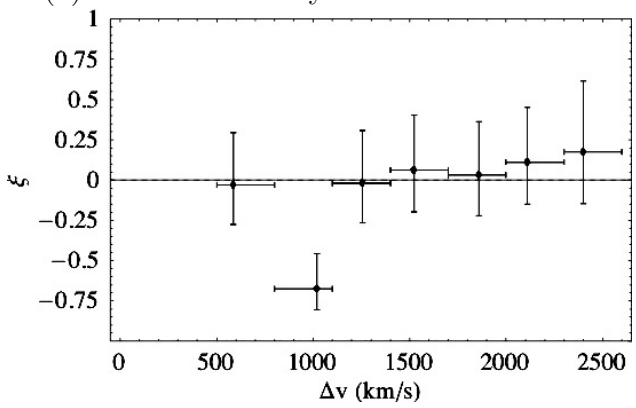

(b) Redshift dependence:

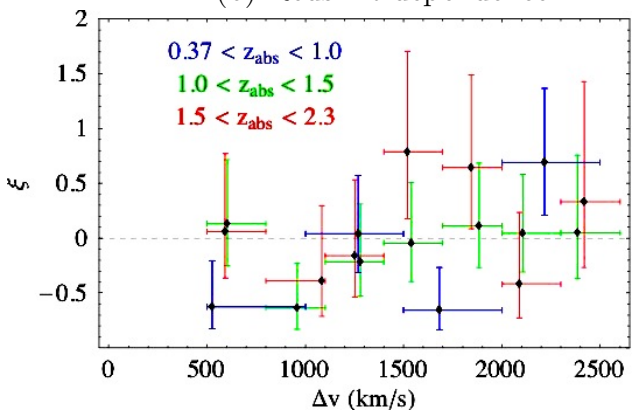

(c) REW dependence:

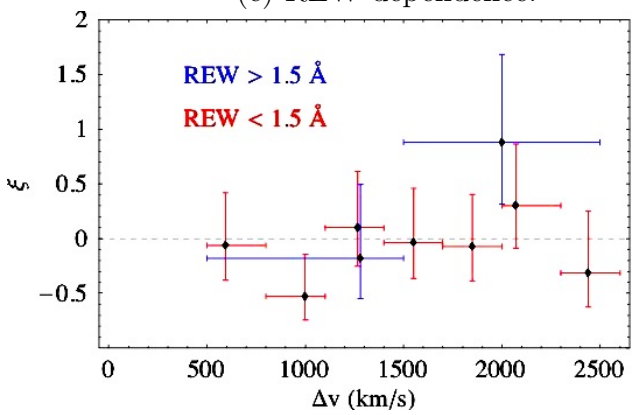

Figure 2.16: Same as Fig. 2.12, but setting a minimum velocity separation of 500 km s^{-1}.

3.0 SDSS GALAXIES AROUND MGII ABSORBERS

Studies of the relation between galaxies and MgII absorber properties in the pre-SDSS era could not reach statistically significant results because of the limited sample sizes of MgII absorbers employed. In this chapter, the dependence of galaxy properties on the MgII REW is investigated by taking advantage of the large MgII catalog extracted from the SDSS DR4 QSO spectra and the large imaging area encompassing all QSOs. The caveat of this approach is that SDSS galaxies are not imaged satisfactorily in the MgII redshift range of detection, and the gain in statistical error is challenged by faint signals. Thus, this analysis is restricted to the lowest redshift bins, and redshift evolution cannot be assessed properly. The QSO glare causes incomplete galaxy detection depending on the QSO brightness, the galaxy magnitude, and the QSO–galaxy angular separation. A method to correct for QSO glare effects and possible statistical biases arising from them is developed. Galaxy density profiles, QSO-galaxy cross-correlations, colors and other photometric properties of galaxies associated with absorbers are analyzed, and the luminosity function for such galaxies is attempted, but despite this completeness is reached only for bright galaxies. Calculations involving galaxy impact parameters and luminosities are derived assuming the standard ΛCDM cosmological model, with $\Omega_m = 0.3$, $\Omega_\Lambda = 0.7$, and Hubble constant $H = 70$ km s^{-1} Mpc^{-1}. Moreover, as in the rest of this thesis, all REWs refer to the 2796 Å component of the MgII doublet.

3.1 ANGULAR DISTRIBUTION OF MGII-ASSOCIATED GALAXIES

3.1.1 The MgII Absorber Sample

The SDSS spectroscopic MgII catalog is cross-correlated with the SDSS imaging catalog of galaxies near QSO sight-lines. QSO spectra provides the information regarding the QSO classification, its redshift, and absorption lines (detected as described in § 2.1.2). Positions and magnitudes of QSOs and galaxies are extracted from SDSS photometric tables. In particular, the magnitudes used for QSOs are point-spread function (PSF) magnitudes, while for galaxies model[1] magnitudes are used.

Unfortunately, SDSS galaxies can only be detected marginally in the lower redshift interval (approximately $z < 1$) of MgII detection. The analysis is restricted to MgII systems occurring in the three redshift bins (0.37, 0.55), (0.55, 0.76), and (0.76, 1). While the number of absorbers increases in the higher redshift bins (among the ones mentioned above), the signal of MgII absorber-galaxy association weakens because of increasing contamination from non-absorbing foreground galaxies and incompleteness of higher-redshift galaxies.

MgII absorbers are further subdivided in five REW intervals: (0.16, 0.6), (0.6, 1), (1, 2), (2, 3), and (3, 8.5), all expressed in Å units. The minimum and maximum values of these intervals (0.16 and 8.5 Å) correspond to the weakest and strongest absorbers detected in the whole data set.

The weakest REW bin (less than 0.6 Å) is highly incomplete given the SDSS resolution, and it is dominated by bright QSOs (e.g., see the average QSO r-band magnitude as a function of REW shown in Fig. 3.1 for absorbers with $z_{abs} \in (0.37, 0.55)$). Nevertheless, it is included in the study because of the interest in MgII absorbers found in environments with low HI column densities ($\sim 10^{19}$ atoms cm^{-2} on average) and without damped Lyman α systems (which are characterized by HI column densities greater than 2×10^{20} atoms cm^{-2}) [Rao et al. 2005, Rao 2005]. The strongest REW bin (greater than 3 Å) includes only a

[1]Model magnitudes are constructed by fitting pure deVaucouleurs and exponential profiles to galaxy images [Stoughton et al. 2002, Abazajian et al. 2004]. The model with the highest likelihood in the r-band is chosen, and it is applied to all of the other bands (after convolving with the appropriate PSF). Since the flux is measured through equivalent apertures in all bands, estimates of galaxy colors are not biased. Furthermore, colors from model magnitudes have higher signal-to-noise ratios than those from Petrosian magnitudes.

few dozen absorbers (depending on the redshift bin – see Table 3.1), but it is considered separately because of recent findings suggesting that ultra-strong MgII absorbers may arise partly from very luminous galaxies (4 to 13 L_*) [Nestor et al. 2007].

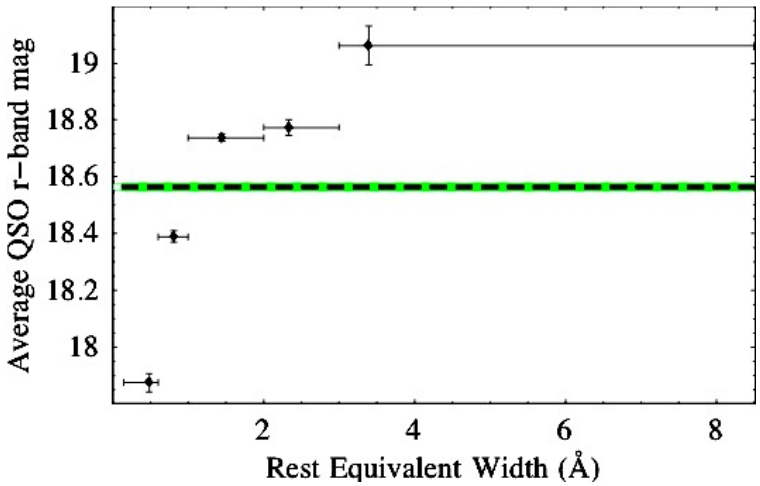

Figure 3.1: The signal-to-noise ratio affects the minimum detectable REW, so weaker systems are detected more often in brighter QSOs on average, as shown for absorbers in the redshift range (0.37, 0.55). The dashed line and green band refer to the average QSO magnitude and its error for all REW.

Galaxies around QSO sight-lines with multiple MgII detections cannot be uniquely associated with each absorber. This is not expected to cause serious problems because galaxy detection near the smallest redshift absorber dominates the absorber-galaxy association signal. However, in order to avoid possible biases[2] a more conservative approach is taken, and only those lines of sight with one and only one MgII absorber are retained. The redshift distribution of absorbers in such sight-lines with respect to the whole sample is plotted in Fig. 3.2, while the number counts subdivided in redshift and REW bins are listed in Table 3.1.

[2]For example, the number density of galaxies at small angles from the QSO sight-line may be artificially enhanced as a consequence of assuming that all of the detected galaxies are associated with the lowest redshift absorber.

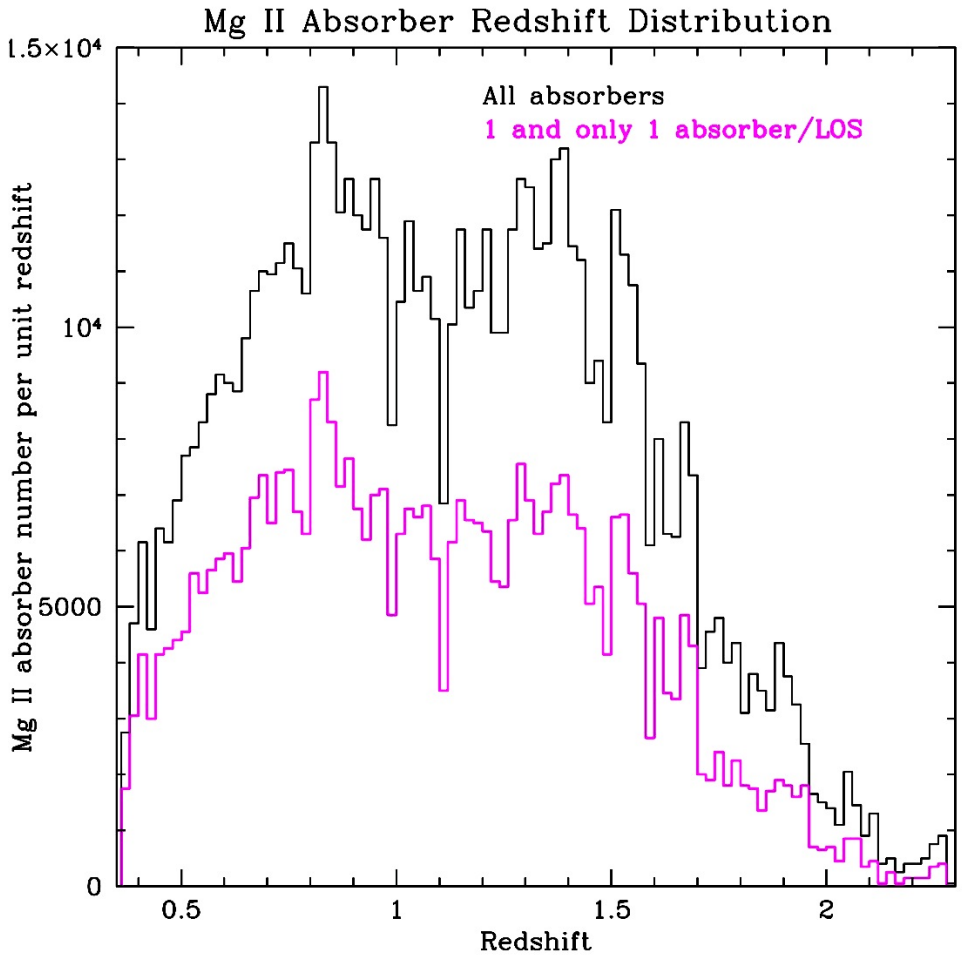

Figure 3.2: The black histogram shows the observed redshift distribution of all 14,536 MgII absorbers detected within the redshift interval (0.367, 2.281) in 11,139 QSO spectra, while the magenta colored histogram refers to 8475 MgII detections in lines of sight within which one and only one MgII absorber is found.

3.1.2 Reference QSO Samples

In order to compare the neighborhoods of absorbers in different REW and absorption redshift z_{abs} intervals, two sets of reference QSO sight-lines are created for each absorber subset (with similar QSO redshift, z_{QSO}, and i-band magnitude, i_{QSO}, as QSOs with absorbers): a sample

Table 3.1: MgII absorbers from QSO sight-lines with one and only one system detected are listed subdivided in redshift and REW bins.

Redshift bin	(0.16, 0.6)Å	(0.6, 1)Å	(1, 2)Å	(2, 3)Å	(3, 8.5)Å	ALL REWs
(0.37, 0.55)	82	199	353	102	17	753
(0.55, 0.76)	146	398	592	155	51	1342
(0.76, 1.00)	184	500	769	200	65	1718

without MgII detections, and a random sample regardless of the presence of MgII systems. While the former minimizes the contamination by absorbers, it does not represent the average random properties, which are reflected by the latter.

Both samples require N_{ref} QSOs for each QSO sight-line in the absorber catalog to match i_{QSO} and z_{QSO} within $\pm\Delta i_{QSO}$ and $\pm\Delta z_{QSO}$ from the corresponding MgII-absorbing QSO, respectively. The value of Δz_{QSO} is set to 0.1 in all cases; for the lowest MgII z_{abs} interval (0.37, 0.55) $N_{ref} = 5$ and $\Delta i_{QSO} = 0.35$, while for the other two z_{abs} bins $N_{ref} = 4$ and $\Delta i_{QSO} = 0.5$. The slightly more relaxed criteria for higher redshift absorbers are due to the larger number of absorbing QSOs matched to reference QSOs and the attempt of keeping the fraction of duplicated reference QSOs as small as possible (of the order of a few percent). Errors on QSO magnitudes[3] and redshifts are typically much smaller than the binning used for selection of reference samples, and so they are neglected.

Figures 3.3–3.8 show that the difference between reference i_{QSO} and z_{QSO} with the corresponding values of absorbed QSOs is roughly uniformly distributed in all REW and z_{abs} intervals, so no obvious biases are expected to affect the references. Furthermore, signal-to-noise levels in reference QSOs are required to allow the detection of MgII doublets with the same REW and z_{abs} as measured in the MgII-absorbing spectra, ensuring that the observed systems would truly not be present in the non-absorbing reference sample. Each reference QSO is assigned a "ghost" absorber at z_{abs} corresponding to the actual MgII detection in

[3]Errors on PSF magnitudes of 95% of all QSOs are less than 0.12, 0.04, 0.03, 0.03, 0.07 magnitudes in the u, g, r, i, z-bands, respectively.

the absorbed QSO (previously used to select the reference QSO). Thus, impact parameters of galaxies around reference sight-lines could be expressed in terms of physical distances for comparison with the actual absorber LOS.

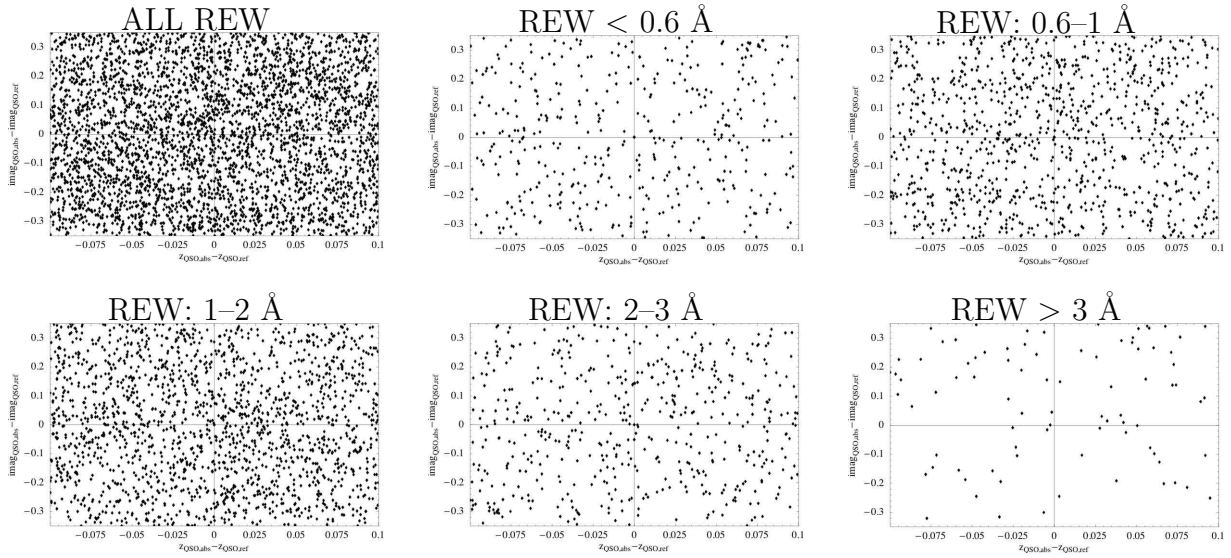

Figure 3.3: Difference of z_{QSO} and i-band magnitude for random reference QSOs vs absorbing QSOs is plotted in various REW intervals for $z_{abs} \in (0.37, 0.55)$.

Reference QSOs are extracted from all 44,606 QSOs for the random sample and from the 33,467 non-absorbing QSOs for the non-absorbing reference sample, respectively in a random manner. Thus, it is possible that a small fraction of reference QSOs (generally of the order of a few percent) contains duplicate objects. The largest fraction of repeated objects is found in the reference samples pertaining to all REWs, and it amounts to about 7% and 11% for the random and non-absorbing references, respectively, in the lowest z_{abs} bin (0.37, 0.55); the same quantities increase to 8% and 12% for $z_{abs} \in (0.55, 0.76)$, and 12% and 16% for $z_{abs} \in (0.76, 1)$. The values corresponding to separate REW bins are always a few times smaller. Therefore, the limited amount of duplicates in the reference samples is not expected to introduce relevant biases.

Occasionally, the number of QSOs with absorbers are matched to fewer than N_{ref} reference QSOs. This effect has been neglected since the incidence of such cases is very low, considering the size of the samples (listed in Table 3.1), as only 0, 2, and 5 (at the most) absorbing QSOs are matched to less than N_{ref} QSOs, in the three z_{abs} bins in increasing

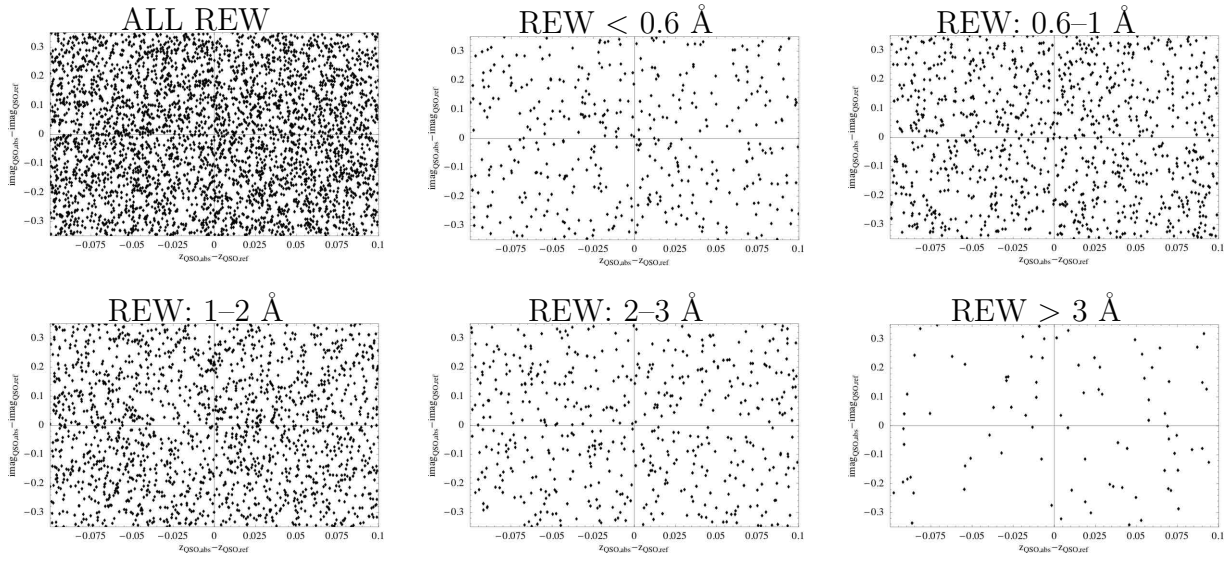

Figure 3.4: Difference of z_{QSO} and i-band magnitude for non-absorbing reference QSOs vs absorbing QSOs is plotted in various REW intervals for $z_{abs} \in (0.37, 0.55)$.

order, respectively.

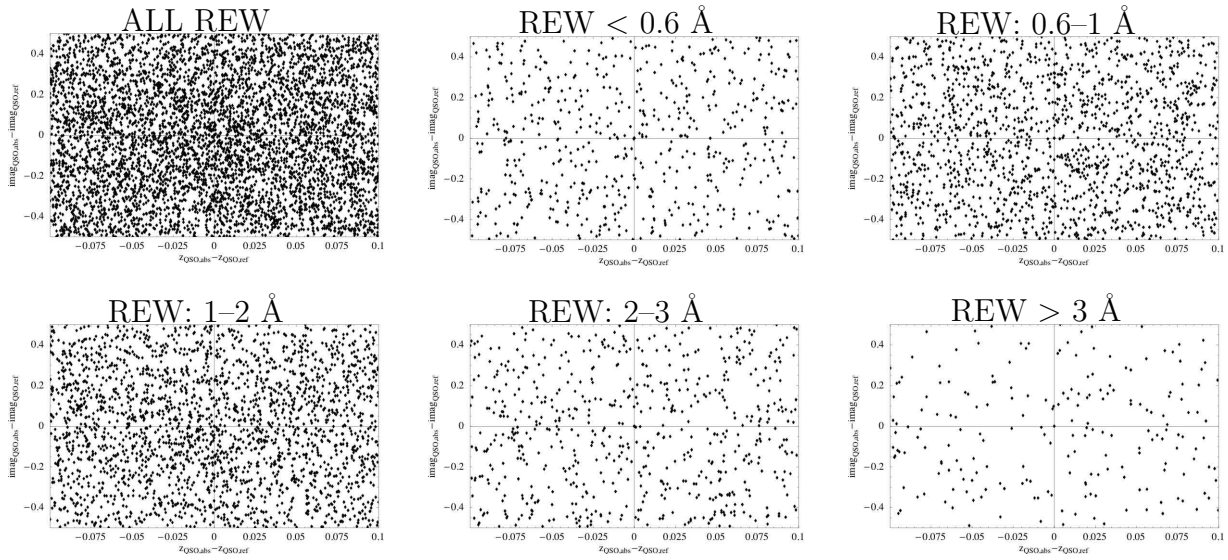

Figure 3.5: Difference of z_{QSO} and i-band magnitude for random reference QSOs vs absorbing QSOs is plotted in various REW intervals for $z_{abs} \in (0.55, 0.76)$.

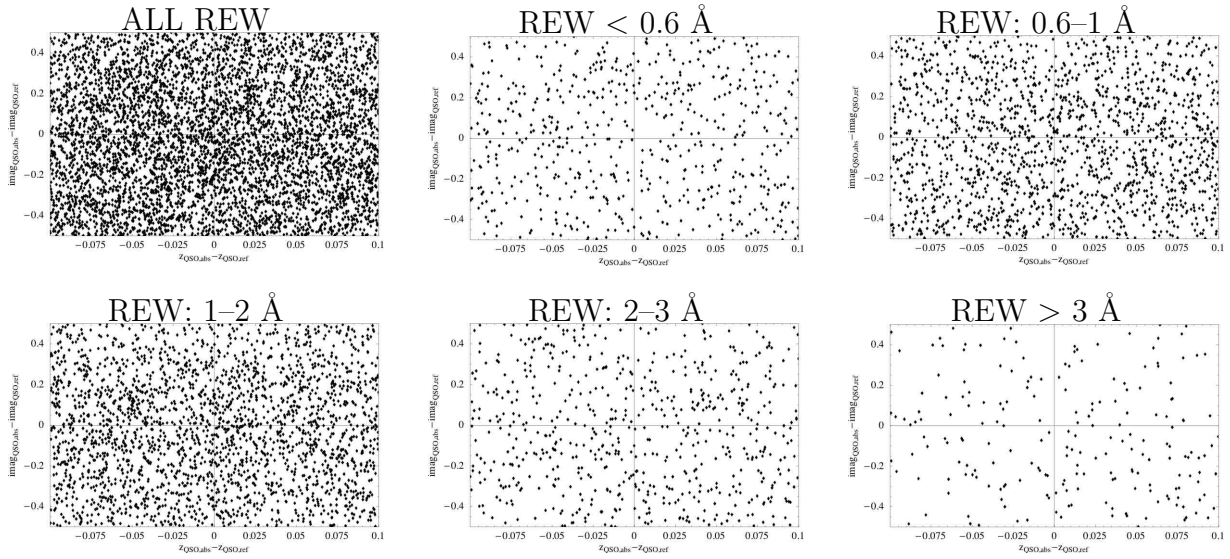

Figure 3.6: Difference of z_{QSO} and i-band magnitude for non-absorbing reference QSOs vs absorbing QSOs is plotted in various REW intervals for $z_{abs} \in (0.55, 0.76)$.

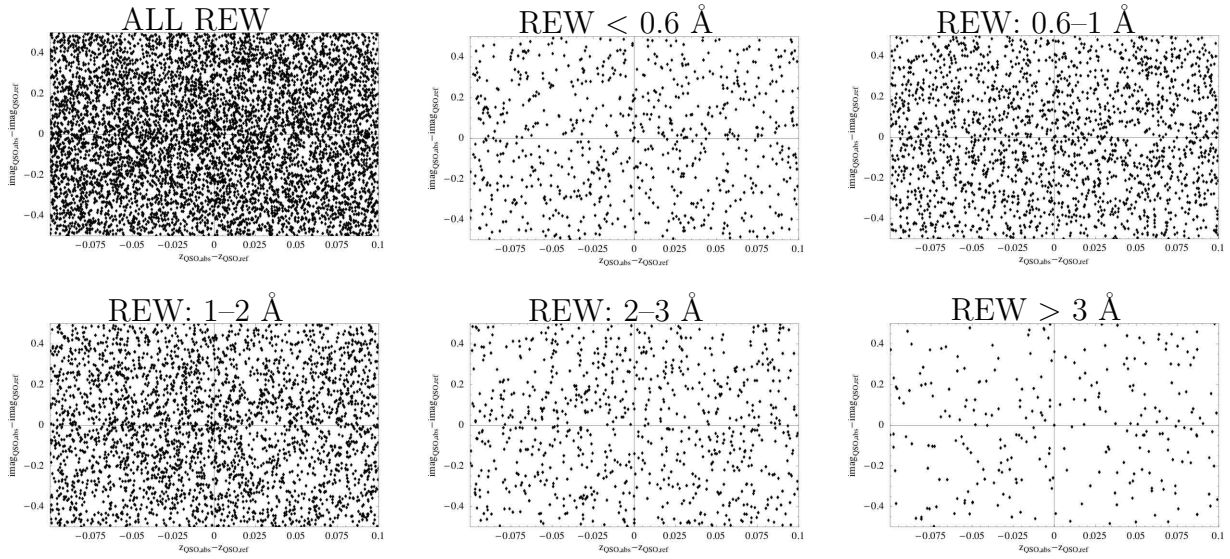

Figure 3.7: Difference of z_{QSO} and i-band magnitude for random reference QSOs vs absorbing QSOs is plotted in various REW intervals for $z_{abs} \in (0.76, 1)$.

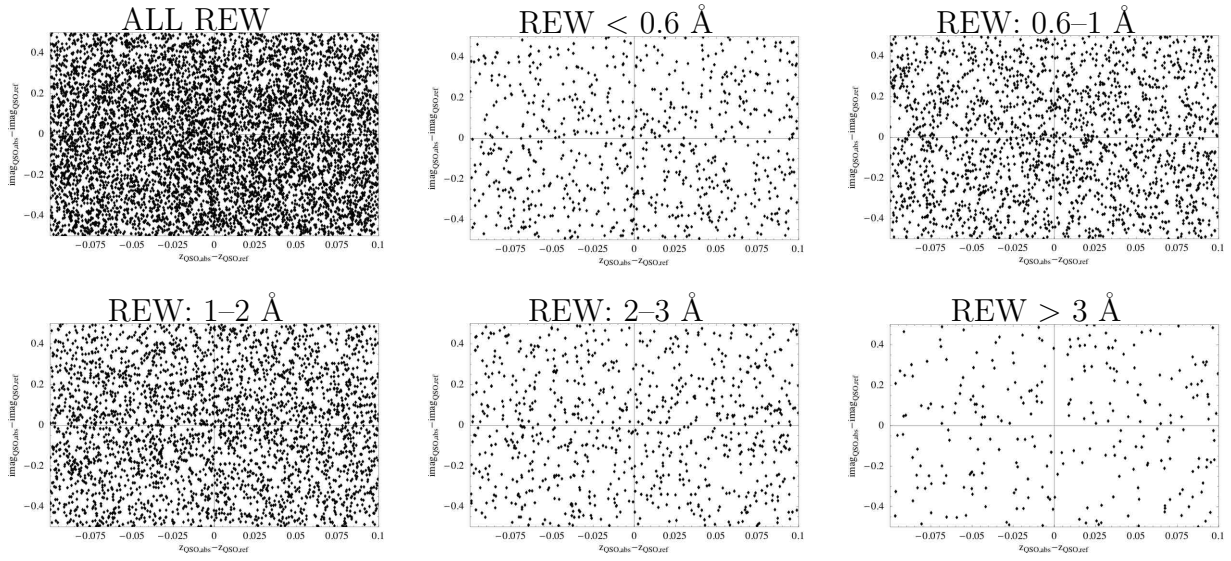

Figure 3.8: Difference of z_{QSO} and i-band magnitude for non-absorbing reference QSOs vs absorbing QSOs is plotted in various REW intervals for $z_{abs} \in (0.76, 1)$.

3.1.3 QSO Glare Effect

Galaxy counts are affected by incompleteness from various sources. The one addressed in this section is due to the glare of QSOs around which galaxies are being studied. It is cause for concern because it affects galaxy detection exactly where the signal of association of galaxies with MgII absorbers is the strongest.

The glare from the QSO (and its host galaxy, if observed) make the detection of nearby galaxies more difficult, and the number counts of galaxies are underestimated, especially in the neighborhood of bright QSOs. Moreover, the sky levels in the vicinity of bright objects are systematically overestimated in the SDSS DR4 (see [Adelman-McCarthy et al. 2006] and references therein), biasing the classification and photometry of faint objects. The consequences of such effects should be carefully evaluated when correlating bright QSOs with the position of neighboring faint galaxies.

The enhanced incompleteness of fainter sources with respect to brighter ones may mimic dependences of galaxy parameters on the angular distance from QSOs or on the REW. For example, if larger REWs are associated with brighter absorbing galaxies, a naive interpreta-

tion of the galaxy distribution around QSO sight-lines may indicate that stronger absorption lines occur at smaller impact angles. While a REW-distance dependence may actually exist, first it needs to be disentangled from the artifact created by the QSO-glare. Another example involves the comparison of strong with weak absorbers. Since the weak ones need a higher signal-to-noise ratio to be detected, the average QSO magnitude is brighter (see Fig. 3.1), which may lead to the appearance that weaker absorbers are caused by more luminous galaxies and/or at greater impact parameters.

3.1.3.1 Glare Correction Method

Absorbing galaxies are identified by the excess in number counts with respect to the background sample and they are predominantly found in the region affected by the QSO glare (as shown in § 3.1.4.1). In order to correct for the incompleteness of galaxy counts induced by the QSO glare, the average background density of galaxies is estimated using the random QSO reference sample. In fact, such a reference is expected to be biased in proximity of QSO sight-lines only by the glare effect, and otherwise probe a flat average density of sources.

The corrections to apply to galaxy densities around QSOs with absorbers are not simply those needed to boost the reference galaxy underdensities at small impact-angles from QSOs to the levels in the large-angle limit. In fact, the incompleteness of galaxy counts depends also on the magnitude distribution of galaxies in each angular bin, enhancing the number counts of fainter populations more than brighter ones (for a given QSO magnitude).

The method described herein is meant to provide an approximate solution to the QSO-glare problem and sensible estimates for the magnitude of the corrections. It makes a series of assumptions meant to sacrifice accuracy for simplicity, while retaining general consistency with the data. The high statistical noise due to low number counts of galaxies at small angles from QSO sight-lines limits greatly the possible accuracy, so conclusions from more complicated treatments to correct for the QSO-glare effect are not expected to lead to significantly different results. Note that the instrumental detection incompleteness of faint-end objects is not accounted for by the QSO-glare correction, but an appropriate magnitude threshold may help achieve complete samples of galaxies.

In the convention adopted in this section only, tildes are superposed over the quantities which are observed, while the (unknown) glare-free counterparts are tilde-free. Given same conditions for an observational apparatus, the average observed apparent magnitude $\tilde{\mu}$ of a set of galaxies depends on both the galaxy population and the glare-induced deficiency. Since the QSO glare affects a larger proportion of fainter rather than brighter objects, $\tilde{\mu}$ tends to be brighter than the unbiased average magnitude μ of the galaxy sample. Herein, computations of average magnitudes are not weighted by the measured errors in order to avoid biasing to the advantage of brighter objects. Moreover, magnitudes must be treated as observed, i.e., not corrected by Galactic extinction.

The observed brightness distribution of galaxies is generally not described in terms of a Gaussian probability density function $g(m|\mu, s)$, but this may still be employed to parametrize the glare-free detection of galactic magnitudes m (distributed with variance s^2) in a simplistic manner:

$$g(m|\mu, s) = \frac{1}{\sqrt{2\pi}\, s} \exp\left[-\frac{(m-\mu)^2}{2s^2}\right]. \tag{3.1}$$

A simple model for the fraction $f(m|\{p_*\})$ of detectable galaxies of magnitude m within a given angular distance interval from QSOs may be described by the following function (given a set of parameters $\{p_*\}$ depending on the instrument and the average photometric properties of QSOs):

$$f(m|m_*, s_*) = \frac{1}{1 + \exp\left(\frac{m-m_*}{s_*}\right)}. \tag{3.2}$$

Given the parameters m_* and s_* (describing the typical cutoff and the magnitude range over which the fraction of detectable galaxies vanishes, respectively), the observed galaxy magnitude distribution $\tilde{g}(m|\mu, s)$ is

$$\tilde{g}(m|\mu, s) = g(m|\mu, s)\, f(m|m_*, s_*). \tag{3.3}$$

Since the observed $\tilde{g}(m|\mu, s)$ depends on the unknown values μ and s, in principle these should be determined by solving simultaneously the following equations involving the measured $\tilde{\mu}$ and $\tilde{s}$ (for given values of m_* and s_*):

$$\begin{cases} \tilde{\mu} = \tilde{A}^{-1}(\mu, s) \int_{-\infty}^{\infty} m\, \tilde{g}(m|\mu, s)\, dm \\ \tilde{s}^2 = \tilde{A}^{-1}(\mu, s) \int_{-\infty}^{\infty} (m-\tilde{\mu})^2\, \tilde{g}(m|\mu, s)\, dm \end{cases} \tag{3.4}$$

where $\tilde{A}(\mu, s) = \int_{-\infty}^{\infty} \tilde{g}(m|\mu, s)\, dm$. Reinterpreting $f(m|m_*, s_*)$ as $f(m - m_*|s_*)$, it is clear that $\tilde{A}$ describes the convolution of g with f, i.e., $\tilde{A} = g \otimes f$.

Solving the system of equations (3.4) proved to be computationally intensive. For faster processing, the value for s was assumed to be the same at all angles and well represented by the average of $\tilde{s}$ at large angles (between 20 and 30 arcsec, where the QSO-glare effect was deemed negligible). Assuming $s_* \sim 1$ (which seemed a sensible value by comparing $\tilde{g}$ with the observed brightness distribution of galaxies – see Fig. 3.9), an initial value for m_*, and measuring $\tilde{\mu}$, a solution for μ was found numerically. The process was iterated varying m_* until the corrected projected number density of galaxies surrounding random reference QSOs (corresponding to specific z_{abs} and REW intervals in the absorber sample) reproduced the large-angle average (from 20 to 30 arcsec) with a tolerance of 1%, or the value for m_* became greater than 30 (i.e., much larger than $\tilde{\mu}$, in which case the QSO-glare effect was considered negligible). Such a procedure was repeated for all angular bins as well as z_{abs} and REW intervals.

Once m_* was found from the random QSO reference sample (referring to specific z_{abs}, REW, and angular bins), $f(m|m_*, s_*)$ was used to solve for μ (and s, if Eqs. 3.4 were solved for) corresponding to galaxies around MgII-absorbed QSO (within the same z_{abs}, REW, and angular intervals). In the general case of galaxy counts of galaxies brighter than a magnitude threshold m_{cut}, the factors β correcting for the QSO glare-induced incompleteness are computed as

$$\beta = \frac{\int_{-\infty}^{m_{cut}} g(m|\mu, s)\, dm}{\int_{-\infty}^{m_{cut}} \tilde{g}(m|\mu, s)\, dm}, \tag{3.5}$$

which equals $\tilde{A}^{-1}$ when no magnitude cuts are applied ($m_{cut} \to \infty$). Note that β can only be greater than one; if statistical fluctuations lead to reference galaxy number densities greater than the assumed background average, then m_* tends to infinity and no correction is applied. In such cases, the above mentioned tolerance limit of 1% cannot be accounted for.

The resulting factors β are generally different around QSO samples corresponding to different REW and z_{abs} interval, even when they refer to the same angular bin. This is due to the variation of μ and s of galaxy populations as well as the average reference QSO brightness (inbuilt in m_*). Thus, the definition of reference QSOs matching the magnitudes

of QSOs with absorbers in different subsets assures that the neighborhood of a sample of bright QSOs (in which weak REWs are measured more often) gets more strongly corrected than near fainter QSOs (where mostly strong REWs are found).

The glare correction is performed using galaxy magnitudes in the r-band, which provides a straightforward computation of β from Eq. 3.5 when considering an r-band magnitude cut. As expected, the values for m_* increase at larger angles from the QSO position. A sample of m_* and β values are listed in Table 3.2 as a function of angular and REW intervals for $z_{abs} \in$(0.37, 0.55) and without magnitude cut on galaxies. The same Table also includes average background galaxy densities around random QSOs, computed averaging galaxy counts (weighted by their errors) between 20 to 30 arcsec from QSO sight-lines. Corrections for galaxies around reference QSOs without MgII absorbers share the same values for m_*, since the average photometric properties of such QSOs have been set to be the same as those with absorbers. The measured average magnitude $\tilde{\mu}$ and the reconstructed μ are shown as a function of angular distace for each REW interval in Fig. 3.10 and Fig. 3.11, respectively, for absorbers within the lowest redshift bin (0.37, 0.55).

3.1.4 Sky-Projected Distribution of Galaxies Around QSO Sight-Lines

Neighboring galaxies classified as "primary", i.e., the best version of (duplicate) objects, are extracted from the SDSS catalog within 30 arcsec from QSO sight-lines with MgII absorbers, leading to 3216, 5149, and 5982 galaxies for the three z_{abs} bins in increasing order. Note that the increment in galaxy number counts with redshift is only due to the increasing size of the absorber sample. Unfortunately, the shallow SDSS imaging does not allow for reliable estimates of photometric redshifts for galaxies in the redshift range of MgII detection. As a consequence, the analysis of MgII associated galaxies is limited to sky-projected distributions.

Overlapping regions are statistically negligible: only 18 pairs of QSOs (out of which 6 with MgII absorbers) are found separated by less than 30 arcsec (with the smallest separation being 9 arcsec). In the rest of this paragraph, a specific case is briefly described to illustrate some of the typical uncertainties with a concrete example. One of the close QSO pairs has an angular separation of 22 arcsec and includes three absorbers at redshift 1.21 (with REW

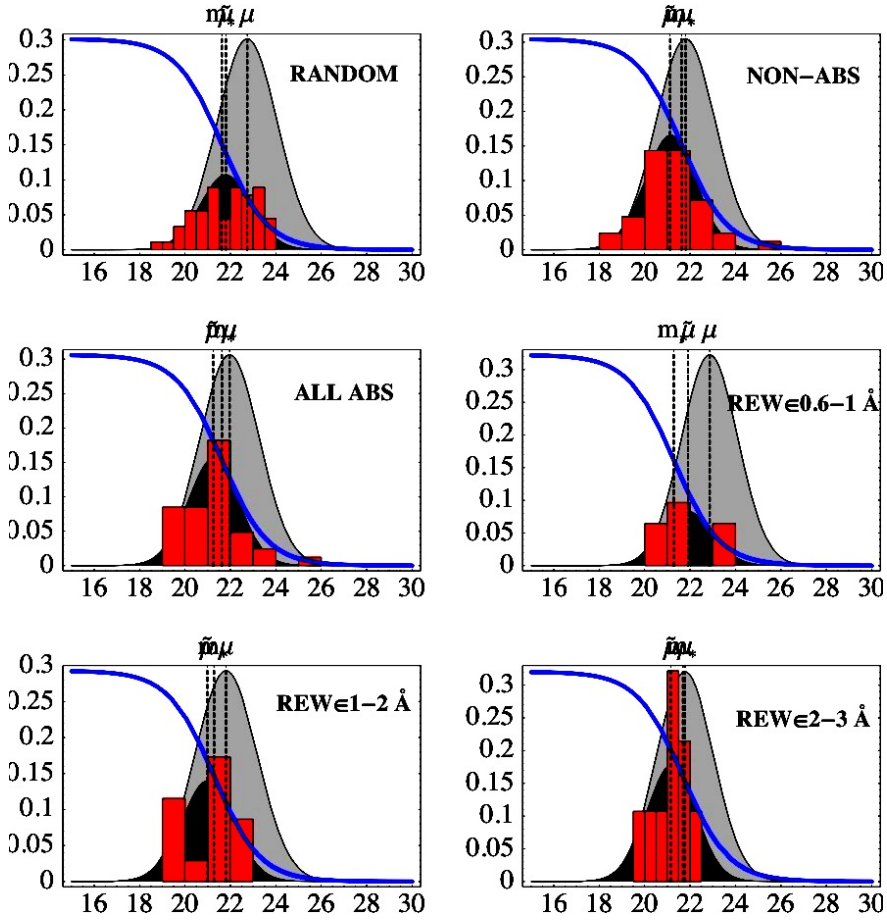

Figure 3.9: Glare-correction applied to galaxies from 2 to 4 arcsec from QSOs belonging to different subsets: random, non-absorbing, absorbing (all REW), and absorbing REWs in the ranges 0.6–1 Å, 1–2 Å, 2–3 Å, presented in the above panels from top-left to bottom-right. The observed galaxy magnitude distribution $\tilde{g}$ (indicated by the dark-gray shaded area overlapped by the red data histogram), with average $\tilde{\mu}$, originates from the glare-corrected distribution g (depicted by the light-gray region) of galaxy magnitudes with average μ. Dashed lines identify μ, $\tilde{\mu}$, and m_*, though they are often too close for clear labeling. In this example, no magnitude cuts are applied to galaxies. Shaded curves and histograms subtend unit areas, so the blue curve describes f as defined in Eq. 3.2 but normalized by $(\sqrt{2\pi}s)^{-1}$ (for plotting purposes only).

Table 3.2: Set of values (m_*, β) in r-band around QSOs containing absorbers within specified REW bins and angular distance intervals from QSOs. The parameter m_* identifies a typical cutoff in the fraction of detectable galaxies due to the QSO glare, while β^{-1} measures the observed fraction of galaxies. Only absorbers with $z_{abs} \in (0.37, 0.55)$ are included, and no magnitude cut is applied to galaxies. Also, the background galaxy densities $\langle N \rangle$ around random QSOs (averaged between 20 to 30 arcsec) are expressed in units of counts per arcmin^{-2}. As expected, m_* increases while β decreases at larger angles from the QSO position. The particularly high value for β in the first angular and REW bins corresponds to especially small m_*, which reflects the fact that the weakest absorbers are detected in the brightest QSOs (and thus affected by the strongest glare effect). Furthermore, the first angular and REW bins contain the smallest number of galaxies for which a glare correction is computed, and, consequently, it is affected by larger statistical fluctuations.

	0.16–0.6 Å	0.6–1 Å	1–2 Å	2–3 Å	3–8.5 Å	ALL REWs
$\langle N \rangle$ arcmin^{-2}	4.9	4.9	5.2	4.8	4.4	5.0
2–4 arcsec	(20.1, 20.9)	(21.3, 4.4)	(21.3, 2.5)	(21.7, 2.1)	n/a	(21.6, 2.3)
4–6 arcsec	(23.1, 1.5)	(25.5, 1.0)	(23.7, 1.2)	(26.0, 1.0)	n/a	(25.0, 1.1)
6–8 arcsec	(>30, 1.0)	(29.0, 1.0)	(>30, 1.0)	(>30, 1.0)	(>30, 1.0)	(26.0, 1.0)

of 1.4 Å) in one spectrum, and 0.95 and 1.32 (with REW of 0.4 Å and 0.7 Å, respectively) in the other spectrum. The redshift of the first QSO matches the absorption redshift in the second one (at $z_{abs} = 1.32$). Thus, the absorption is likely to arise in a galaxy associated with the QSO. The SDSS imaging is not sufficiently deep to detect galaxies at these redshifts. Fig. 3.12 shows the QSO at redshift 1.74 in the center, while the other QSO, also identified by a box, lies in the upper-right (NW) quadrant. The circled object in the bottom-right (SW) quadrant is 20 arcsec away from the central QSO, and it is classified as a star. However, the "star" classification has been found to be incorrect about 40% of the time for $21 < r < 21.8$ [Mandelbaum et al. 2005], and the above mentioned star has $r = 21.56$. The suspicion that such a star is a misclassified faint galaxy is further intensified by the photometric redshift

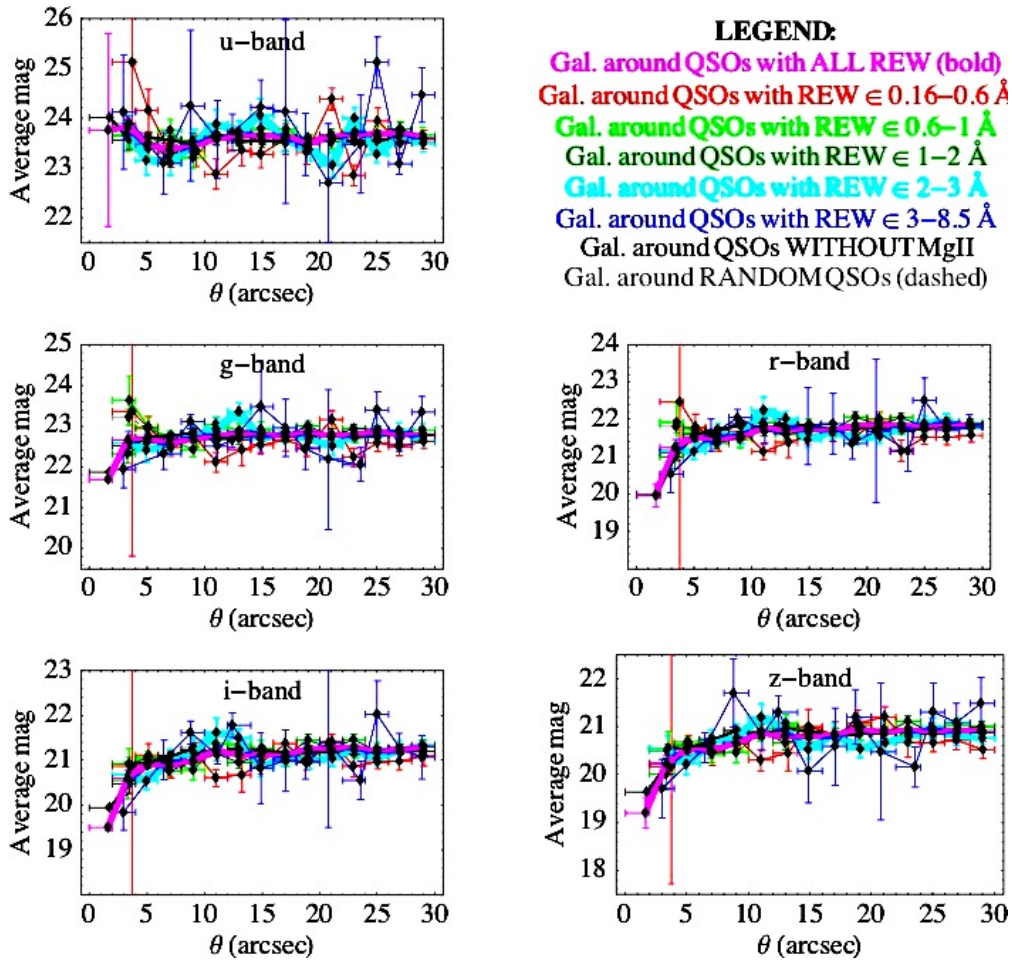

Figure 3.10: The average observed u, g, r, i, z-band magnitudes $\tilde{\mu}$ of galaxies around various QSO sets (color-coded as described in the Figure) are shown as a function of angular distance from QSOs, for z_{abs} within (0.37, 0.55). Errors on the small number counts of galaxies in the first few angular bins are computed from the Student-t distribution requiring a confidence level of 68%. Only statistical errors on the averages are shown in the Figure. For an estimate of the measured galaxy magnitude errors, 68% of all galaxies report errors less than 1.06, 0.32, 0.19, 0.18, 0.49 magnitudes in u, g, r, i, z bands, respectively.

estimate[4] of 0.64 ± 0.32, which is marginally consistent with the absorption at $z_{abs} = 0.95$.

[4]The Photoz table recently loaded in the SDSS archives applies photometric redshift estimates to all objects as if they were galaxies. Thus, such values can still be considered meaningful if misidentified objects actually are galaxies.

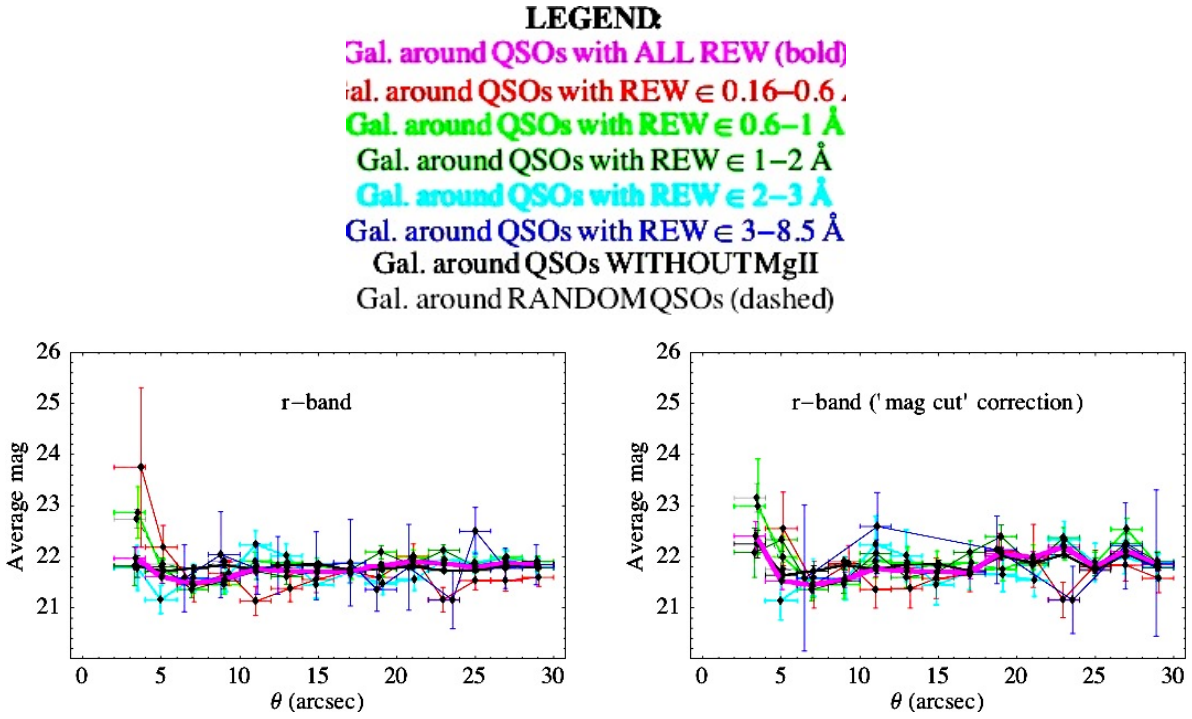

Figure 3.11: The reconstructed r-band average magnitudes μ are shown in the Figure for both cases without a magnitude threshold (left panel) and requiring galaxies brighter than $r = 21.5$ (right panel), for the lowest z_{abs} interval (0.37, 0.55). Note that the magnitude cut is not applied to $\tilde{g}$ but only to the computation of the correction factor.

While the impact parameter for this galaxy to the QSO LOS is fairly large (almost 160 kpc) compared to the typical absorber, other (undetected) galaxies in the environment of the misclassified galaxy may be responsible for the measured absorption as well.

The comparison between the number counts of galaxies around QSO sight-lines with MgII detections in their spectra and those around reference QSOs is described first in terms of average galaxy number densities and then by estimating the QSO-galaxy cross-correlation function. Results are separated in REW and z_{abs} intervals, and evaluations of the errors are described in § 3.1.4.4.

Since glare correction factors β depend on angular distances and not on physical impact parameters, glare-corrected number counts in terms of projected distances are computed by summing the factors β of all galaxies within impact parameter bins, and plotted by weighting

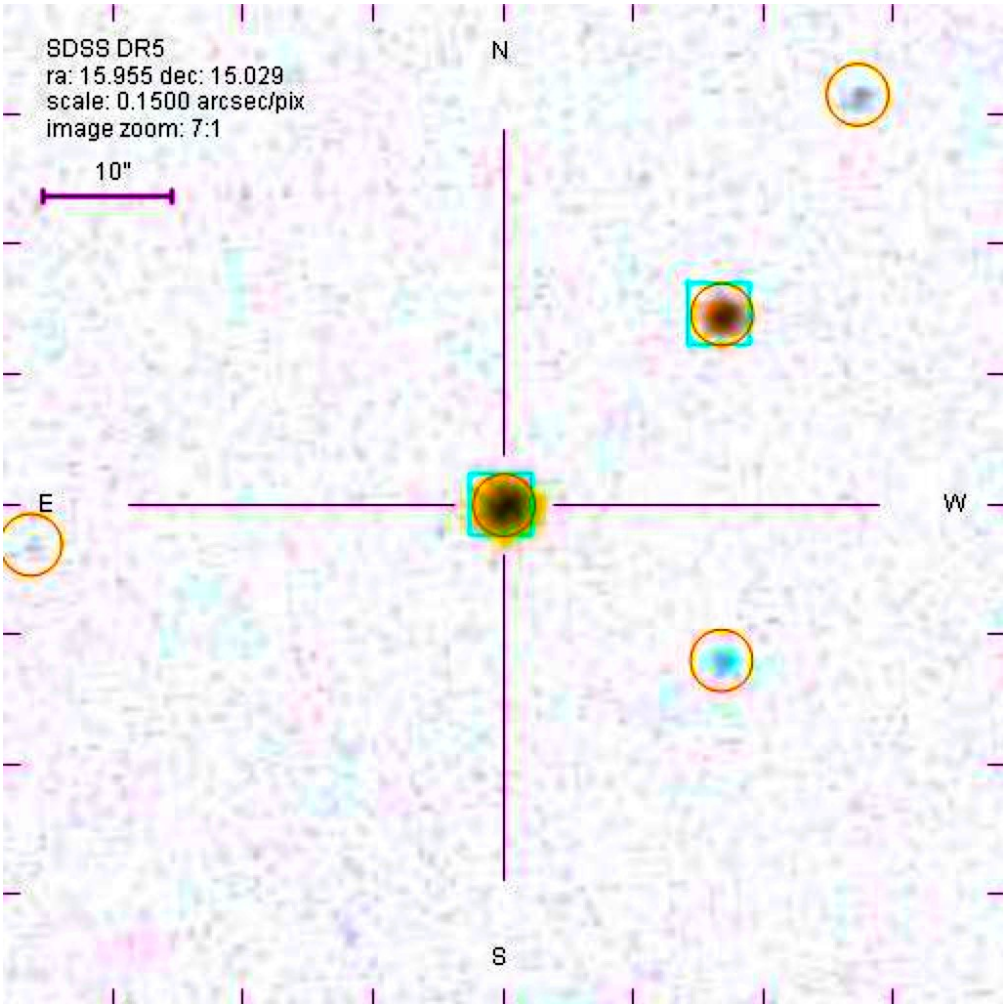

Figure 3.12: A pair of QSOs (identified by boxes) is separated by 22 arcsec, and three MgII absorbers are found in their spectra . The redshift of the QSO in the NW quadrant matches the redshift of one of the absorbers detected in the spectrum of the QSO at the center, indicating the absorbing galaxy might be associated with the off-center QSO. Further motivations described in the text suggest that the star-like object on the bottom-right hand side might actually be a faint galaxy responsible for the MgII absorption (or, more likely, associated with undetected absorbing galaxies).

the average distances by the number counts (in Fig. 3.15–3.21). Since $\theta_{\rm max}$ defines a conical region while a fixed maximum impact parameter selects a cylindrical volume, depletion of

galaxies at impact parameters between $\theta_{\max} D_A(z_{abs,\min})$ and $\theta_{\max} D_A(z_{abs,\max})$ is avoided by setting the maximum projected distance to $\theta_{\max} D_A(z_{abs,\min}) \sim 150$ kpc, where D_A denotes the angular-diameter distance, $\theta_{\max} = 30$ arcsec, and $z_{abs,\max}$ and $z_{abs,\min}$ refer to the limits of the absorbing redshift interval under consideration.

Another reason for incomplete galaxy counts may arise when the search angle around QSOs (set to 30 arcsec) extends beyond the surveyed area. However, such an effect is neglected because of the small angular radius chosen, and the validity of this approximation is confirmed by the flat density profiles (within statistical uncertainties) observed in the limit of large angles (as shown in the Figures of § 3.1.4.1).

3.1.4.1 Average Galaxy Counts

The average number of galaxies within angular and impact parameter bins is computed for each MgII absorbing QSO subset within different REW and z_{abs} intervals. Since contamination from galaxies not associated with MgII systems is expected to affect the neighborhood of absorbed and reference QSOs similarly, the signal from absorption-related galaxies is inferred from the difference with respect to the reference levels.

Considering only galaxies brighter than a certain threshold increases errors on galaxy counts as well as contamination by foreground galaxies not associated with MgII absorbers, since a larger proportion of galaxies at redshift $z > 0.37$ (with respect to $z < 0.37$) is removed. On the other hand, if errors are much smaller than the signal from absorbing galaxies, it is worth investigating a magnitude limited sample, which limits galaxy detection incompleteness (including the one due to the QSO glare) and the occurrence of misidentifications of stars as galaxies (and vice versa). For example, it has been found that stellar contamination in a galaxy sample is negligible for $r < 21$ and it amounts to 7% for objects with $21 < r < 22$, while the fraction of galaxies misclassified as stars may reach 40% within $21 < r < 21.8$ [Mandelbaum et al. 2005].

Comparing galaxies within a region scanned by both SDSS and COMBO-17 surveys, the completeness of SDSS galaxies is estimated to be about 80% for galaxies brighter than $r = 21.5$ (see Fig. 3.13), with only a few percent contamination by stellar objects. Such a magnitude threshold is applied and its effects are investigated. For comparison purposes,

results are presented including as well as excluding the QSO-glare correction.

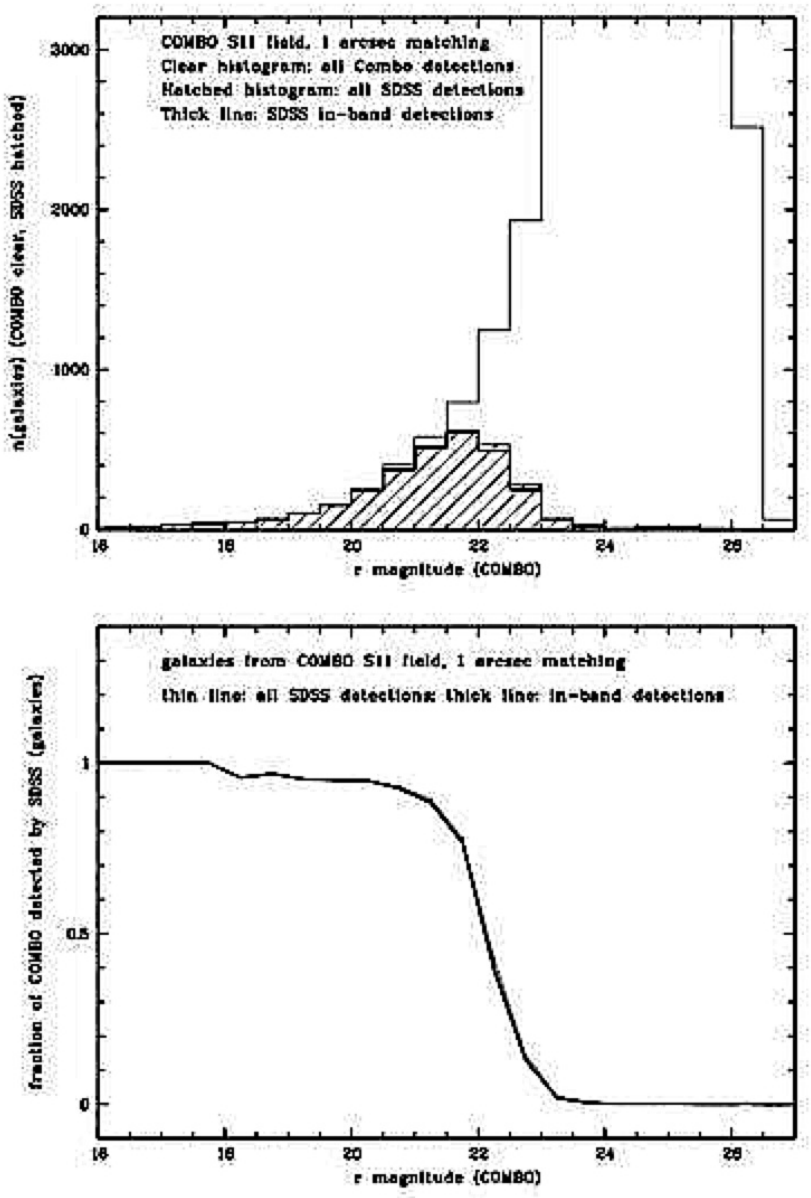

Figure 3.13: The comparison between SDSS and COMBO-17 galaxies allows an estimate of the completeness for detection of SDSS galaxies (both of the panels in this Figure are extracted from the SDSS website). The top panel presents shaded and clear histograms for the r-band magnitude distribution of galaxies in the SDSS and COMBO-17, respectively. The lower panel shows the fraction of COMBO-17 galaxies detected by the SDSS as a function of magnitude.

As shown in Table 3.3, the chance to detect a galaxy within 10 arcsec from QSO sight-lines almost doubles for MgII absorbers detected at $z_{abs} \in (0.37, 0.55)$, and it is higher for stronger rather than weaker systems. Such effects are even more pronounced when only galaxies brighter than $r = 21.5$ are considered.

Table 3.3: The incidence of galaxy detections per QSO line-of-sight as a function of different angular and REW intervals is presented below for three different QSO samples: MgII-absorbing QSOs (ABS) within $z_{abs} \in (0.37, 0.55)$, and the corresponding reference QSOs without MgII detections (NonAbs) as well as random (RAN). Entries within brackets denote galaxies brighter than $r = 21.5$ only.

$\Delta\theta$ (arcsec)	QSOs	0.16–0.6Å	0.6–1Å	1–2Å	2–3Å	3–8.5Å	ALL REWs
0–10	ABS	0.60 (0.32)	0.59 (0.27)	0.63 (0.33)	0.75 (0.40)	0.71 (0.35)	0.63 (0.32)
	NonAbs	0.34 (0.14)	0.31 (0.11)	0.32 (0.11)	0.30 (0.15)	0.21 (0.08)	0.33 (0.13)
	RAN	0.38 (0.14)	0.37 (0.14)	0.35 (0.14)	0.37 (0.14)	0.39 (0.15)	0.35 (0.13)
10–20	ABS	1.54 (0.73)	1.55 (0.57)	1.36 (0.51)	1.40 (0.52)	1.53 (0.65)	1.44 (0.55)
	NonAbs	1.19 (0.43)	1.22 (0.42)	1.16 (0.40)	1.05 (0.40)	1.16 (0.38)	1.22 (0.44)
	RAN	1.16 (0.38)	1.30 (0.46)	1.18 (0.41)	1.18 (0.41)	1.38 (0.35)	1.22 (0.43)
20–30	ABS	2.15 (0.88)	2.15 (0.76)	2.29 (0.80)	2.07 (0.77)	1.94 (0.65)	2.20 (0.79)
	NonAbs	2.12 (0.74)	1.96 (0.70)	1.92 (0.69)	1.94 (0.68)	1.86 (0.67)	1.92 (0.71)
	RAN	1.98 (0.68)	2.01 (0.72)	1.95 (0.69)	1.84 (0.64)	1.87 (0.73)	1.97 (0.70)
0–30	ABS	4.28 (1.93)	4.29 (1.60)	4.27 (1.63)	4.23 (1.70)	4.18 (1.65)	4.27 (1.66)
	NonAbs	3.65 (1.31)	3.48 (1.23)	3.40 (1.20)	3.29 (1.22)	3.24 (1.13)	3.47 (1.28)
	RAN	3.52 (1.20)	3.69 (1.32)	3.48 (1.23)	3.39 (1.19)	3.64 (1.24)	3.54 (1.26)

The average number density of galaxies per line-of-sight as a function the angular and distance impact parameters from the QSO sight-lines is shown in Fig. 3.14–3.18 for different REW and z_{abs} intervals, including and excluding the galaxy magnitude threshold $r < 21.5$; glare-corrected profiles are also plotted in the lowest z_{abs} bin. Horizontal bars refer to the extent of the bin sizes, and points are drawn at the average angles or impact parameters within each bin. Centroiding and astrometric calibration errors (of the order of 0.1 arcsec) are much smaller than the bins employed, so they are neglected.

The reduced galaxy density at small angles with respect to the large-angle limit for galaxies around random reference QSOs is attributed to detection incompleteness from the glare of QSOs. Galaxy counts around reference QSOs without MgII absorbers are slightly

lower, because such sight-lines are selected *not* to have absorbers associated with them, and thus the sample is biased toward probing less dense regions than on average.

The excess of galaxies around QSO sight-lines with MgII absorbers with respect to reference QSOs is attributed to the combination of galaxies directly associated with MgII systems and others simply clustered around MgII-absorbing ones. In agreement with [Zibetti et al. 2005], most of the absorber-galaxy association is observed within 10 arcsec from QSO sight-lines, while all density profiles (corresponding to different REW intervals) tend to the same limit at large angles.

When a magnitude threshold is applied to galaxies ($r < 21.5$), number counts drop by a factor up to 2–3, but the relative trends within different REW do not change (within statistical errors).

As shown in Fig. 3.14, the QSO-glare correction generally succeeds to flatten the trend of the density profiles at small angles, while such a result is less evident in terms of projected distances (see Fig. 3.15), probably because of the presence of only a few galaxies in the very first distance bin. Profiles at different REW may be better compared in Fig. 3.16, where the observed results are zoomed in.

Galaxy density distributions in higher z_{abs} intervals are shown in Fig. 3.17–3.18. As expected, the signal from MgII-associated galaxies becomes weaker, dominated by contamination from foreground galaxies, and it practically vanishes in the magnitude-limited plots at the highest redshift interval (0.76, 1). This confirms that SDSS imaging is too shallow to detect galaxies associated with most of the detected MgII systems, so the evolution of the absorber-galaxy association with redshift cannot be assessed.

3.1.4.2 QSO-Galaxy Cross-Correlation

The QSO-galaxy cross-correlation function w_{qg} cannot be estimated by comparing the observed number of QSO-galaxy pairs with the expected one by averaging multiple random pairs from simulations. In fact, such simulations should include effects from the QSO glare, which have been corrected for by using galaxies observed around random reference QSOs. Thus, this set of QSOs is employed to estimate w_{qg} directly, and results including and excluding glare corrections are compared.

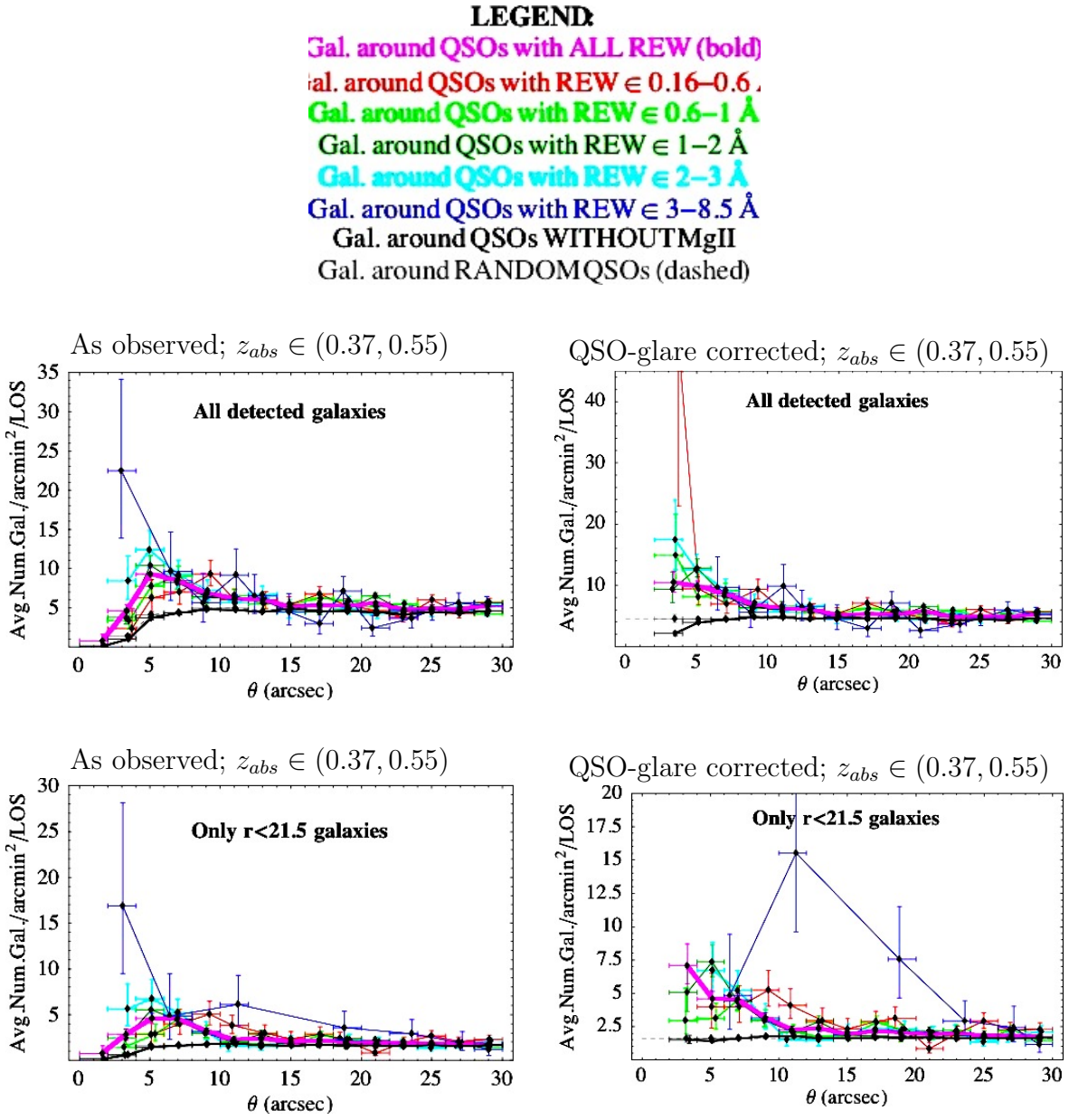

Figure 3.14: Galaxy density distributions as a function of angular impact parameters are shown subdivided in REW intervals for the lowest z_{abs} bin. Galaxy samples with and without a magnitude threshold ($r < 21.5$) are considered, and the QSO-glare correction is applied to each of these cases.

Considering the large uncertainties involved in low galaxy counts and glare corrections,

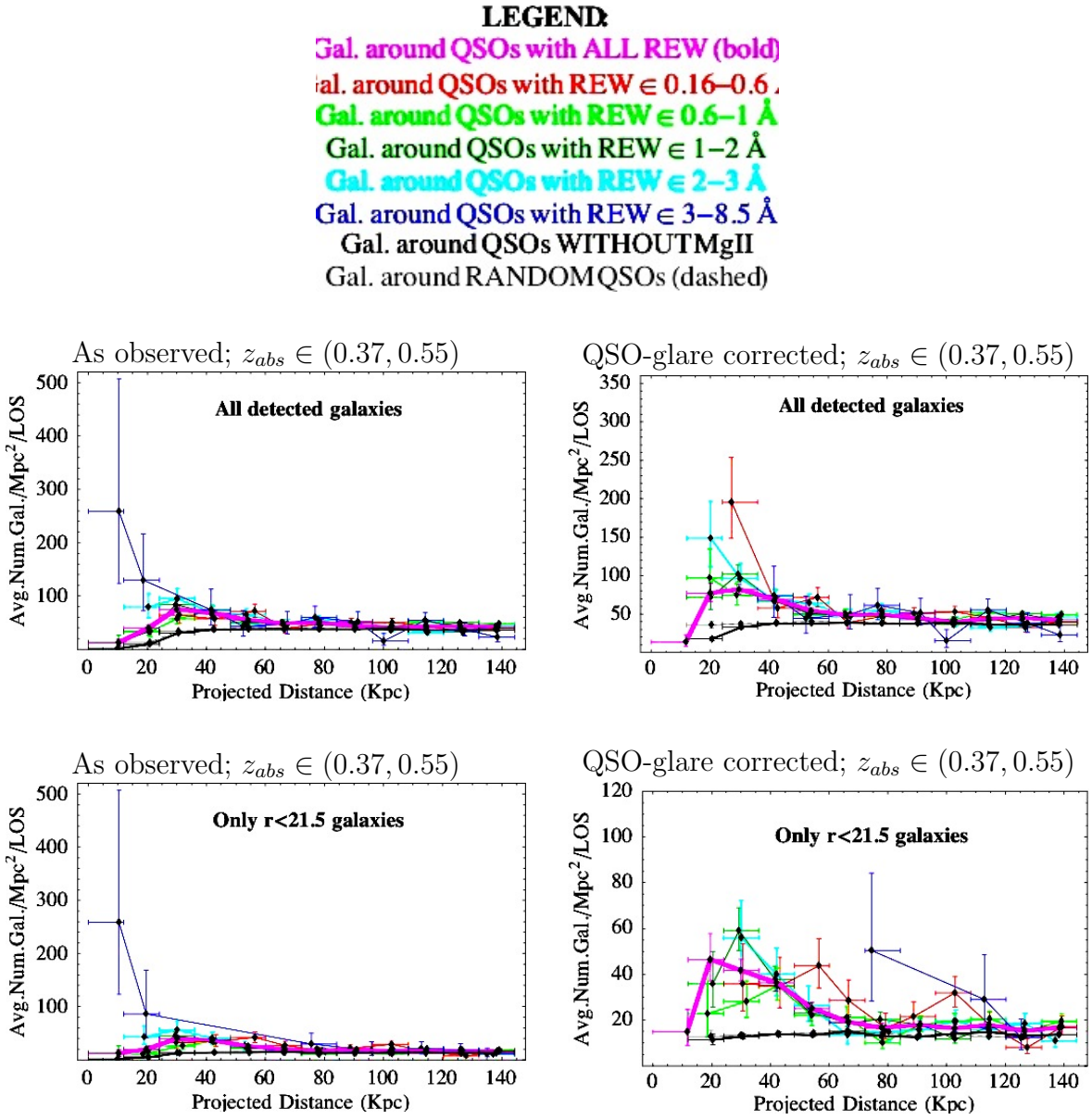

Figure 3.15: Galaxy density distributions as a function of projected distances are shown subdivided in REW intervals for the lowest z_{abs} bin. Galaxy samples with and without a magnitude threshold ($r < 21.5$) are considered, and the QSO-glare correction is applied to each of these cases.

w_{qg} is estimated simply as

$$w_{qg}(x) \approx \frac{N_{qg}(x)}{N_{ran}(x)} - 1, \tag{3.6}$$

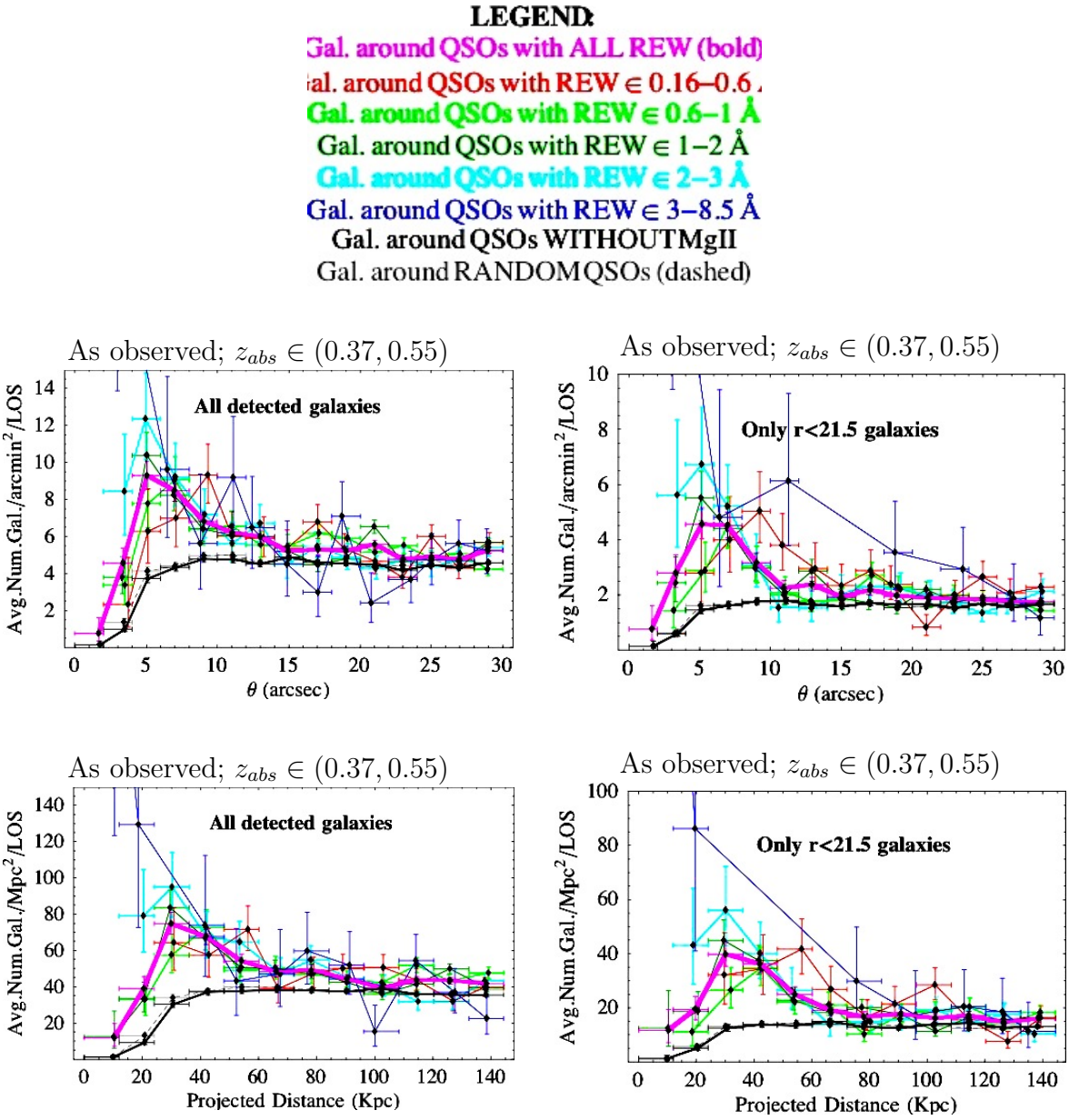

Figure 3.16: For a better view of density profiles at different REW, this Figure enlarges the observed profiles from Fig. 3.14–3.15 as a function of angles and projected distances.

where x identifies the QSO-galaxy angular or impact-parameter bins, within which the average number of QSO-galaxy pairs $N_{qg}(x)$ from galaxies around the absorbing QSO sample is compared with the expected average number of pairs $N_{ran}(x)$ from galaxies around random QSOs. When glare corrections are included, both of the above average quantities are

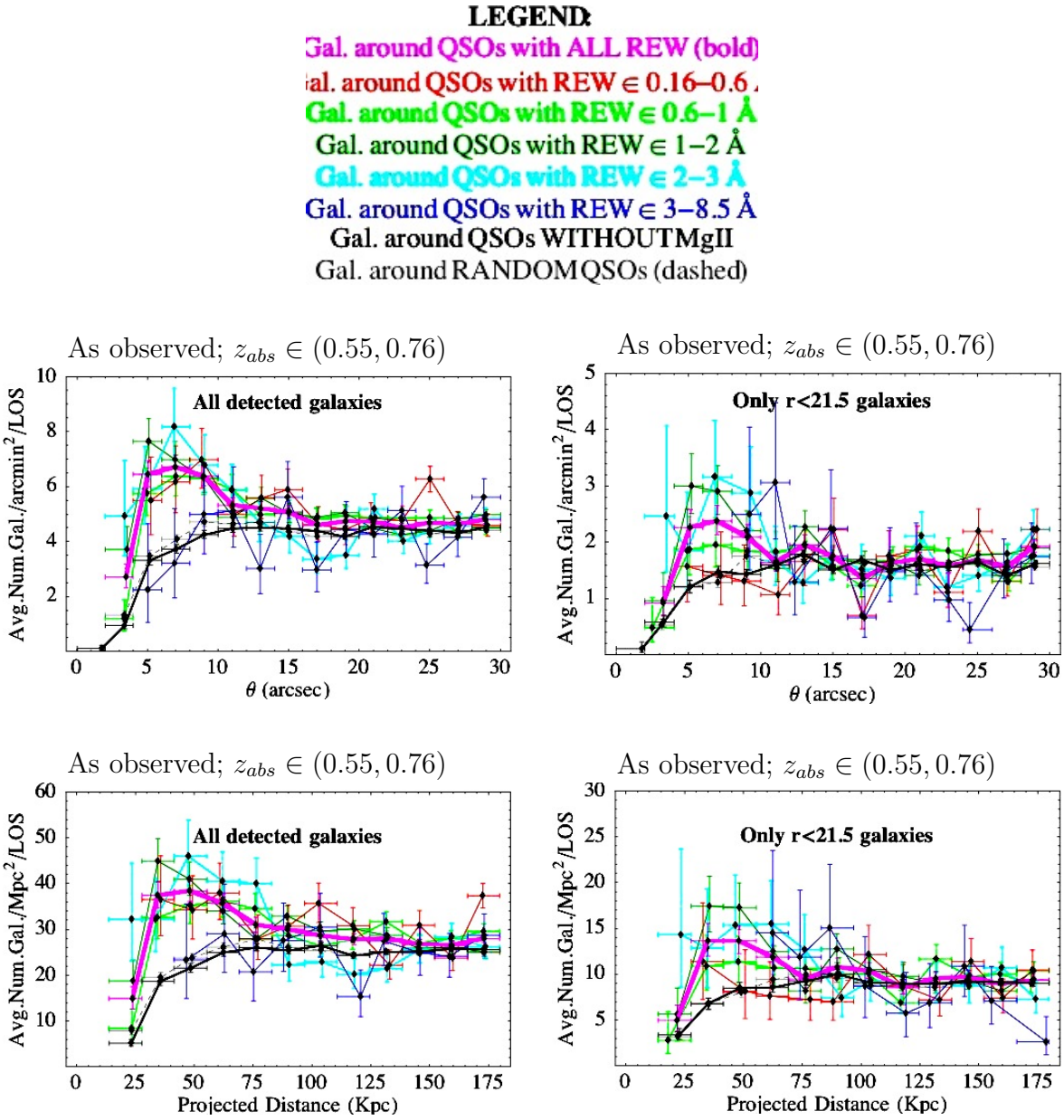

Figure 3.17: Galaxy density profiles as a function of angular and distance impact parameters are shown subdivided in REW intervals for $z_{abs} \in (0.55,\ 0.76)$, including and excluding a magnitude threshold ($r < 21.5$).

multiplied by the corresponding factors β.

Fig. 3.19–3.20 show $w_{qg}(x)$ as a function of impact parameter (angles or projected distances) and REW intervals. Glare corrections enhance by a factor of a few the average galaxy

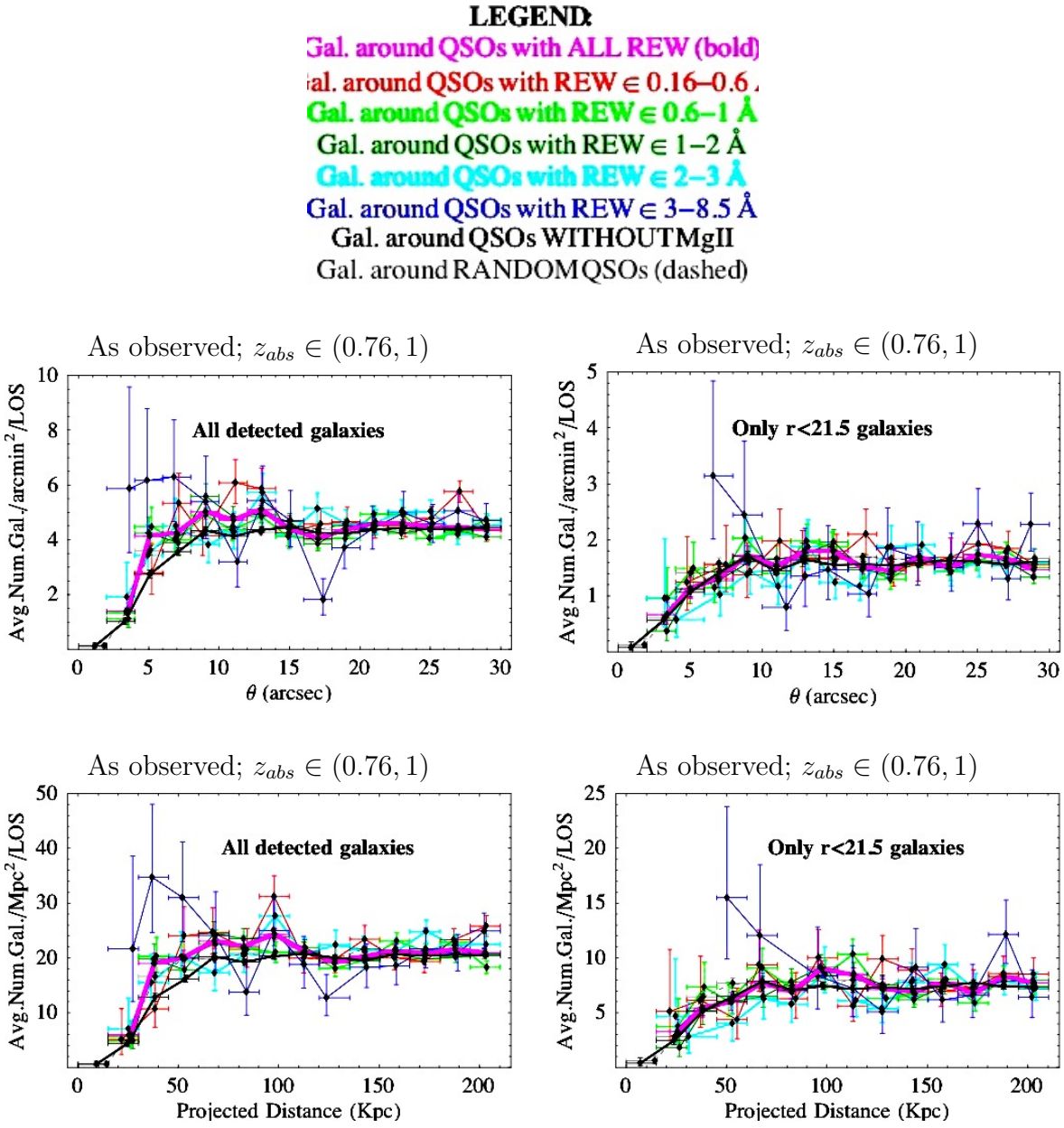

Figure 3.18: Galaxy density profiles as a function of angular and distance impact parameters are shown subdivided in REW intervals for $z_{abs} \in$(0.76,1), including and excluding a magnitude threshold ($r < 21.5$).

density profile at small angles, but similar boosts of the reference sample lead to no significant difference in the QSO-galaxy cross-correlation, apart from few peculiar cases dominated

by statistical fluctuations from small number counts. The cross-correlation function derived from the sample of galaxies subject to the magnitude threshold $r < 21.5$ is more noisy and shows a marginally stronger signal when it is estimated in terms of angles in the case of all REW. However, it is only a $\sim$ 1-σ effect at small angles, while the points referring to other REW bins are consistent with results without magnitude cuts, or obviously affected by poor statistics.

Generally, radial profiles are sharply peaked at small impact parameters, so they are fitted with a simple power-law model

$$w_{qg}(x) = \left(\frac{x}{x_o}\right)^{\nu_x}, \tag{3.7}$$

where x refers to angular or physical distances, while x_o and ν_x are fitting parameters. The χ^2 merit function is minimized with the Levenberg-Marquardt method, which searches for the minimum χ^2 moving gradually from steepest descent to quadratic minimization. Fits are not weighted by errors, otherwise the QSO-galaxy cross-correlation signal (corresponding to the smallest angles with the fewest number counts) would have been washed out.

In order to achieve more accurate and reliable results, the magnitude-limited w_{qg} (subject to large fluctuations from small counts) and noisier high-redshift intervals are not employed to estimate the best-fit parameters. Only the observed $w_{qg}(x)$ (for $z_{abs} \in$(0.37, 0.55) and without magnitude threshold) is fitted in terms of angles and distances. The best-fitting parameters for each REW interval are listed in Table 3.4, while ellipsoidal joint confidence regions (for 68% and 95% confidence levels) are depicted in Fig. 3.21.

A comparison between weak and strong absorbers is attempted in statistically significant sets (such as 0.6–1 Å and 2–3 Å), and it is inferred that the QSO-galaxy cross-correlation signal is stronger and steeper at small impact parameters for larger REW systems. Such a conclusion is drawn from the observed $w_{qg}(x)$ as a function of both angular and projected distances.

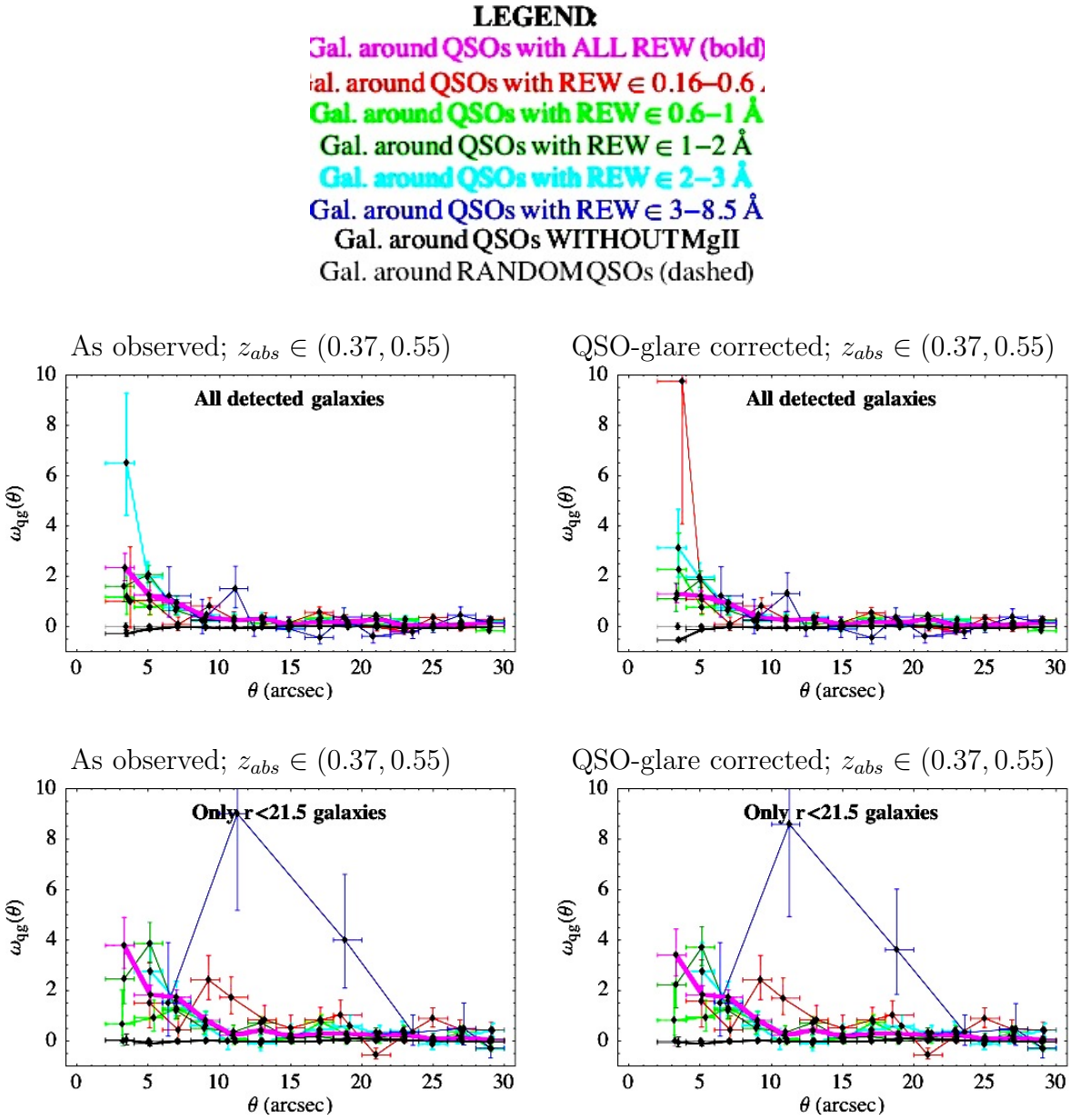

Figure 3.19: The observed and glare-corrected QSO-galaxy cross-correlation functions as a function of angular impact parameters are shown subdivided in REW intervals for the lowest z_{abs} bin. Galaxy samples with and without a magnitude threshold ($r < 21.5$) are considered, and the QSO-glare correction is applied to each of these cases.

3.1.4.3 On the MgII-Star Association

While stars may be misclassified as galaxies, a larger proportion of small and faint galaxies

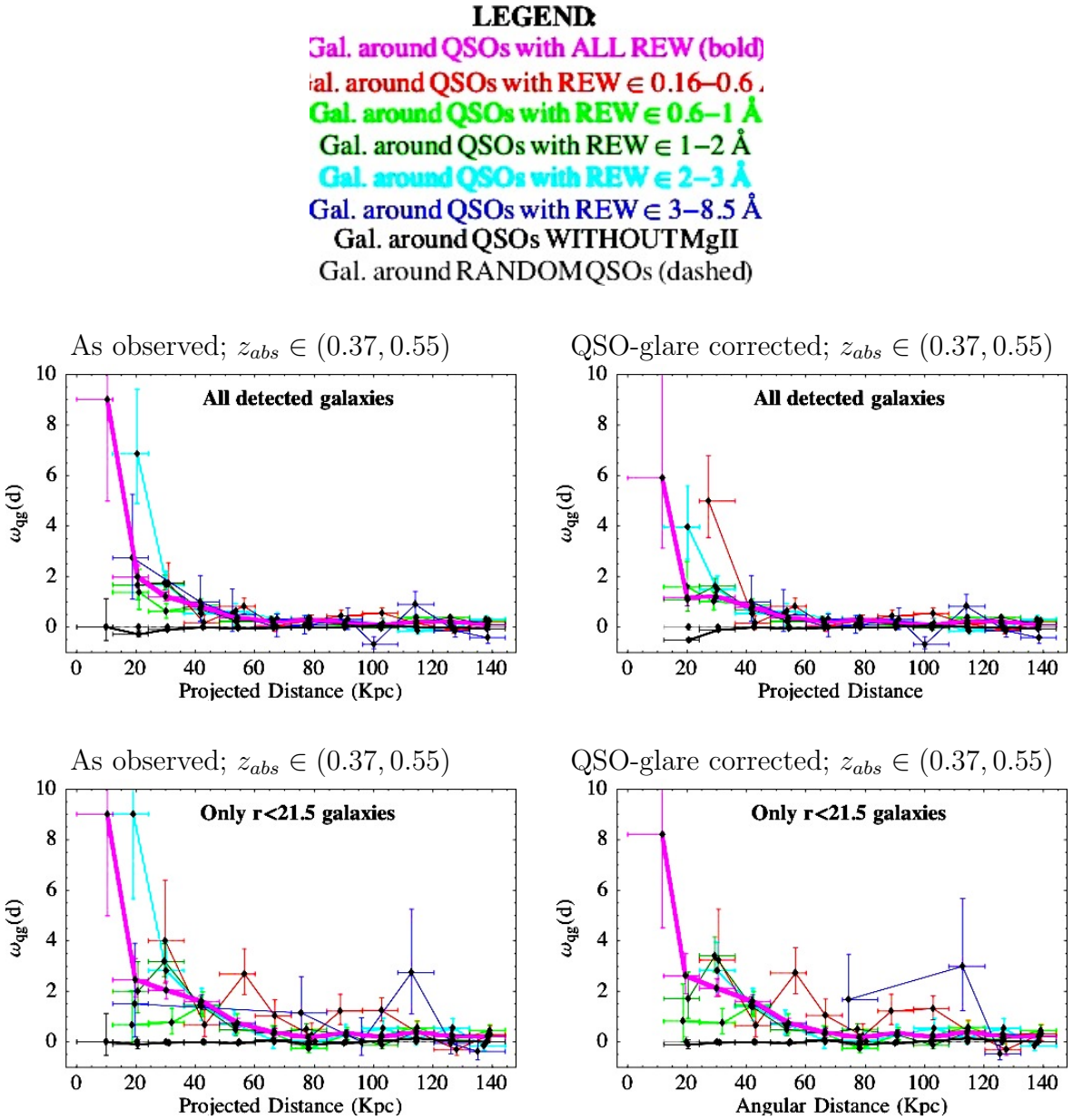

Figure 3.20: The observed and glare-corrected QSO-galaxy cross-correlation functions as a function of projected distances are shown subdivided in REW intervals for the lowest z_{abs} bin. Galaxy samples with and without a magnitude threshold ($r < 21.5$) are considered, and the QSO-glare correction is applied to each of these cases.

contaminates the stellar catalog (as mentioned in § 3.1.4.1). Such misidentifications may give rise to a weak cross-correlation signal between "stars" and MgII-absorbed QSOs, considering

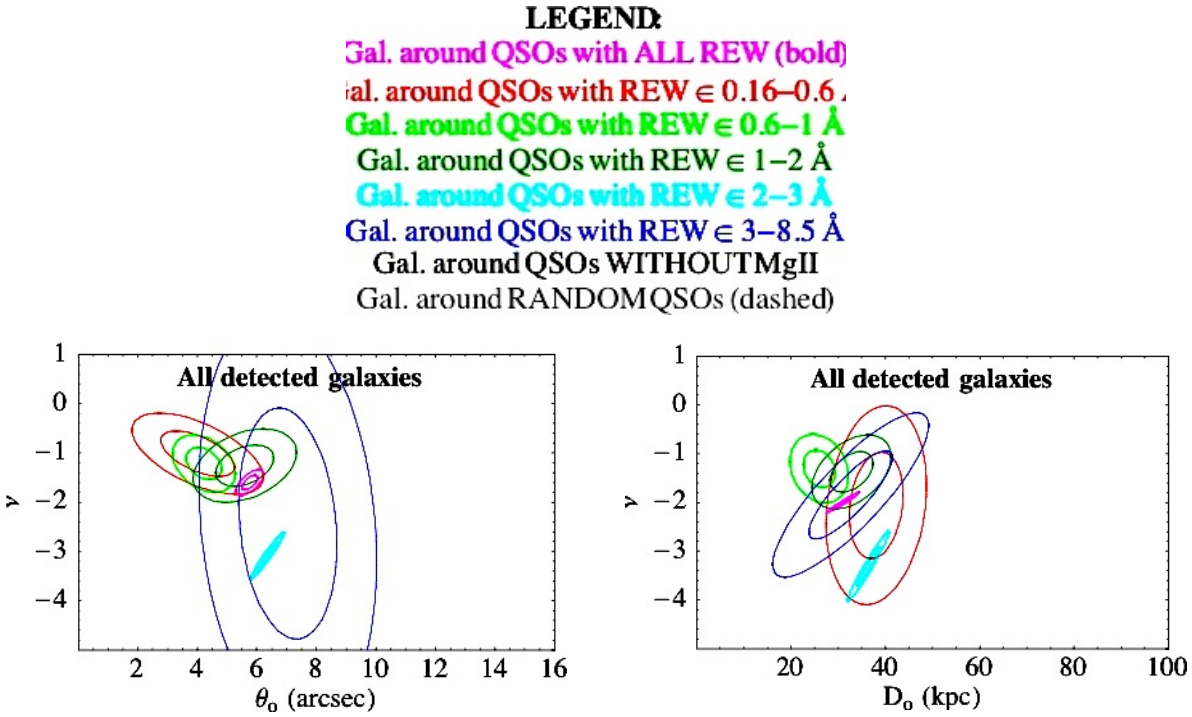

Figure 3.21: Best-fit parameters and the associated errors are depicted in terms of ellipsoidal joint confidence regions (for 68% and 95% confidence levels) for both angular and projected distance cases, as displayed on the left- and right-hand panels, respectively. Plots refer to z_{abs} ∈(0.37, 0.55), and the different REW intervals are color-coded as indicated in the legend.

Table 3.4: The best-fit parameters shown in Fig. 3.21 are listed for each REW bin together with asymptotic standard errors. The fitted data refer to z_{abs} ∈(0.37, 0.55), and no magnitude cuts are applied to galaxies.

Impact	Fitting	REW bins					
Parameter	Parameter	0.16–0.6Å	0.6–1Å	1–2Å	2–3Å	3–8.5Å	ALL REWs
Angular	ν	-1.0±0.3	-1.2±0.2	-1.3±0.3	-3.1±0.2	-2.4±1.5	-1.6±0.1
	θ_o (arcsec)	4.0±0.8	4.2±0.4	5.6±0.6	6.4±0.2	7.0±1.0	5.8±0.2
Proj. Dist.	ν	-2.1±0.7	-1.3±0.2	-1.4±0.3	-3.3±0.2	-1.8±0.6	-2.0±0.1
	D_o (kpc)	38±3	26±2	33±3	36±1	33±5	31±1

the poor imaging of SDSS galaxies in the MgII redshift detection range. As shown in Fig. 3.22, the "star"-MgII association signal does not vanish for the smallest discernible impact parameters. A more careful analysis of misclassified galaxies may provide further insight into MgII absorbers, but this approach is not pursued in this work. The contribution from multiple images of the background QSOs, gravitationally lensed by MgII-associated galaxies, is expected to be negligible with respect to the statistical errors.

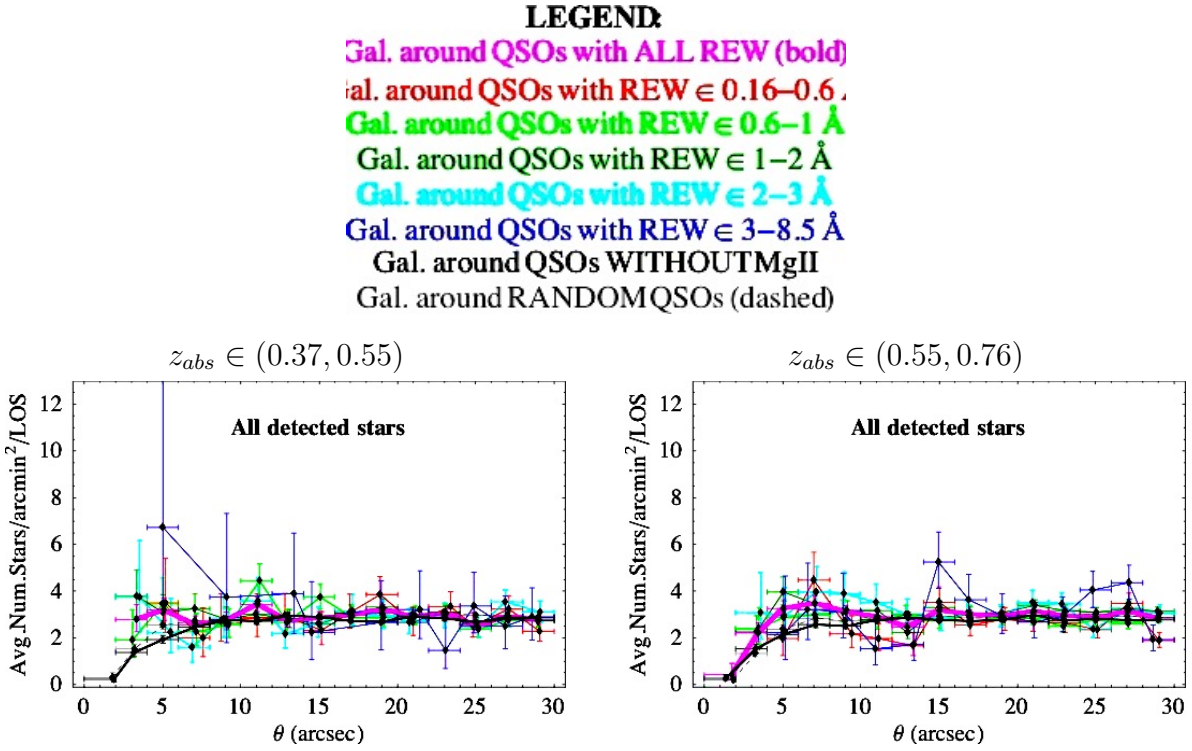

Figure 3.22: Star number density distributions, in particular those including all REWs, show a weak excess above the reference level (beyond statistical errors), which indicates that "stars" are weakly correlated with MgII absorbers within redshift intervals (0.37, 0.55) and (0.55, 0.76), presented on the left- and right-hand panel, respectively. This is believed to be a consequence of misclassification of MgII associated galaxies as stars.

3.1.4.4 Error Evaluations

Galaxies within 100 h^{-1} kpc from MgII absorbers are expected to be strongly correlated (e.g., see [Bouché et al. 2004]). However, only few galaxies per line-of-sight are detected on

average within small impact angles from QSOs (from less than one for $\theta < 10$ arcsec to about two for θ within 20–30 arcsec; see Table 3.3). Thus, galaxy counts can be considered independent, including those in the galaxy-absorber correlation region. Within the QSO sample under consideration, only 18 QSO-QSO pairs are separated by less than 30 arcsec (which is possible in regions probed by overlapping plates only), so the correlation from galaxies associated with more than a single sight-line is neglected. As a result, errors on galaxy counts within 30 arcsec of QSO sight-lines are approximated by Poisson errors (in agreement with [Landy & Szalay 1993]), and only those impact parameter bins including at least two galaxies are taken into account.

Errors bars on small number counts are computed similarly to § 2.2.3. If $\pi = n/N$ is the (unknown) probability of counting n independent galaxies in a sample of N QSO sight-lines, the observed number of galaxies $\tilde{n}$ is expected to be distributed according to the binomial distribution with average $N\pi$, and standard deviation $[N\pi(1-\pi)]^{1/2}$. Assuming the range of variability of $\tilde{n}$ around the mean is less than τ times the standard deviation, i.e. $|\tilde{n} - N\pi| < \tau[N\pi(1-\pi)]^{1/2}$, the solution for π is expressed by Eq. 2.18.

Note that errors on parameters involved in the QSO glare correction are not taken into account, so Poissonian errors underestimate the uncertainties, especially at angles less than ~ 10 arcsec from QSO sight-lines. Since glare-corrections cannot improve the accuracy of measurements and errors are based on the *observed* number counts, the plotted errors are computed by multiplying Poissonian errors by the correction factors β.

3.2 LUMINOSITY FUNCTION OF MGII-ASSOCIATED GALAXIES

The luminosity function of galaxies associated with MgII absorbers is derived by employing a background subtraction technique similar to that used in studies of galaxies within clusters [Hansen et al. 2005]. In order to extract the luminosity function, Φ_{MgII}, of only MgII-related galaxies from the distribution of all galaxies projected around QSOs with absorbers, the contribution from random background and foreground galaxies has to be removed. This is achieved by subtracting the average luminosity distribution of galaxies around random

reference QSOs (selected as described in § 3.1.2) from the average luminosity distribution of galaxies around MgII-absorbed QSOs. Although the galaxies involved in the absorption cannot be identified uniquely, this method permitted a description of the mean properties of MgII-associated galaxies.

The r-band absolute magnitudes, M_r, of galaxies are extracted from the Photoz table (uploaded in the SDSS DR5 archives), which contains photometric redshift estimates derived with a template-fitting method. Only galaxies with photometric redshifts consistent with MgII-absorbers (within the marginalized error) are considered. Since the quality of SDSS imaging (and thus photometric redshifts) is poor for most galaxies at redshifts greater than 0.37, the analysis focuses on the lowest z_{abs} interval (0.37, 0.55).

In order to probe the same physical projected area around absorbers at all redshifts, galaxies are required to lie within the maximum impact parameter $\theta_{\rm max} D_A(z_{\rm min}) \sim 150$ kpc, with $z_{\rm min} = 0.37$ and $\theta_{\rm max} = 30$ arcsec (D_A denotes the angular diameter distance). Impact parameters of galaxies around reference and absorbed QSOs are computed at the absorber redshift. This allows to keep consistency with the z_{abs} assigned to reference QSOs (see § 3.1.2), and is deemed more reliable than adopting photometric redshifts (affected by large errors). The contribution from galaxies assigned at wrong redshifts (i.e., not associated with the absorbers) is expected to be removed by the background subtraction method.

Galaxy counts per luminosity interval are normalized by the area $\pi[\theta^2_{\rm max} D^2_A(z_{\rm min}) - \theta^2_{\rm min} D^2_A(z_{\rm max})]$, where $\theta_{\rm min}$ is set to 1.4 arcsec (corresponding to the median PSF width in the r-band). However, the average number density of galaxies associated with absorbers depends on the maximum impact parameter, since the contribution from large impact angles tends to match the random reference (so that the average MgII galaxy density decreases by increasing the area surveyed around each QSO). As a consequence, the overall normalization of the derived luminosity function is affected by the choice of a selection window.

In order to assure completeness at faint luminosities, a minimum luminosity threshold is set at the largest redshift of the interval under consideration (i.e., 0.55). As shown in Fig. 3.13, the SDSS detected about 90% of the galaxies brighter than $r \sim 21.0$. The distribution of M_r for galaxies with $r \sim 21.0 \pm 0.1$ and photometric redshift $\sim 0.55 \pm 0.01$ has mean $\langle M_r \rangle \sim -22.4$ and standard deviation $\sigma_{M_r} \sim 0.3$, while $\langle M_r \rangle \sim -21.0$ and $\sigma_{M_r} \sim 0.2$ at

photometric redshift $\sim 0.37 \pm 0.01$. Consequently, number counts of galaxies at $z_{abs} \in$(0.37, 0.55) are considered complete only for bright galaxies (with $M_r < -22.4$). Such a luminosity threshold is greater than typical M_* values, so an extension of the completeness limit is pursued by computing average galaxy counts within each luminosity bin around only those QSO sight-lines where the absorber redshift is sufficiently low to permit a $\sim 90\%$ detection completeness for galaxies within such a luminosity interval[5]. Thus, the total number of sight-lines used to compute averages is a function of the luminosity bin, which depends on the associated z_{abs} and absolute magnitude threshold. The described procedure permits the extension of the absolute magnitude threshold to the corresponding value at $z_{abs} \sim 0.37$, i.e. $M_r < -21.0$.

The average distribution of absolute magnitudes of all galaxies within 150 kpc from MgII-absorbed QSOs is shown in Fig. 3.23 together with the corresponding distribution of galaxies around reference QSOs. The derived luminosity function data are weighted by statistical errors and attempted to be fitted by a Schechter function of the form [Schechter 1976]

$$\Phi(M)\, dM = 0.4 \ln(10) \Phi_* 10^{-0.4(M-M_*)(\alpha+1)} \exp\left(-10^{-0.4(M-M_*)}\right)\, dM. \qquad (3.8)$$

Unfortunately, Fig. 3.24 shows that the SDSS imaging of galaxies above redshift 0.37 limits the analysis to galaxies brighter than M_*. As a consequence, no reliable set of fitting parameters (Φ_*, M_*, and α) can be derived. This conclusion is consistent with recent results from a study of SDSS galaxies within clusters in the redshift range $0.07 < z < 0.3$ [Hansen et al. 2005], which derived M_* values from -19.95 to -20.86, depending on the cluster richness.

[5]It is found that, within the redshift interval (0.37, 0.55), a linear interpolation between the minimum and maximum redshift values reproduces reasonably well the trend of $\langle M_r \rangle$ for $r \sim 21$ galaxies. As a result, only those QSO sight-lines are accepted for which z_{abs} satisfies $M_r^{(bin)} < -7.8\, z_{abs} - 18.1$, where $M_r^{(bin)}$ denotes the faint limit of each luminosity bin. The explicit expression leading to the above relation is:

$$M_r^{(bin)} < -21.0 - \frac{22.4 - 21.0}{0.55 - 0.37}\,(z_{abs} - 0.37).$$

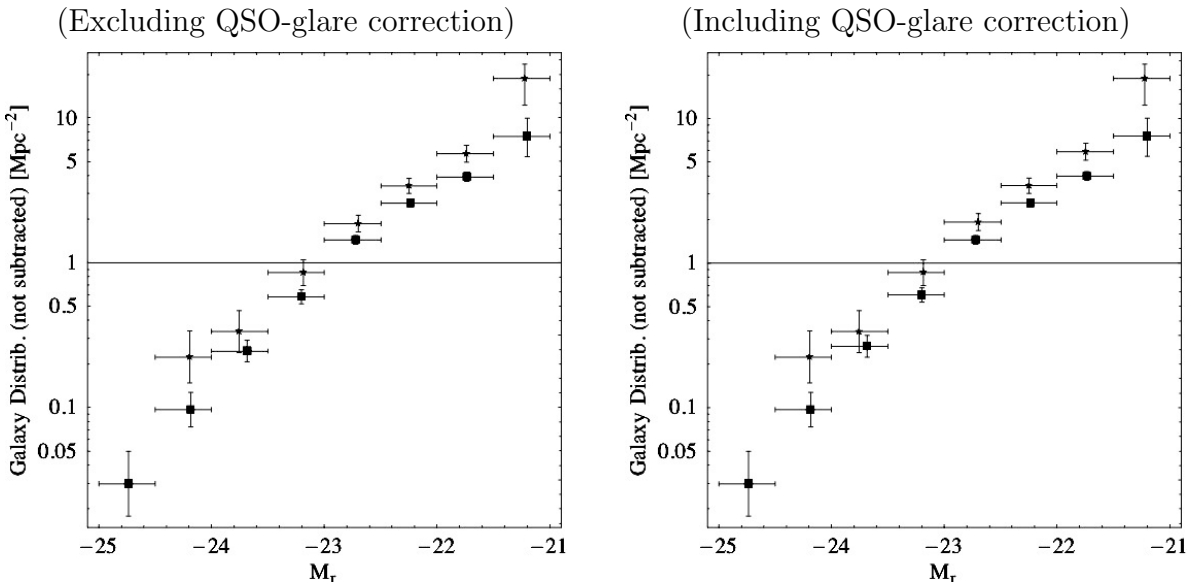

Figure 3.23: The luminosity distributions (not yet background subtracted) of galaxies within 150 kpc from reference and absorbing QSOs (with absorbers of all REWs and with $z_{abs} \in (0.37,\ 0.55)$) are plotted with boxed and starred symbols, respectively. The left-hand panel does not include QSO-glare corrections, which are applied to the plot shown on the right-hand side.

3.3 PHOTOMETRIC PROPERTIES OF MGII-ASSOCIATED GALAXIES

Despite the fact that most of the SDSS galaxies in the MgII redshift range of detection are faint and thus have large photometric errors, further insight into galaxies associated with MgII absorbers is attempted by comparing their average integrated fluxes and average colors with the same quantities for galaxies around reference QSOs, within a projected distance of 100 kpc (in order to compare easily results with those from a recent study employing the same data set [Zibetti et al. 2007]). Integrated reference galaxy fluxes are subtracted from those corresponding to galaxies around absorbing QSOs, so that the contribution of galaxies not associated with the absorption is removed. In order to minimize contamination effects, only the lowest z_{abs} interval (0.37, 0.55) is considered. In order to derive intrinsic colors and fluxes of absorbing galaxies, all galaxy magnitudes are corrected for Galactic extinction.

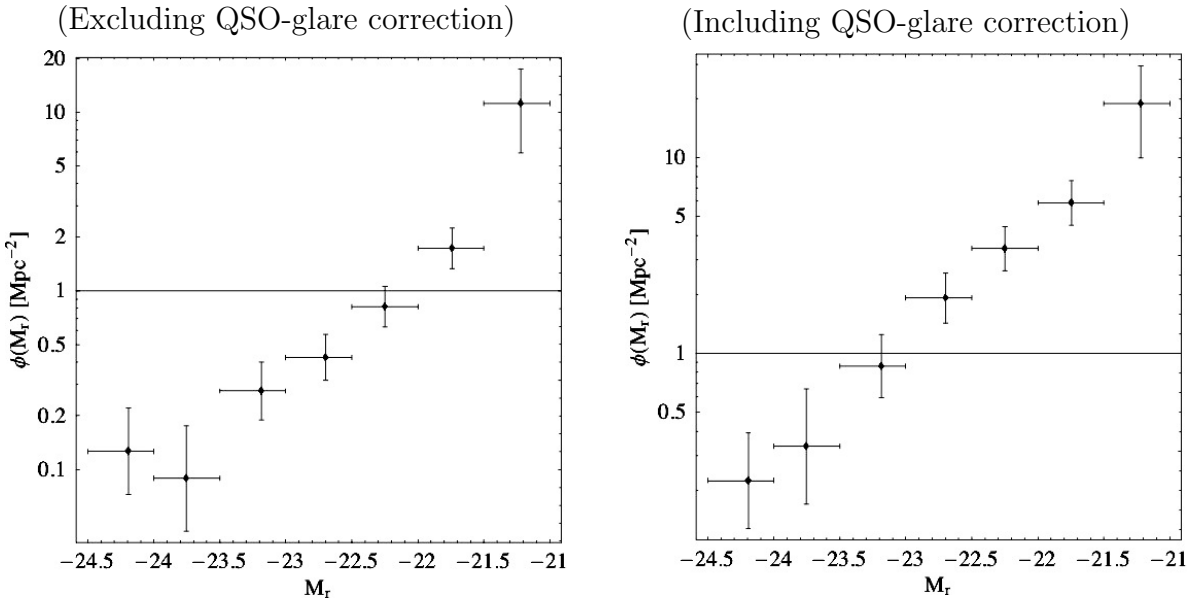

Figure 3.24: The luminosity function of galaxies associated with absorbers (obtained by subtracting the background contribution) of all REWs and with $z_{abs} \in (0.37, 0.55)$ is plotted excluding and including the QSO-glare correction, as shown on the left- and right-hand side, respectively. Galaxy counts (within a given area and luminosity interval) sample only galaxies brighter than M_*, so luminosity function parameters cannot be derived.

Note that such a correction was excluded in the study of galaxy number counts (§ 3.1), because the QSO-glare effect depended on the observed brightness levels.

3.3.1 Average Integrated Fluxes

The flux from galaxies is integrated within a 100-kpc projected radius around QSO sight-lines, and then averaged over all MgII-absorbing sight-lines for each REW sample. Galaxy positions are determined from their centroids, and the fractions of galaxies included and excluded by circular boundaries around QSOs are assumed to compensate each other[6].

Denoting by F_i^{abs} and F_i^{ref} the integrated fluxes around the i-th sight-line of MgII-

[6]Actually, the integrated flux may include slightly more flux from galaxies partially outside the boundary than lose from galaxy only partly within the boundary. A careful evaluation of this difference should take into account the sizes of galaxies (and their distribution) with respect to the region enclosed by the boundary.

absorbing and corresponding reference QSOs, respectively, and recalling that 5 reference QSOs are extracted for each line-of-sight with absorbers, the individual fluxes f_j from the surrounding galaxies (identified by the index j) are integrated as follows:

$$F_i^{abs} = \sum_j f_{i,j}^{abs} \tag{3.9}$$

$$F_i^{ref} = \frac{1}{5}\sum_{k=1}^{5}\sum_j f_{i,j,k}^{ref}, \tag{3.10}$$

where the reference galaxy flux is averaged over multiple sight-lines. The net flux F_i^{net} from the galaxies associated with MgII only is found from

$$F_i^{net} = F_i^{abs} - F_i^{ref}. \tag{3.11}$$

Average integrated fluxes are obtained by applying the operator $\langle ... \rangle = (1/N_{QSO}^{abs}) \sum_{i=1}^{N_{QSO}^{abs}} ...$ to the quantities described in Eq. 3.9–3.10. In order to evaluate the error on $\langle F^{net} \rangle$, the following covariance matrix is computed:

$$\mathrm{cov}(F^{abs}, F^{ref}) = \frac{1}{N_{QSO}^{abs}(N_{QSO}^{abs}-1)} \sum_{i=1}^{N_{QSO}^{abs}} (F_i^{abs} - \langle F^{abs} \rangle) \cdot (F_i^{ref} - \langle F^{ref} \rangle), \tag{3.12}$$

so that the variance $\sigma^2_{\langle F^{net} \rangle}$ of the mean net integrated flux is found as follows:

$$\sigma^2_{\langle F^{net} \rangle} = \sigma^2_{\langle F^{abs} \rangle} + \sigma^2_{\langle F^{ref} \rangle} - 2\sigma_{\langle F^{abs} \rangle \langle F^{ref} \rangle}. \tag{3.13}$$

The magnitudes m of average integrated fluxes are computed adopting the SDSS definition:

$$m = -\frac{2.5}{\ln(10)} \left[\mathrm{asinh}\left(\frac{\langle F^{net} \rangle}{2bf_o} \right) + \ln(b) \right], \tag{3.14}$$

with f_o denoting the zero-point count rate, and b being a softening parameter depending on the photometric band (up-to-date values are listed on the SDSS website).

Plots of 5-band magnitudes of average fluxes integrated within 100 kpc are presented in Fig. 3.25 and Fig. 3.26 for galaxies without and with a magnitude threshold ($r < 21.5$), respectively, and within different REW intervals. Despite large error bars, some trend for the average flux of MgII-associated galaxies with REW emerges (though less than 2-σ from the reference values). In particular, weak absorption systems seem to be associated with

more luminous galaxies than those related to strong absorbers. This conclusion is further supported by recalling that strong systems are found more concentrated near the QSO sight-line with respect to weak absorbers (see § 3.1.4.2), so the 100 kpc boundary is more likely to omit more weakly-absorbing galaxies than strongly-absorbing ones. The average flux integrated within 100 kpc from QSO sight-lines with strong absorbers is fainter than that from galaxies around random QSOs, despite the excess of galaxy counts around absorbers found in § 3.1.4. Such an effect is possible if strong absorbers are due to less luminous galaxies than average. As for the sample including all REW, the strong and weak REW trends tend to compensate each other, and only a marginal deficiency and excess in the u- and z-bands, respectively, is observed. The significance of plots with only $r < 21.5$ galaxies is slightly smaller because of fewer galaxies, but results are qualitatively identical. Further interpretation is presented in § 3.3.3 together with results on average colors.

3.3.2 Average Colors of Integrated Fluxes

The magnitude m_i of the integrated flux of galaxies around the i-th sight-line with absorbers is computed as

$$m_i = -\frac{2.5}{\ln(10)}\left[\operatorname{asinh}\left(\frac{F_i^{net}}{2bf_o}\right) + \ln(b)\right]. \tag{3.15}$$

Identifying various filters by greek indices, the covariance matrix of the average colors $\langle m_\alpha - m_\beta\rangle$ and $\langle m_\gamma - m_\delta\rangle$ is computed as follows:

$$\operatorname{cov}(m_\alpha - m_\beta, m_\gamma - m_\delta) = \frac{1}{N_{QSO}^{abs}(N_{QSO}^{abs}-1)}\times$$

$$\times \sum_{i=1}^{N_{QSO}^{abs}} \left[(m_{\alpha,i} - m_{\beta,i}) - \langle m_\alpha - m_\beta\rangle\right]\cdot\left[(m_{\gamma,i} - m_{\delta,i}) - \langle m_\gamma - m_\delta\rangle\right], \tag{3.16}$$

where N_{QSO}^{abs} indicates the number of absorbing QSOs in the sample under consideration. The same computation is repeated for average colors of galaxies around reference QSOs, so that results can be compared.

Assuming errors are normally distributed in color-color space, elliptical joint confidence regions of the average colors of integrated fluxes for MgII-associated and reference galaxies

(No magnitude threshold is applied to galaxies)

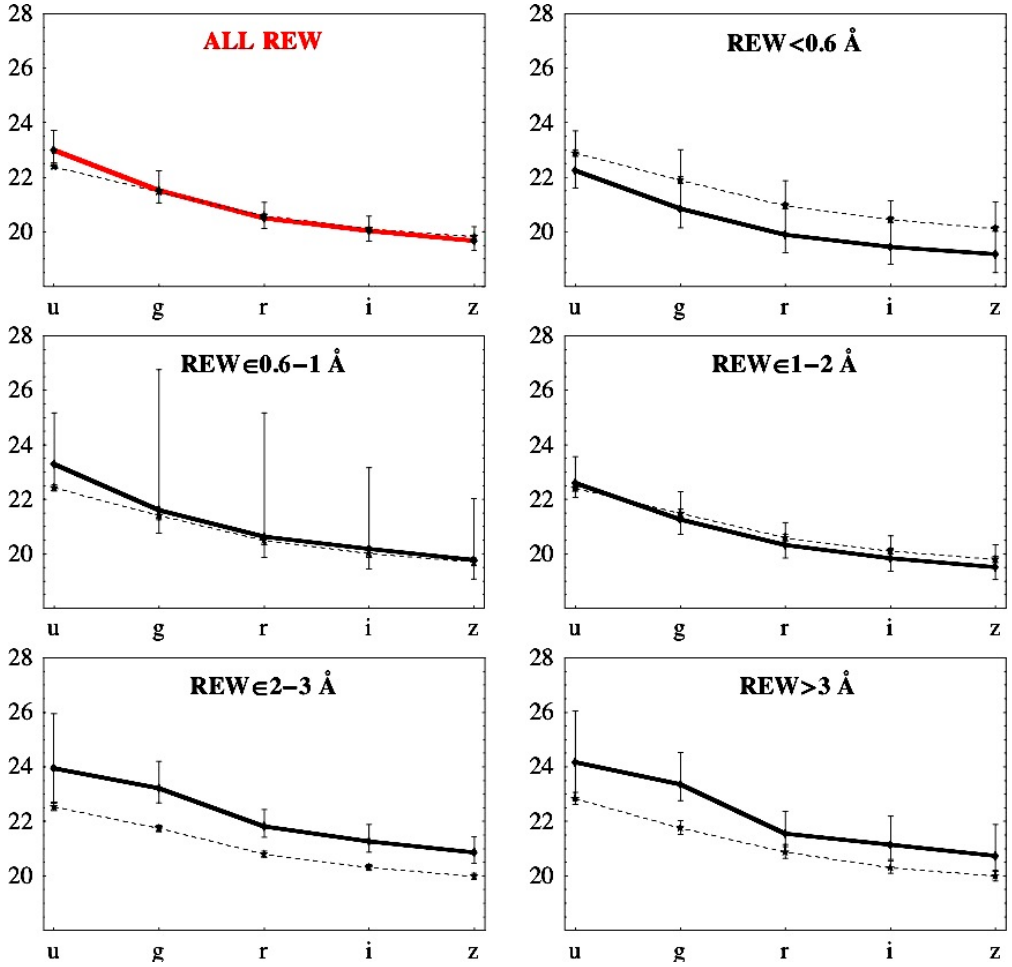

Figure 3.25: The magnitudes in 5-bands of average galaxy fluxes integrated within 100 kpc are shown for absorbers with redshift $z_{abs} \in (0.37, 0.55)$ and REWs in the ranges 0.16–8.5 Å, <0.6 Å, 0.6–1 Å, 1–2 Å, 2–3 Å, and >3 Å, presented in the above panels from top-left to bottom-right. Points related to absorbing galaxies are connected by solid lines (red for all REW, and black for separate REW bins), while dashed lines refer to average fluxes of galaxies integrated around random reference QSOs (corresponding to specific REW ranges).

were evaluated as a function of REW for various projections of the color space, as shown in Fig. 3.27–3.30. Only galaxies within 100 kpc from QSO sight-lines are included, and galaxy magnitudes are corrected for Galactic extinction. Smaller dashed ellipses indicate

(Only galaxies with $r < 21.5$)

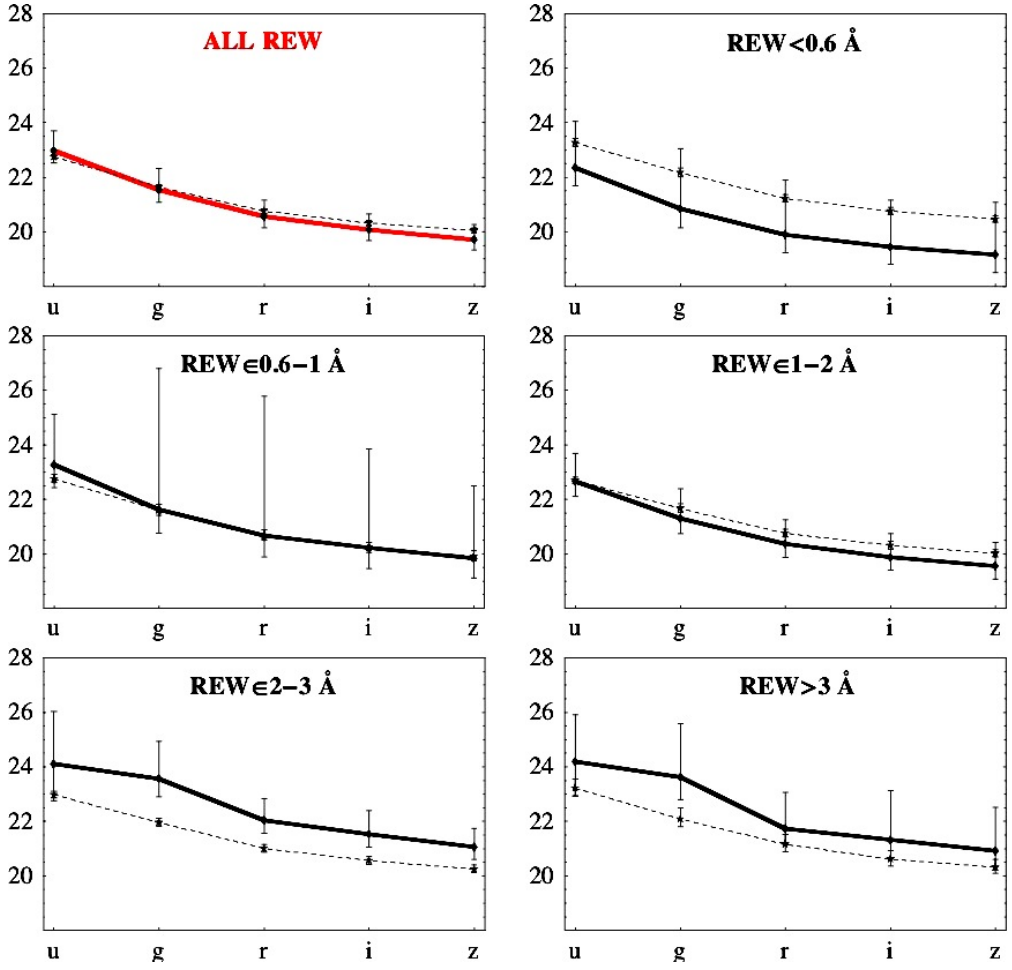

Figure 3.26: Same as Fig. 3.25, but for galaxies brighter than $r = 21.5$ only.

confidence regions for galaxies around the corresponding reference QSOs. Two different reference samples are employed: random QSOs (in Fig. 3.27–3.28) and non-absorbing QSOs (in Fig. 3.29–3.30). Each of these cases is presented with and without imposing a galaxy magnitude threshold of $r < 21.5$. For reference purposes, all plots include labels identifying galaxy types at redshift 0.5 (from [Fukugita et al. 1995]).

3.3.3 Discussion

Errors on average colors of integrated fluxes in different REW intervals are too large to establish a relation between REW and colors (or galaxy types) as shown in Fig. 3.27–3.30. However, comparing average colors of MgII-associated galaxies with all REWs versus reference galaxies in all Figures, absorption-related galaxies are found with a bimodal color distribution: bluer in the $u-g$ color, and redder in the $i-z$ color. The effect is stronger when no apparent magnitude cut is applied to the galaxy sample, as expected as a consequence of the additional contamination introduced by a magnitude threshold (as discussed in § 3.1.4.1).

It has been argued [Baldry et al. 2004] that the $u-X$ color (where X indicates any of the other bands) is very sensitive to star formation history of galaxies. A blueward offset of ~ 1 magnitude (slightly more [less] when all [only $r < 21.5$] galaxies are considered) in the $u-g$ color with respect to random or non-absorbing reference galaxies is consistent with high star-formation rates, suggesting spiral galaxies are associated with MgII absorption lines. On the other hand, a redward offset of the same order of magnitude in the $i-z$ color would indicate that evolved reddish elliptical galaxies are likely to be related to MgII absorbers.

Such a bimodal contribution to MgII absorption was also found in a recent analysis of the optical properties of MgII absorbers by stacking SDSS images [Zibetti et al. 2007]. Such a method collected higher signal-to-noise information on the light from absorbers, and the contribution from different absorption strengths could be separated and interpreted in terms of galaxy evolution. In particular, stronger systems were found to be consistent with bluer (star-forming) galaxies, while weaker ones were associated with redder and older galaxies. Such a scenario is consistent with the results from colors reached for the case of all REWs (see § 3.3.2), and it agrees with the conclusions from average integrated fluxes computed as a function of REW (weak absorbers are associated with more luminous galaxies than strong systems, as found in § 3.3.1). Also, results from the QSO-galaxy cross-correlation function (indicating weak MgII absorbers are at larger impact parameters than strong systems – see § 3.1.4.2) support the above interpretation. Recalling the description of galactic outflows in § 1.2.2.2 (and references therein), supernova explosions in young star-forming regions form

super-bubbles, which expand and lead to superwinds on galactic scales. As the galaxy ages, the outflowing gas reaches farther distances from the galaxy. This is consistent with MgII systems associated with older galaxies being detected mostly in the outskirts of galaxies.

However, what is actually measured are galaxies *associated* with MgII, which include galaxies clustered around the absorbing one. An alternative scenario may involve MgII absorbers as being primarily due to spiral galaxies, while their neighborhood may determine the strength of the absorption and apparent color of absorbing galaxies. For example, weak absorbers may arise from spiral galaxies embedded in redder, more luminous, and more extended environments like galaxy clusters, while strong absorbers may occur from more isolated, bluer, less luminous, and smaller objects like field galaxies. The exact mix of absorbing galaxy properties and environmental effects will need further investigation.

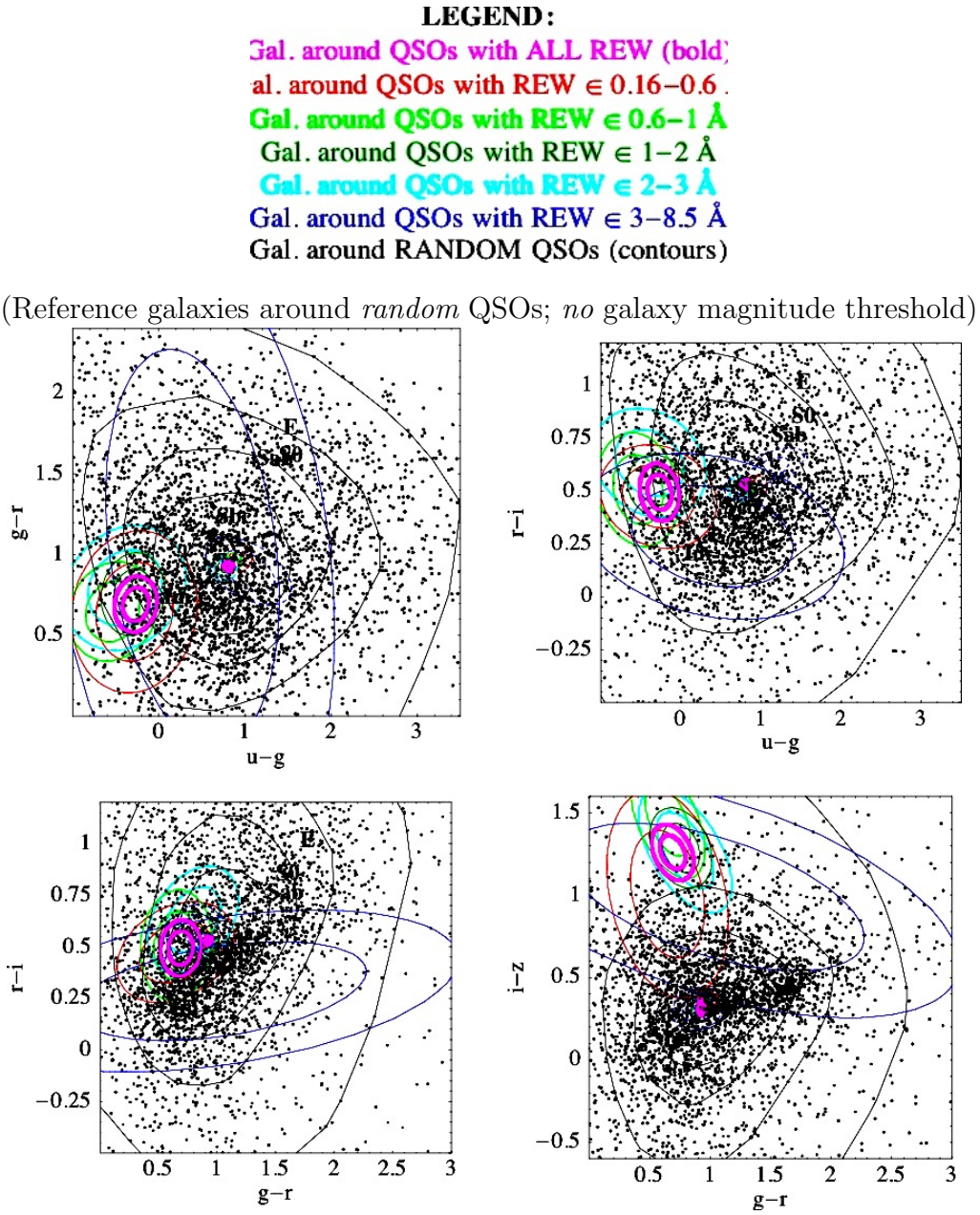

Figure 3.27: Elliptical confidence regions (with 68% and 95% confidence levels) of the average colors of integrated fluxes for MgII-associated galaxies are shown as a function of REW (color-coded as indicated in the legend). Galaxies of all magnitudes but within 100 kpc of the absorbing sight-line are included; all magnitudes are corrected for Galactic extinction. Smaller dashed ellipses indicate the corresponding regions for galaxies around random reference QSOs (with the same REW color legend). Labels identify galaxy types at redshift 0.5 (from [Fukugita et al. 1995]) and are included for reference purpose only. The background black points depict the distribution of colors of galaxies in the random reference sample, with contour lines enclosing from 10% to 90% of the points in steps of 20%.

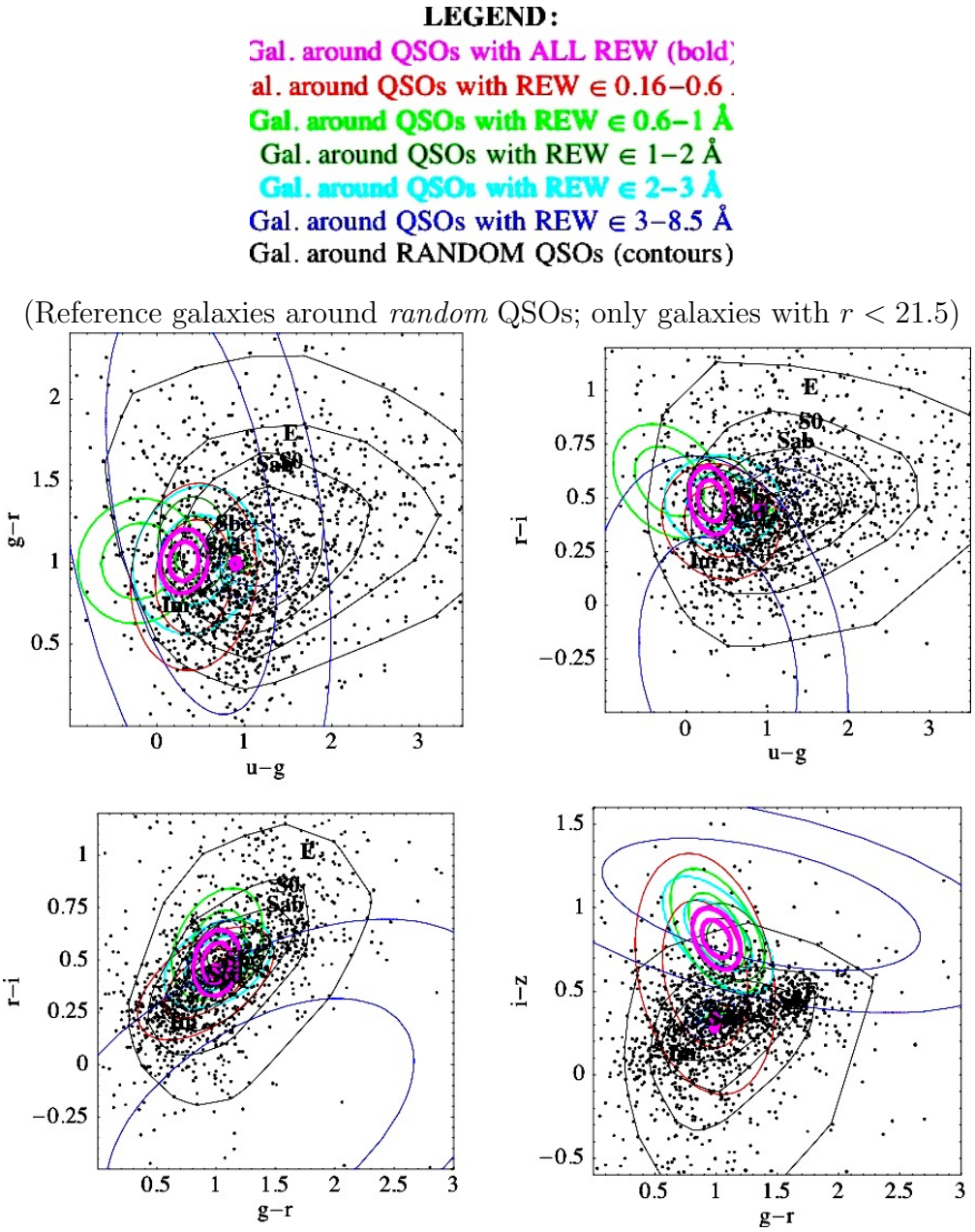

Figure 3.28: Elliptical confidence regions (with 68% and 95% confidence levels) of the average colors of integrated fluxes for MgII-associated galaxies are shown as a function of REW (color-coded as indicated in the legend). Only galaxies with r-band magnitudes brighter than 21.5 and within 100 kpc of the absorbing sight-line are included; all magnitudes are corrected for Galactic extinction. Smaller dashed ellipses indicate the corresponding regions for galaxies around random reference QSOs (with the same REW color legend). Labels identify galaxy types at redshift 0.5 (from [Fukugita et al. 1995]) and are included for reference purpose only. The background black points depict the distribution of colors of galaxies in the random reference sample, with contour lines enclosing from 10% to 90% of the points in steps of 20%.

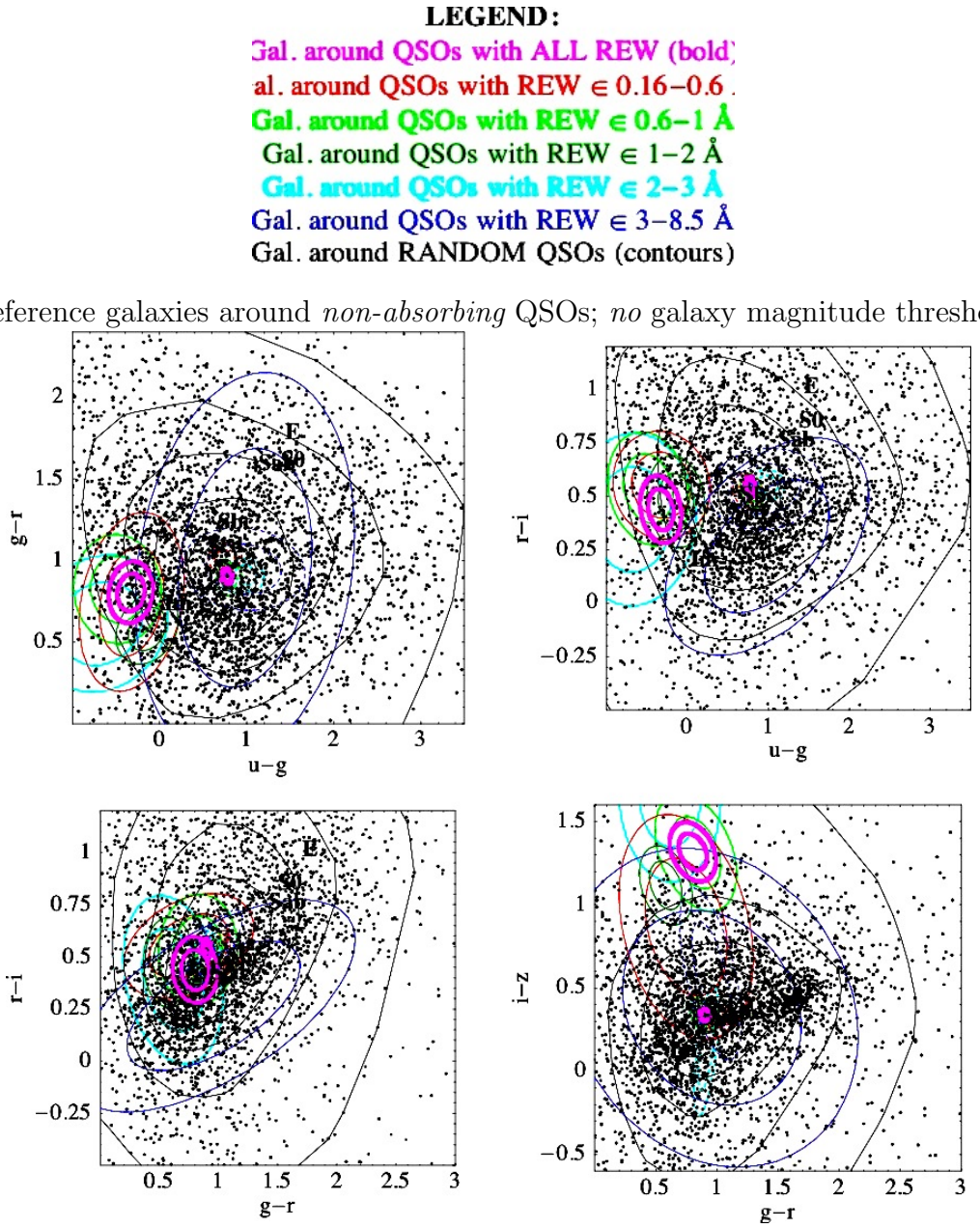

Figure 3.29: Elliptical confidence regions (with 68% and 95% confidence levels) of the average colors of integrated fluxes for MgII-associated galaxies are shown as a function of REW (color-coded as indicated in the legend). Galaxies of all magnitudes but within 100 kpc of the absorbing sight-line are included; all magnitudes are corrected for Galactic extinction. Smaller dashed ellipses indicate the corresponding regions for galaxies around non-absorbing reference QSOs (with the same REW color legend). Labels identify galaxy types at redshift 0.5 (from [Fukugita et al. 1995]) and are included for reference purpose only. The background black points depict the distribution of colors of galaxies in the random reference sample, with contour lines enclosing from 10% to 90% of the points in steps of 20%.

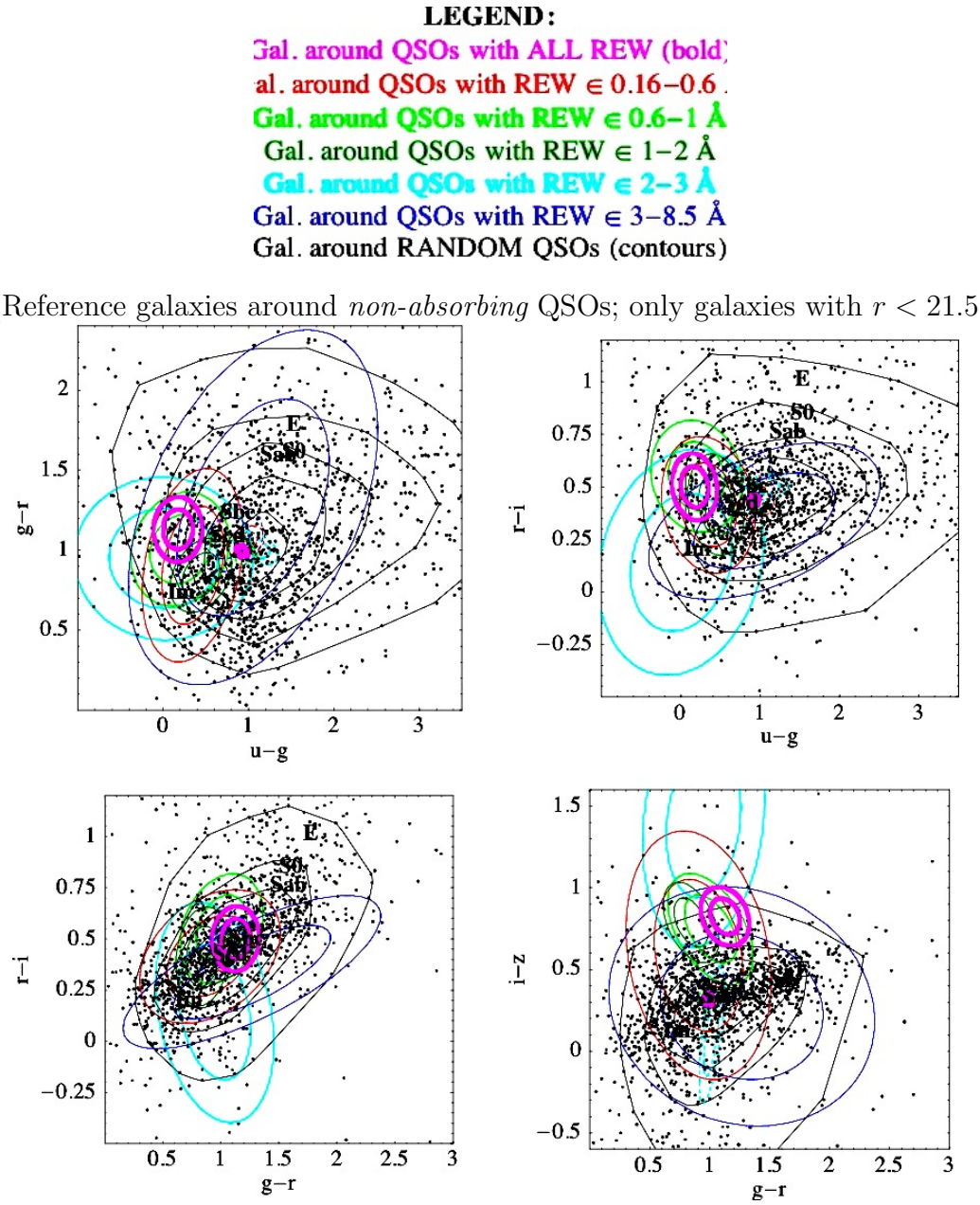

Figure 3.30: Elliptical confidence regions (with 68% and 95% confidence levels) of the average colors of integrated fluxes for MgII-associated galaxies are shown as a function of REW (color-coded as indicated in the legend). Only galaxies with r-band magnitudes brighter than 21.5 and within 100 kpc of the absorbing sight-line are included; all magnitudes are corrected for Galactic extinction. Smaller dashed ellipses indicate the corresponding regions for galaxies around non-absorbing reference QSOs (with the same REW color legend). Labels identify galaxy types at redshift 0.5 (from [Fukugita et al. 1995]) and are included for reference purpose only. The background black points depict the distribution of colors of galaxies in the random reference sample, with contour lines enclosing from 10% to 90% of the points in steps of 20%.

4.0 MODELING MGII ABSORBERS AND THEIR EVOLUTION IN REDSHIFT

Since the statistical luminosity-dependent model for the cross-section of MgII-absorbing gas in galaxies was introduced [Steidel 1995, Steidel 1993, Lanzetta 1993] (as described in Chapter 1 and § 4.1.2 in more detail), the number of strong MgII absorbers detected increased by more than two orders of magnitude because of the SDSS. The improved statistics permits an unprecedented accuracy in measurements of absorption incidence (see Chapter 2) and the MgII absorber association with galaxies as a function of REW as well as impact parameter (see Chapter 3).

The shallow SDSS galaxy imaging limited the study of MgII-absorbing galaxies to the lowest redshift interval 0.37–0.55, removing from consideration the greatest part of the sample (about 95% if multiple detections per sight-line are included). In order to fully exploit the wealth of information contained in the MgII catalog, the deepest galaxy imaging to date (the Hubble Ultra Deep Field, HUDF) is considered in combination with the measured absorption incidence over the whole MgII redshift range of detection. Such a comparison is described in § 4.2 but it can only be of statistical nature, because the HUDF galaxies associated with absorbers cannot be directly studied. However, taking advantage even indirectly of the full statistical properties of the data set allows investigation of the average evolution with redshift of galaxies' gaseous cross-sections.

Since results in Chapter 3 suggest a possible REW–impact parameter relation, a statistical model for absorbers is developed analytically (in § 4.3) to account for the measured MgII REW distribution in terms of impact parameter, luminosity, and redshift of absorbing galaxies. Possible scenarios are illustrated and compared with results obtained in Chapter 3. New observational tests to break parameter degeneracies are discussed.

4.1 A SIMPLE STATISTICAL MODEL FOR MGII ABSORBING GALAXIES

4.1.1 Notation and Assumptions

For clarity purposes, this section defines notation and assumptions for the basic formulas adopted in the rest of this Chapter, including luminosity function parameters and their evolution, as well as some cosmological distance relations.

4.1.1.1 Galaxy Luminosity Function

The luminosity function of galaxies at a given redshift is approximated by a Schechter function [Schechter 1976] as follows

$$\Phi(L|z)\,dL = \frac{\Phi_*(z)}{L_*(z)}\left(\frac{L}{L_*(z)}\right)^{\alpha}\exp\left(-\frac{L}{L_*(z)}\right)\,dL, \tag{4.1}$$

assuming a constant faint-end slope α. The evolution of the characteristic luminosity $L_*(z)$ at the "knee" of the distribution is parametrized as

$$L_*(z) = L_{*,0}\,(1+z)^q, \tag{4.2}$$

while the redshift dependence of the proper number density of galaxies $\Phi_*(z)$ includes a factor $(1+z)^3$ from cosmological expansion and an additional contribution from intrinsic evolution, indicated by the parameter p:

$$\Phi_*(z) = \Phi_{*,0}\,(1+z)^{3+p}. \tag{4.3}$$

In terms of absolute magnitudes, Eq. 4.1 can be written as

$$\Phi(M|z)\,dM = 0.4\ln(10)\,\Phi_*(z)\,10^{-0.4(M-M_*(z))(\alpha+1)}\exp\left(-10^{-0.4(M-M_*(z))}\right)\,dM, \tag{4.4}$$

with

$$M_*(z) = M_{*,o} - 2.5\,q\,\log(1+z). \tag{4.5}$$

Computations are performed in proper space because impact parameters and cross-sections of gaseous halos are not affected by cosmological expansion.

4.1.1.2 Cosmological Distances

In today's standard cosmological model, a flat ΛCDM Universe (with $\Omega_M = 0.3$ and $\Omega_\Lambda = 0.7$) expands at the rate $H(z) = H_o\, E(z)$, where $H_o \sim 70$ km s^{-1} Mpc^{-1} denotes the Hubble constant and its evolution is

$$E(z) = \sqrt{\Omega_M (1+z)^3 + \Omega_\Lambda}. \tag{4.6}$$

In flat cosmological models, the line-of-sight comoving distance to redshift z and the comoving transverse distance $D_c(z)$ at redshift z are given by the same expression

$$D_c(z) = \frac{c}{H_o} \int_0^z \frac{dz'}{E(z')}. \tag{4.7}$$

The angular diameter distance D_A (a proper length) is related to the transverse comoving distance by $D_A = D_c/(1+z)$ and the proper distance element dl along the line-of-sight is

$$dl = \frac{c}{H_o} \frac{dz}{(1+z)\, E(z)}. \tag{4.8}$$

4.1.2 The Model

Assuming that a MgII absorber is detected when the impact parameter of the QSO line-of-sight with respect to the center of the absorbing galaxy (of luminosity L and at given redshift z) is less than a maximum value $R(L|z)$, the gaseous cross-section of the galaxy $s(L|z)$ can be modeled as a Holmberg-like relation [Holmberg 1975]:

$$s(L|z) = K \tilde{\epsilon}(L|z)\, \kappa\, \pi R^2(L|z), \quad \text{with} \quad R(L|z) = R_*(z) \left(\frac{L}{L_*(z)} \right)^\beta, \tag{4.9}$$

where β denotes the power for the luminosity scaling, R_* indicates the projected radial extent of the absorbing gas associated with a L_* galaxy, K specifies the geometrical model ($K = 1$ for spherical geometries and $K = 0.5$ for disk-like geometries), and $\tilde{\epsilon}(L|z)$ represents the fraction of galaxies of luminosity L at redshift z participating in the absorption with covering factor κ.

If MgII absorbers are associated with galaxies, the number of absorbers dn intercepted by a random line-of-sight due to galaxies of luminosity and redshift within the intervals $(L, L+dL)$ and $(z, z+dz)$, respectively, is:

$$dn = \Phi(L|z)\, s(L|z)\, dL\, dl = \Phi(L|z)\, s(L|z)\, \frac{c}{H_o} \frac{dL\, dz}{(1+z)\sqrt{\Omega_M (1+z)^3 + \Omega_\Lambda}}. \tag{4.10}$$

Thus, dn/dz is found by integrating Eq. 4.10 over luminosity:

$$\frac{dn}{dz} = K \kappa\, \pi\, \frac{dl}{dz} \int_0^\infty \tilde{\epsilon}(L|z)\, \Phi(L|z)\, R^2(L|z)\, dL. \tag{4.11}$$

Assuming for simplicity that $\tilde{\epsilon}(L|z) = \epsilon H[L - L_{\rm min}(z)] H[L_{\rm max}(z) - L]$, where $H(x)$ denotes the Heaviside step function and $(L_{\rm min}, L_{\rm max})$ defines the luminosity range (though not necessarily bounded) of the fraction ϵ of galaxies participating in the absorption, e.g., for $W > W_{\rm min}$, Eq. 4.11 becomes:

$$\left.\frac{dn}{dz}\right|_{W>W_{\rm min}} = K \kappa \epsilon\, \pi\, \Phi_*(z) R_*^2(z)\, \Xi(z)\, \frac{dl}{dz} \tag{4.12}$$

with

$$\Xi(z) \equiv \Gamma\left(1 + \alpha + 2\beta, \frac{L_{\rm min}(z)}{L_*(z)}\right) - \Gamma\left(1 + \alpha + 2\beta, \frac{L_{\rm max}(z)}{L_*(z)}\right), \tag{4.13}$$

where $\Gamma(a,b) = \int_b^\infty t^{a-1} e^{-t} dt$ describes the incomplete gamma function with $t = L/L_*$. Studies of absorbing galaxies in the B-band have found $\beta \sim 0.2$, while typical K-band values for $L_{\rm min}$ have been taken to be $\sim 0.05 L_*$ [Steidel et al. 1994]. If the absorption dn/dz and the galaxy luminosity function are measured, Eq. 4.12 may be rearranged to determine $R_*(z)$ as a function of redshift:

$$R_*(z) = \left(\frac{1}{K \kappa \epsilon \pi\, \Phi_*(z)\, \Xi(z)\, dl/dz} \left.\frac{dn}{dz}\right|_{W>W_{\rm min}} \right)^{1/2}, \tag{4.14}$$

which may be fitted by the following expression (including normalization and evolution parameters $R_{*,o}$ and γ, respectively):

$$R_*(z) = R_{*,0} (1+z)^\gamma. \tag{4.15}$$

4.2 THE HUBBLE ULTRA-DEEP FIELD

The Hubble Ultra-Deep Field (HUDF) was employed as a tool to complement the shallow SDSS imaging and investigate high-redshift galaxies in the context of absorption cross-section modeling.

The HUDF was obtained by the Hubble Space Telescope ACS and NICMOS between 2003 and 2004, and it covered 12.80 arcmin^2 centered at RA=03° 32' 39.0", Dec=−27° 47' 29.1" (J2000). The multi-wavelength deep images included four wide-band filters in the optical at 3700–10,000 Å (B, V, i, z) with 0.05 arcsec pixel^{-1} resolution and two near-infrared bands (J and H) extending the wavelength coverage to ∼18,000 Å with 0.2 arcsec pixel^{-1} resolution.

Combining and drizzling images [Fruchter & Hook 2002] lead to even finer resolutions of 0.03 arcsec and 0.09 arcsec pixel^{-1} for the optical and near-infrared images, respectively. The combined optical image released to the public included over 10,000 sources in the i-band (which had the longest total exposure time of 347,110 s), leading to the deepest and most detailed portrait of the Universe to date.

4.2.1 HUDF Galaxy Luminosity Function

The luminosity function derived from HUDF galaxies is expected to probe galaxy evolution and the contribution from faint galaxies at high redshifts. However, fewer than 100 spectroscopic redshifts have been measured for galaxies within the HUDF footprint to date. While more of them will be obtained in the future, non-spectroscopic techniques to estimate redshifts are necessary because of the large number of objects as well as the low apparent luminosity of many of them, which would make spectroscopic analyses practically impossible even with the largest telescopes available.

The high-quality multi-band photometry of the HUDF is expected to permit the determination of robust photometric redshifts. Methods to estimate galaxy redshifts from multicolor data are usually of empirical nature. Some adopt a training set of objects with known spectroscopic redshifts and multiband photometry, and then derive an empirical relation between them (which, however, is reliable only for objects similar to those in the training set). Other

methods are based on templates created by synthetic galaxy spectral energy distributions, and the galaxy type and redshift are found by minimizing the difference with the observed colors.

A combination of the techniques described above involves a training set of galaxies to build an optimal set of spectral templates, which are then matched to the observed colors. It has been shown [Budavary & Szalay 2000] that this method provides a significant decrease in the dispersion of the photometric redshift estimates with respect to the spectroscopic ones.

In this section, the photometric redshifts for HUDF galaxies are extracted from a recent study [Coe et al. 2006], which provides results accurate to within $0.04(1+z_{spec})$ out to $z < 6$ within the central 11.97 arcmin^2 (assuring at least half of the average depth of the whole image).

The absolute luminosities [Cameron & Driver 2007] employed in this Chapter correspond to a subsample of 2532 sources with $i < 28$ and minimum surface brightness of $\sim$27.4 mag arcsec^{-2}. The magnitude threshold is 1.5 mag brighter than the completeness limit as implied by the turnover of galaxy number counts. K-corrections from the observed i-band to rest-frame B-band are computed using the photometric redshift catalog [Coe et al. 2006] and minimizing the χ^2 of all observed vs. artificial magnitudes from synthetic spectral templates [Cameron & Driver 2007, Poggianti 1997].

The distribution of B-band absolute magnitudes, M_B, in redshift is shown in Fig. 4.1 together with the incidence of galaxies as a function of redshift.

The luminosity function parametrized in § 4.1.1.1 is fitted for a complete subset of galaxies brighter than $M_B = -17$ (a simple magnitude threshold, slightly brighter than the faintest galaxies at photometric redshift $\sim$2.3) within the redshift range 0.3–2.3, as indicated in Fig. 4.1. The χ^2 merit function is minimized using the Levenberg-Marquardt method. Data and the derived best-fit function are depicted in Fig. 4.2, while the corresponding parameters

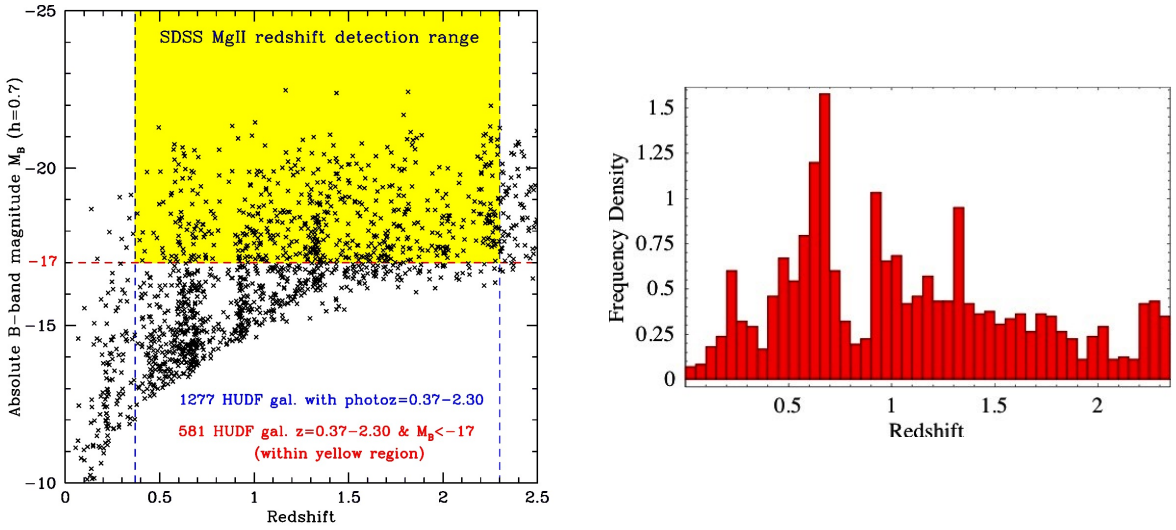

Figure 4.1: The distribution of B-band absolute magnitudes for HUDF galaxies corresponding to a subsample with $i < 28$ is shown in the left-hand panel, while on the opposite side the frequency of galaxy number counts as a function of redshift is presented.

are listed in Table 4.1. The correlation matrix $\boldsymbol{\rho}$ is expressed by:

$$\boldsymbol{\rho} = \begin{pmatrix} 1 & 0.88 & 0.51 & -0.58 & 0.53 \\ 0.88 & 1 & 0.15 & -0.79 & 0.82 \\ 0.51 & 0.15 & 1 & 0.36 & -0.36 \\ -0.58 & -0.79 & 0.36 & 1 & -0.96 \\ 0.53 & 0.82 & -0.36 & -0.96 & 1 \end{pmatrix}, \tag{4.16}$$

where the indices of ρ_{ij} refer to the parameters in the following order: $(\Phi_{*,o}, M_{*,o}, \alpha, p, q)$.

Table 4.1 includes results from the FORS (FOcal Reducer and low dispersion Spectrograph) Deep Field (FDF) [Heidt et al. 2003], which is statistically more robust because it covers an area 4–5 times larger than the HUDF (though it is about 2 mag shallower, in the i-band). The comparison of HUDF with FDF luminosity function best-fit parameters shows that results are consistent within error bars [Gabasch et al. 2004].

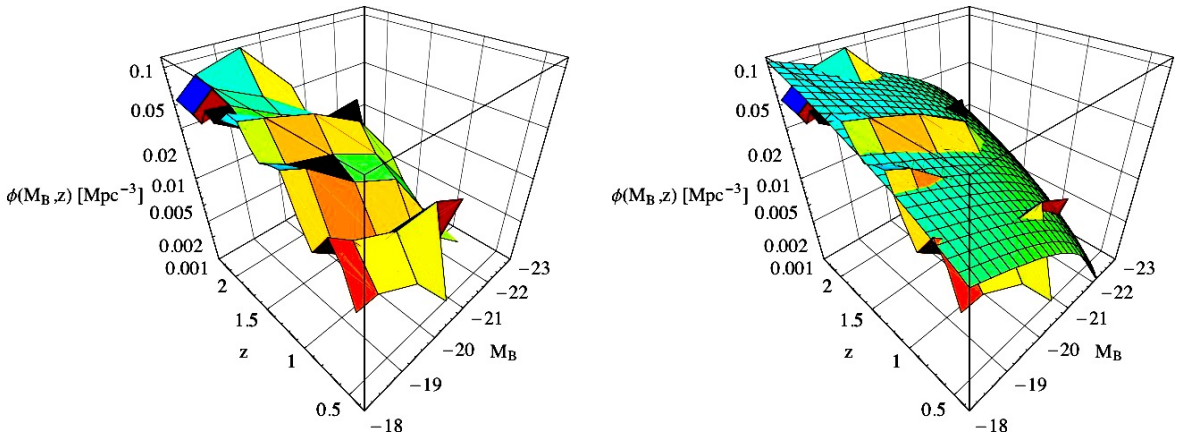

Figure 4.2: The number counts of galaxies with redshift in the interval 0.3–2.3 as a function of redshift and absolute magnitude is shown on the left-hand side, while in the right-hand panel the same distribution is plotted together with the best-fit luminosity function surface.

Table 4.1: The best-fit parameters for the luminosity function of HUDF galaxies with redshift within 0.3–2.3, derived herein adopting absolute magnitudes and photometric redshifts from [Cameron & Driver 2007], are listed together with the respective asymptotic standard errors. Results are compared with those from the FORS Deep Field (FDF) [Gabasch et al. 2004], listed in the second column of the table.

Parameters	HUDF	FDF
$\Phi_{*,o}$ (Mpc^{-3})	0.0057±0.0047	$0.0082^{+0.0014}_{-0.0012}$
$M_{*,o}$	-21.01±1.71	$-20.92^{+0.32}_{-0.25}$
α	-1.33±0.10	-1.24±0.04
p	-1.69±0.95	$-1.27^{+0.16}_{-0.19}$
q	1.42±2.15	$0.95^{+0.21}_{-0.26}$

4.2.2 Absorber Cross-Section and its Evolution

The knowledge of the average incidence of MgII absorbers as a function of redshift and absorption strength from SDSS QSOs, combined with observations of a sample of galaxies

complete to $M_B \sim -17$ in the same redshift range from HUDF, provides information to constrain the cross-section of absorbing galaxies.

The basic assumption of this approach is that the large-scale average statistics from the SDSS applies to the HUDF as well. Of course, it is not possible to derive a one-to-one correspondence between HUDF galaxies and absorption features, and only average results can be obtained. Such a comparative study makes sense only if the large-scale distribution of gas and galaxies in the SDSS and HUDF reflects average properties of the Universe.

In order to assure a connection with reality and reduce parameter degeneracy, certain parameters of the cross-section model have been set to values from the literature: $\beta = 0.2$, $L_{\rm min} = 0.05 L_*$, and $K\epsilon\kappa = 0.5$ (see [Steidel et al. 1994, Tripp & Bowen 2005] and comments in § 1.2.1). Note that all of the parameters are meant in the average sense, i.e., averaged over all morphological types and redshifts.

Computing $R_*(z)$ from Eq. 4.14 under observational constraints from SDSS MgII statistics (Eq. 2.6) and HUDF galaxy luminosity function (Table 4.1), the best-fit set of parameters for an evolving absorbing cross-section (described by Eq. 4.15) is presented in Table 4.2 for various minimum REW thresholds, from 0.3 Å to 3.5 Å. However, note that the listed uncertainties do not include those originating from luminosity function parameters or any other observational constraints (such as β, $L_{\rm min}$, $K\epsilon\kappa$).

Table 4.2 suggests clearly two trends: (i) an increase of the evolutionary parameter γ with larger REW thresholds and (ii) a decrease of the characteristic halo size of L_* absorbing galaxies at stronger REW, consistent with the results in Chapter 3.

The covariance between the fitted parameters $R_{*,o}$ and γ is visualized in Fig. 4.3, depicting ellipsoidal joint confidence regions for 68% and 95% confidence levels with REW thresholds ranging from 0.3 Å to 3.5 Å.

The absorption incidence resulting from the fitted evolving cross-section model is compared with the non-evolving case in Fig. 4.4 for the same REW intervals. Non-evolutionary curves are dashed, while evolving ones are plotted with a solid line.

Table 4.2: Best-fit parameters for an evolving cross-section model $R_*(z) = R_{*,o}(1+z)^\gamma$ are listed for several REW thresholds, assuming previously obtained parameters for the HUDF galaxy luminosity function and MgII absorption incidence. Further observational constraints include $\beta = 0.2$, $L_{\rm min} = 0.05L_*$, and $K\epsilon\kappa = 0.5$. Errors on parameters beyond the ones listed in this Table are not included.

REW	$R_{*,o}$ (kpc)	γ
> 0.3 Å	$60.2^{+2.6}_{-2.5}$	0.82±0.06
> 0.6 Å	$43.0^{+1.9}_{-1.8}$	0.92±0.06
> 1.0 Å	$30.2^{+1.7}_{-1.7}$	1.01±0.07
> 1.5 Å	$20.6^{+1.2}_{-1.2}$	1.06±0.08
> 2.0 Å	$13.6^{+0.9}_{-0.9}$	1.15±0.09
> 2.5 Å	$8.6^{+1.1}_{-0.9}$	1.31±0.15
> 3.0 Å	$5.6^{+0.9}_{-0.8}$	1.45±0.19
> 3.5 Å	$3.3^{+0.7}_{-0.6}$	1.65±0.24

4.3 AN IMPROVED ABSORBING GALAXY MODEL

A physical model describing the nature of MgII absorbers is likely to involve a mixture of various kinematics, and disentangling the different contributions is difficult because of degeneracy effects. A statistical approach to the modeling of MgII absorbers is presented in this section, and a solution for the absorption REW as a function of galaxy impact parameter, luminosity, and redshift is achieved analytically under the observational constraints from SDSS and HUDF.

The statistical nature of the model implies that it can only provide a description of average galaxy and absorption properties. Nevertheless, an empirically defined relation may form a versatile reference for development of physical models which are consistent with observations.

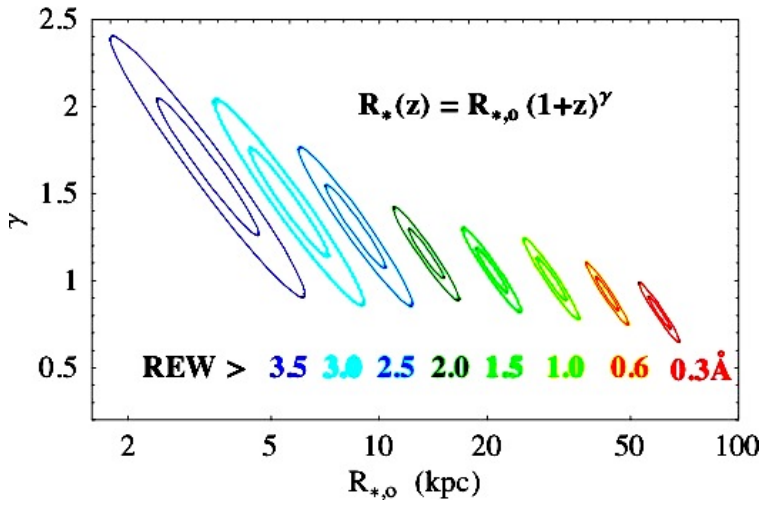

Figure 4.3: Ellipsoidal joint confidence regions of cross-section parameters $R_{*,o}$ and γ are shown with REW thresholds ranging from 0.3 Å to 3.5 Å, for 68% and 95% confidence levels.

4.3.1 Modeling Absorption REW as a Function of Impact Parameter, Luminosity, and Redshift

The improvement introduced by the new model is due to the inclusion of REW dependence on galaxy impact-parameter, following results suggesting that the two quantities are related (see Chapter 3). The goal of this section is to find a solution for $W(x|L,z)$, i.e. the absorption REW W as a function of projected distance x between a sight-line and the center of a galaxy of luminosity L and redshift z.

The REW distribution is assumed to be generally described in terms of a Schechter function (adopted by [Prochter et al. 2006])

$$\frac{\partial^2 n_{abs}}{\partial z\,\partial W} = \frac{N_*(z)}{W_*(z)} \left(\frac{W}{W_*(z)}\right)^{\delta} \exp\left(-\frac{W}{W_*(z)}\right), \tag{4.17}$$

which simplifies to Eq. 2.3 for $\delta = 0$ (employed by [Nestor et al. 2005a]).

In order to constrain the statistical model with the observed dn/dz and dn/dW at all redshifts, the best-fit REW distribution of SDSS absorbers is set to arise from imaginary

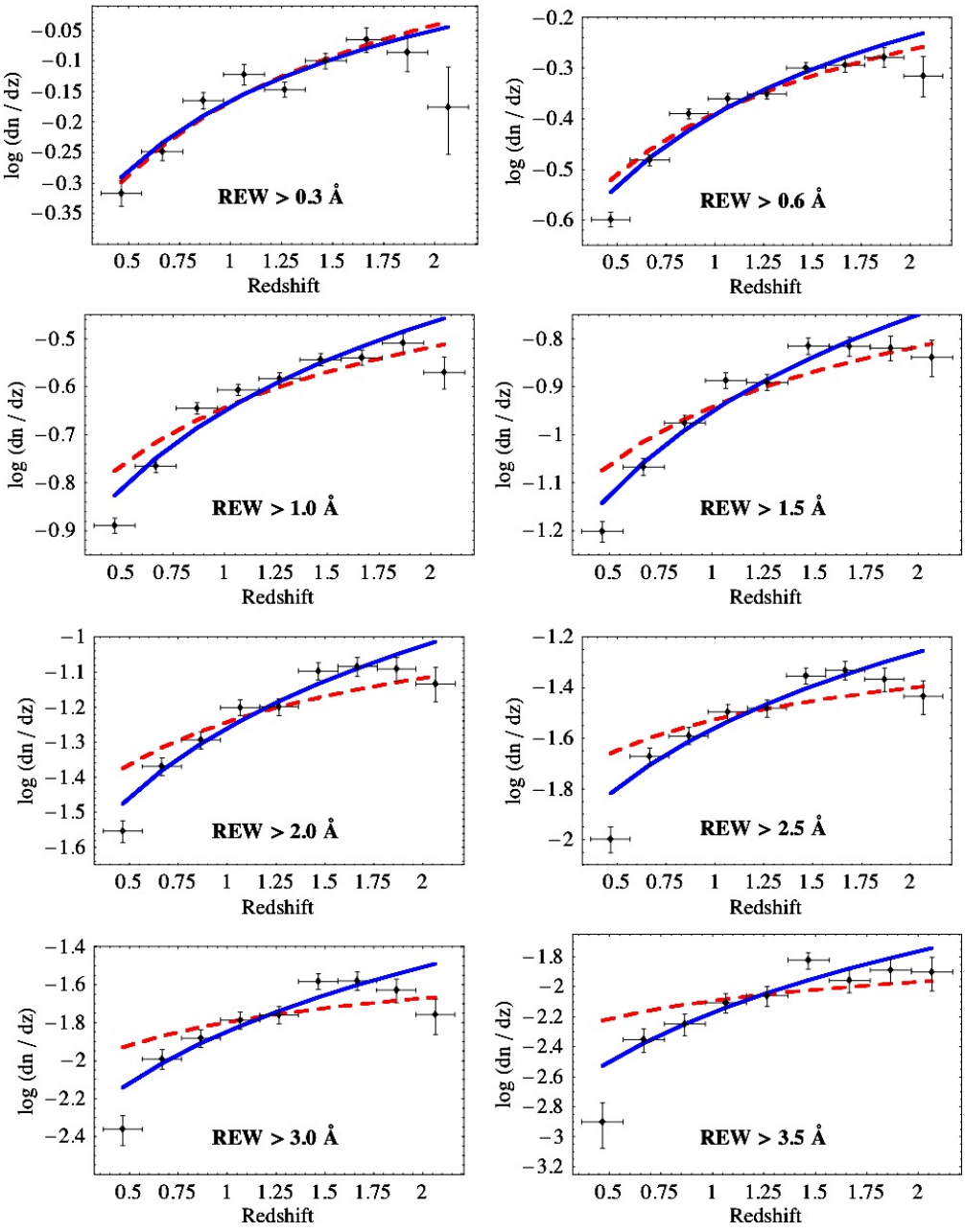

Figure 4.4: The observed number density of absorbers with REW greater than thresholds from 0.3 Å to 3.5 Å is shown together with best-fitting curves describing non-evolving cross-section models (red dashed lines) and evolving scenarios (blue solid lines).

QSO sight-lines intercepting HUDF galaxies with cross-sections parametrized as in § 4.2.2:

$$\frac{\partial^2 n_{gal}}{\partial z\,\partial W} = \frac{\partial^2 n_{abs}}{\partial z\,\partial W}, \tag{4.18}$$

assuming that each absorbing galaxy generated a distribution of REW depending on the luminosity and distance from their center. Eq. 4.18 is written more explicitly as follows:

$$\frac{\partial l}{\partial z}\int_0^\infty \Phi(L|z)\,p(W|L,z)\,dL = \frac{N_*(z)}{W_*(z)}\left(\frac{W}{W_*(z)}\right)^\delta \exp\left(-\frac{W}{W_*(z)}\right), \tag{4.19}$$

where $p(W|L,z)$ defines the contribution to the cross-section from galaxies of luminosity L and redshift z generating absorption lines of REW W, per unit REW interval:

$$p(W|L,z) = -\frac{\partial\tilde{s}(>W|L,z)}{\partial W}. \tag{4.20}$$

The cross-section $\tilde{s}(>W|L,z)$ of a galaxy of given luminosity L and redshift z causes absorption lines with REW greater than W, and it is related to the projected distance x from the center of the galaxy as

$$\tilde{s}(>W|L,z) = K\tilde{\epsilon}(L|z)\kappa\,\pi\,x^2(W|L,z). \tag{4.21}$$

Note the additional dependence of the cross-section $\tilde{s}$ on the REW, with respect to the simple model described by Eq. 4.9. Also, $\tilde{s}$ may include elliptical cross-sections through the correcting geometrical factor $\tilde{\epsilon}$. The negative sign in Eq. 4.20 is chosen to impose $\partial\tilde{s}(>W)/\partial W < 0$, according to results indicating larger cross-sections for weaker absorbers with respect to stronger ones (see § 3.1.4.2).

Multiplying both sides of Eq. 4.19 by $(W/W_*)^{-\delta}\exp(W/W_*)$, the right-hand side does not depend on W anymore. Then, assuming $\tilde{s}$ is separable as follows

$$\tilde{s}(>W|L,z) = s(L|z)\,r(>W|z), \tag{4.22}$$

$r(>W|z)$ can be solved by

$$\frac{\partial}{\partial W}\left[\left(\frac{W}{W_*(z)}\right)^{-\delta}\exp\left(\frac{W}{W_*(z)}\right)\frac{\partial r(>W|z)}{\partial W}\right] = 0, \tag{4.23}$$

which leads to

$$r(>W|z) = A(z)\,\Gamma\left(1+\delta, \frac{W}{W_*(z)}\right) + B(z), \tag{4.24}$$

where $A(z)$ and $B(z)$ are integration constants (independent of W). Since Eq. 4.20 depends only on $\partial r/\partial W$, the value of $B(z)$ can be constrained by direct observations, but it does not affect the measured incidence. Substituting

$$\frac{\partial r}{\partial W} = -\frac{A(z)}{W_*(z)}\left(\frac{W}{W_*(z)}\right)^{\delta}\exp\left(-\frac{W}{W_*(z)}\right) \tag{4.25}$$

into Eq. 4.19, the latter becomes:

$$\frac{\partial l}{\partial z}\int_0^{\infty}\Phi(L|z)\,s(L|z)\,A(z)\,dL = N_*(z). \tag{4.26}$$

Assuming for simplicity that the fraction of galaxies $\tilde{\epsilon}(L|z)$ participating in the absorption at a given redshift z is ϵ for $L \in (L_{\rm min}(z), L_{\rm max}(z))$ and zero otherwise,

$$\tilde{\epsilon}(L|z) = \epsilon H[L - L_{\rm min}(z)]\,H[L_{\rm max}(z) - L], \tag{4.27}$$

then Eq. 4.26 can be solved for $A(z)$:

$$A(z) = \left(\frac{K\epsilon\kappa\,\pi\,R_*^2(z)\,\Phi_*(z)\,\Xi(z)}{N_*(z)}\,\frac{dl}{dz}\right)^{-1}. \tag{4.28}$$

Using Eqs. 4.22, 4.24 and 4.28, it follows that

$$\frac{\partial\tilde{s}}{\partial W} = -\frac{N_*(z)\,H[L - L_{\rm min}(z)]\,H[L_{\rm max}(z) - L]}{W_*(z)\,\Phi_*(z)\,\Xi(z)}\left(\frac{L}{L_*(z)}\right)^{2\beta}\left(\frac{dl}{dz}\right)^{-1}\left(\frac{W}{W_*(z)}\right)^{\delta}\exp\left(-\frac{W}{W_*(z)}\right). \tag{4.29}$$

Note that $\partial\tilde{s}/\partial W$ does not depend on $K\epsilon\kappa$ and $R_*(z)$, since they are just constant factors (independent of W or L) absorbed by the integration constant $A(z)$, as a consequence of the assumption in Eq. 4.22. In that case, $p(W|L,z)$ is proportional to the REW distribution described by Eq. 4.17 and from Eq. 4.29 it follows that

$$p(W|L,z) = \frac{1}{\Phi_*(z)\,\Xi(z)}\left(\frac{L}{L_*(z)}\right)^{2\beta}\left(\frac{dl}{dz}\right)^{-1}\frac{\partial^2 n_{abs}}{\partial z\,\partial W}\,H[L - L_{\rm min}(z)]\,H[L_{\rm max}(z) - L]. \tag{4.30}$$

The contribution of galaxies of luminosity L to the incidence of absorbers with REW W at redshift z is evaluated from the following expression

$$\frac{\partial^3 n}{\partial z\,\partial W\,\partial L} = \frac{dl}{dz}\,\Phi(L|z)\,p(W|L,z), \tag{4.31}$$

which is shown in Fig. 4.5–4.6 at fixed redshifts from 0.5 to 2, after adopting the previously obtained best-fit parameters for the HUDF galaxy luminosity function (Table 4.1) and the SDSS absorption incidence (Eq. 2.6).

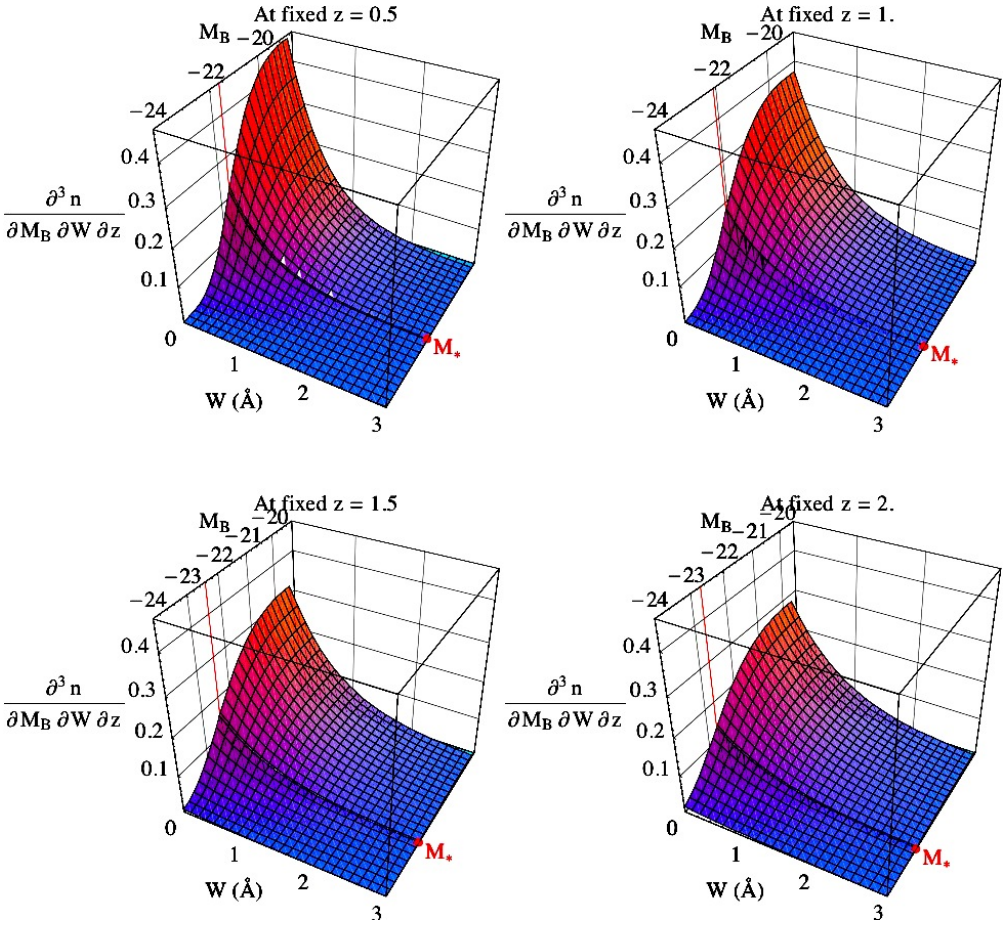

Figure 4.5: Plot of $\partial^3 n/\partial z \partial W \partial L$ at fixed redshifts 0.5, 1, 1.5, and 2 (from top-left to bottom-right), assuming previously obtained best-fit parameters for the HUDF galaxy luminosity function (Table 4.1) and the SDSS absorption incidence (Eq. 2.6). Further observational constraints include $\beta = 0.2$ and $L_{\rm min} = 0.05 L_*$. The dashed/shaded line at constant M_B enhances the trend at the characteristic magnitude $M_{B,*}(z)$.

Recalling Eq. 4.21, it follows that

$$\frac{\partial \tilde{s}}{\partial x} = 2K\epsilon\kappa\pi x \, H[L - L_{\rm min}(z)] \, H[L_{\rm max}(z) - L] \tag{4.32}$$

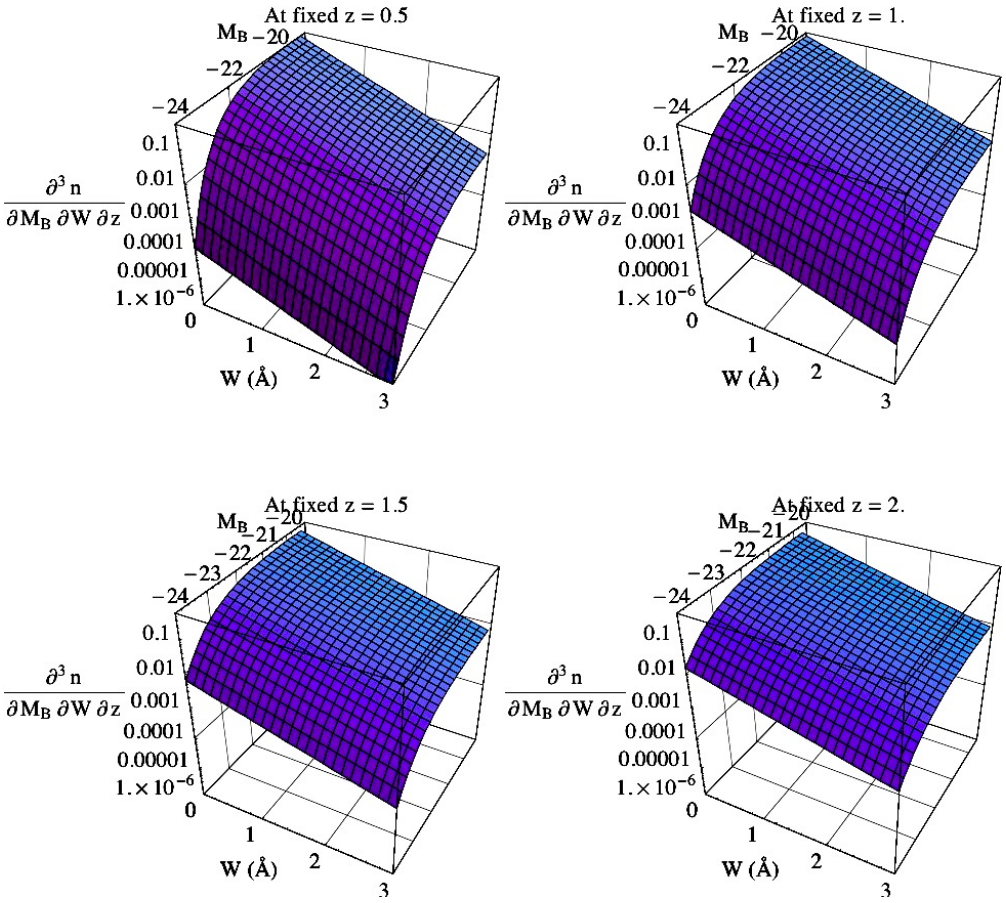

Figure 4.6: Same as Fig. 4.5, but with a logarithmic scale to enhance the small REW trend.

and substituting Eq. 4.29 into

$$\frac{\partial \tilde{s}}{\partial W} = \frac{\partial \tilde{s}}{\partial x}\,\frac{\partial x}{\partial W}, \tag{4.33}$$

the following expression results:

$$\frac{\partial W}{\partial x} = -2K\epsilon\kappa\pi\, x\, \frac{W_*(z)\,\Phi_*(z)\,\Xi(z)}{N_*(z)}\,\frac{dl}{dz}\left(\frac{L}{L_*(z)}\right)^{-2\beta}\left(\frac{W}{W_*(z)}\right)^{-\delta}\exp\left(\frac{W}{W_*(z)}\right). \tag{4.34}$$

In the particular case of $\delta = 0$ (as assumed in Eq. 2.3 and by [Nestor et al. 2005a]), W may be solved for as follows:

$$W(x|L,z) = W_*(z)\,\ln\left\{\left[F(L,z) + \left(\exp\left(-\frac{W_{\rm min}}{W_*(z)}\right) - F(L,z)\right)\frac{x^2}{\tilde{R}^2(L,z)}\right]^{-1}\right\}, \tag{4.35}$$

which is defined for impact parameters x smaller than the maximum radius of the absorber $\tilde{R} = x(W_{\rm min})$, whose value depends on the minimum REW threshold $W_{\rm min}$ derived from observations:

$$\tilde{R}(L,z) = \tilde{R}_*(L,z) \left(\frac{L}{L_*(z)} \right)^{\beta}, \tag{4.36}$$

with

$$\tilde{R}_*(L,z) = \left[\frac{\exp\left(-\frac{W_{\rm min}}{W_*(z)}\right) - F(L,z)}{K \epsilon \kappa \, \pi \, \frac{dl}{dz} \, \Phi_*(z) \, \Xi(z) / N_*(z)} \right]^{1/2}. \tag{4.37}$$

The integration constant (independent of x) $F(L,z)$ is related to the maximum REW corresponding to sight-lines passing through the center of absorbing galaxies. Solving Eq. 4.35 for $F(L,z)$ in the case of a line-of-sight passing through the center of the absorber ($x = 0$) and setting $W_{\rm max}(L,z) \equiv W(x=0|L,z)$, considering W is monotonically decreasing with x,

$$F(L,z) = \exp\left(-\frac{W_{\rm max}(L,z)}{W_*(z)} \right) \tag{4.38}$$

results.

In order to replace the dependence of Eq. 4.37 on $N_*(z)$ with that on the less noisy dn/dz for absorption lines stronger than a minimum REW threshold $W_{\rm min}$, it is realized that:

$$\left.\frac{dn}{dz}\right|_{W>W_{\rm min}} = \int_{W_{\rm min}}^{\infty} \frac{\partial^2 n}{\partial z \, \partial W} \, dW = \frac{N_*(z)}{W_*(z)} \int_{W_{\rm min}}^{\infty} \left(\frac{W}{W_*(z)} \right)^{\delta} \exp\left(-\frac{W}{W_*(z)} \right) dW$$

$$= N_*(z) \, \Gamma\left(1+\delta, \frac{W_{\rm min}}{W_*(z)} \right). \tag{4.39}$$

For the case of $\delta = 0$,

$$N_*(z) = \exp\left(\frac{W_{\rm min}}{W_*(z)} \right) \left.\frac{dn}{dz}\right|_{W>W_{\rm min}} \tag{4.40}$$

results, and the expression for $\tilde{R}_*(L,z)$ becomes

$$\tilde{R}_*(L,z) = \left\{ \frac{\left[1 - \exp\left(-\frac{W_{\rm max}(L,z) - W_{\rm min}}{W_*(z)} \right) \right] \left.\frac{dn}{dz}\right|_{W>W_{\rm min}}}{K \epsilon \kappa \, \pi \, \Phi_*(z) \, \Xi(z) \, \frac{dl}{dz}} \right\}^{1/2}. \tag{4.41}$$

Unlike the simple model presented in § 4.1.2, $\tilde{R}_*(L,z)$ depends on luminosity since $F(L,z)$ has been introduced. If $W_* \ll W_{\rm max}(L,z)$, then $F(L,z)$ becomes negligible and $\tilde{R}_*(L,z) \approx R_*(z)$ as in the simple case (see Eq. 4.14).

4.3.2 General Comments on the New Model

In order to illustrate possible trends of $W(x|L,z)$ (all fitting the measured incidence of absorbers), simple relations for $W_{\rm max}(L,z)$ are chosen. The solution for REW (Eq. 4.35) as a function of impact parameter and absolute magnitude is plotted in Fig. 4.7–4.9, assuming previously obtained best-fit parameters for the HUDF galaxy luminosity function (Table 4.1) and the SDSS absorption incidence (Eq. 2.6) and three different models for $W_{\rm max}(L,z)$:

(i) $W_{\rm max}(L,z) = 10$ Å (shown in Fig. 4.7),

(ii) $W_{\rm max}(L,z) = 3W_*(z)\,(L/L_*(z))^{\gamma}$ (shown in Fig. 4.8),

(iii) $W_{\rm max}(L,z) = 3W_*(z)\,(L/L_*(z))^{-\gamma}$ (shown in Fig. 4.9),

setting $\gamma = 0.3$ and $z = 1$.

Since absorbers from galaxies of luminosity L and redshift z are detectable if and only if $W_{\rm max}(L,z) > W_{\rm min}$, a lower [upper] limit for $L_{\rm min}(z)$ [$L_{\rm max}(z)$] arises when the sign of $\partial W_{\rm max}/\partial L$ is positive [negative], as it can be inferred from Fig. 4.8–4.9.

Values for $W_{\rm max}(L,z)$, $L_{\rm min}(z)$, $L_{\rm max}(z)$, and β should be constrained by direct imaging of galaxies with known absorption. Of course, observational data are expected to be scattered around the statistical model for $W(x|L,z)$, which averages over all galaxy types with the same luminosity at a given redshift.

Independent of the form of $W_{\rm max}(L,z)$, the solution for $W(x|L,z)$ is consistent with measurements of greater REWs at smaller impact parameters (as indicated by Table 4.2 and [Lanzetta & Bowen 1992, Steidel 1993]), as well as the observed correlation between larger impact parameters and brighter galaxies [Steidel 1993, Steidel et al. 1994], believed to be real because they are opposite to that predicted by potential selection effects due to the QSO glare (see § 3.1.3).

Results from Chapter 3 indicate that fainter and bluer galaxies contribute marginally more than luminous galaxies to stronger absorption lines. Unfortunately, these results are based on apparent magnitudes only, so they do not constrain $W_{\rm max}(L,z)$. However, since average absorption redshifts do not appear to increase at larger REW, possible justifications of the observed brightness–REW trend in terms of a relation between REW and redshift are ruled out. Instead, a decreasing $W_{\rm max}(L,z)$ at brighter luminosities can explain the

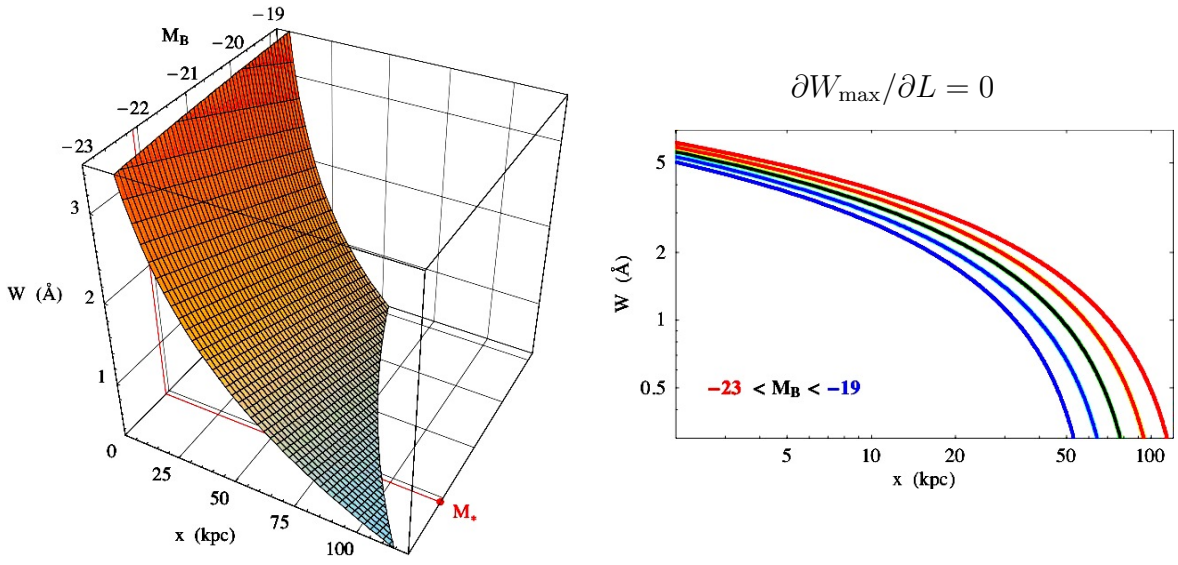

Figure 4.7: Plot of $W(x|L,z)$ assuming previously obtained best-fit parameters for the HUDF galaxy luminosity function (Table 4.1) and the SDSS absorption incidence (Eq. 2.6) at fixed redshift $z = 1$ and $W_{\rm max}(L,z) = 10$ Å. Further observational constraints include $W_{\rm min} = 0.3$ Å, $\beta = 0.2$, $L_{\rm min} = 0.05L_*$, and $K\epsilon\kappa = 0.5$.

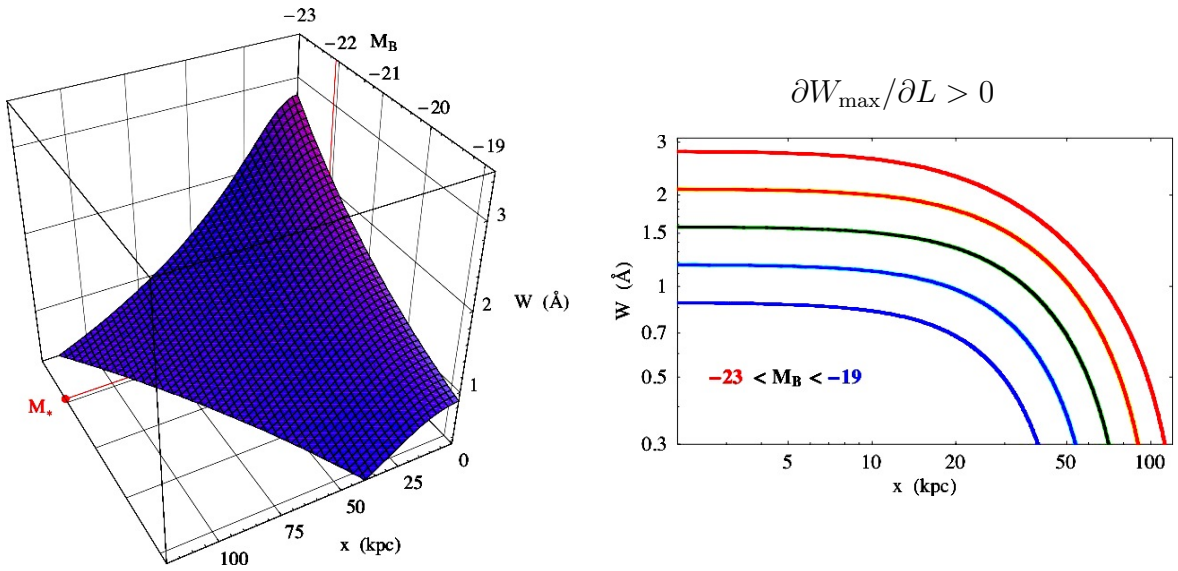

Figure 4.8: Same as Fig. 4.7, but assuming $W_{\rm max}(L,z) = 3W_*(z)\,(L/L_*(z))^{0.3}$.

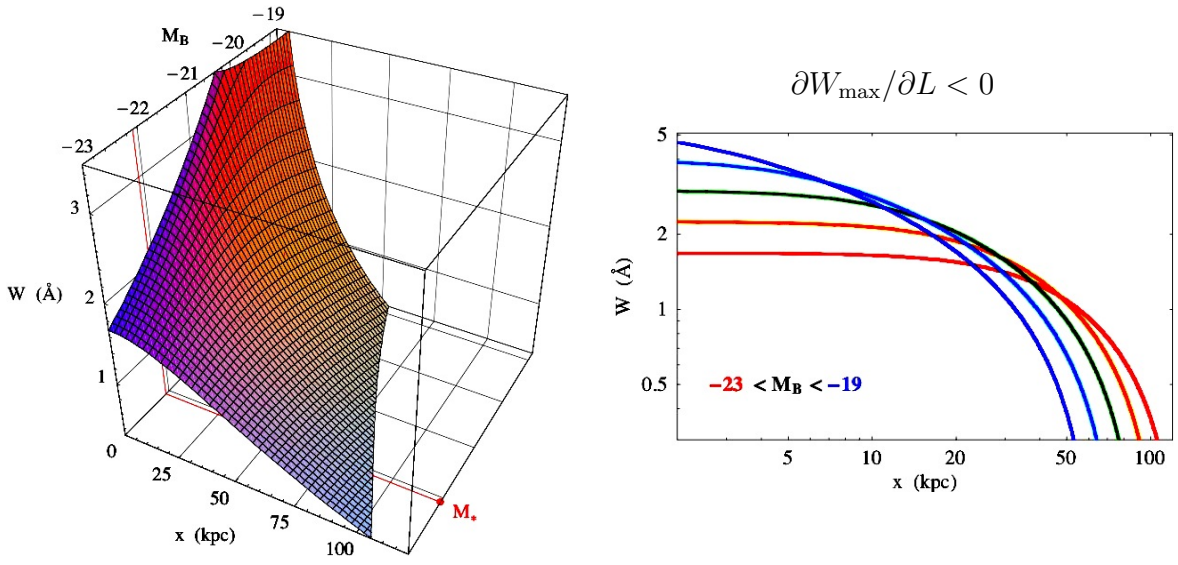

Figure 4.9: Same as Fig. 4.7, but assuming $W_{\max}(L,z) = 3W_*(z)\,(L/L_*(z))^{-0.3}$.

association of stronger absorbers with fainter galaxies, as illustrated in Fig. 4.9.

Also, Fig. 4.9 shows that data points are expected to be scattered around $W(x|L,z)$ not only because of different galactic morphologies with the same luminosity and uncertainties of the adopted parameters, but also as a consequence of luminosity degeneracy over a large range of impact parameters (which may further justify the difficulty of correlating absorption properties with galaxy properties [Churchill et al. 2000b]). However, the model indicates that such a degeneracy may be broken and systematic trends are expected to arise if the absorption strength is correlated with absorbing galaxies at very small and very large impact parameters.

4.3.3 On Weak Absorbers

On a more speculative note, could weak absorbers (with REW<0.3 Å) follow from extrapolating the above described model? Some reasons arguing against this include the uncertain association with galaxies and a steeper incidence of $\partial n/\partial W$ [Nestor et al. 2005a]. However, weak absorbers might arise as "end products" of strong absorbers as follows. Galactic winds may originate from stellar formation activities and sweep-up interstellar gas during the initial

fast and dense regime (consistent with the strong kinematics and small impact parameters expected for large REW absorbers). As winds lose speed and drag material into the galactic halo, gas may accumulate and also be subject to various interactions (from dwarf satellite galaxies, nearby galaxies, intergalactic medium, etc.) which weaken its association with the original galaxy. Such an environment agrees with the expectations for weak absorbers, which are preferentially found within older and redder galaxies, with less dense and more irregular and fragmented halo gas distribution.

4.3.4 Future Prospects

Although this new model is only statistical in nature, some of its features are expected to be constrained by ongoing surveys reaching deeper imaging of galaxies around MgII absorbers detected in SDSS QSO sight-lines (e.g., see § 5.2.2). The versatility of an analytical model, which is set to be consistent with the measured incidence of absorbers, offers a useful test bed for evaluating the statistical properties of physical models.

For example, the kinematical evolution of superwinds may explain why stronger absorbers are associated with bluer (younger) environments at smaller impact parameters, while weaker systems tend to be related to redder (older) galaxies at larger projected distances. The statistical model for $W(x|L,z)$ might arise from a relation between galactic outflow speed and distance from a galaxy's center. It is likely that studying galactic winds and QSO absorbers in synergy may help achieve a deeper understanding of their origins and properties.

5.0 CONCLUSIONS

5.1 SUMMARY

In this thesis, the quest into the nature of strong MgII absorbers was pursued by taking advantage of the largest catalog of MgII absorbers to date from SDSS DR4 QSO spectra. Three different but complementary approaches were employed, as summarized below.

5.1.1 Absorption Line Statistics (Chapter 2)

From the analysis of 44,606 SDSS DR4 QSOs with magnitude $i < 20$ and redshift $z > 0.36$, 14,536 MgII absorbers were detected in 11,139 sight-lines, with rest-equivalent width (REW) ranging from 0.16 Å to 8.5 Å. Dust reddening and gravitational lensing effects were neglected. The number density distribution of MgII absorbers as a function of REW and redshift was computed, and it agreed with prior results from the Early Data Release [Nestor et al. 2005a].

The distribution of 6,061 absorbers, detected in 2,664 QSO sight-lines with multiple systems, was studied by evaluating the two-point correlation function as a function of REW and absorption redshift intervals, for different minimum velocity separations. Line blending was believed to suppress the correlation signal for velocity separations of at least 300 km s^{-1}. Clustering signals were detected from the two-point correlation function for absorber-absorber pairs separated by less than ∼500 km s^{-1}. The signal strength was found to be larger for lower redshift absorbers ($z_{abs} < 1$), as well as for stronger systems (with REW>1.5 Å). These findings were consistent with the expected growth of clustering at lower redshift, and indicated possible association of clustered MgII absorbers on either galaxy-group scales or line-of-sight velocity dispersions typical of galaxy clusters. The con-

volution of peculiar velocities in redshift measurements allowed freedom in the interpretation of clustering in terms of spatial distributions and/or kinematic effects.

One unexpected result was the anti-correlation feature at $\sim$1000 km s^{-1}, suggesting that high-velocity galaxies (e.g., in high-eccentricity orbits) or galaxies in the outer regions of clusters were deficient in gas content. If the former case corresponds to reality, ram pressure stripping was conjectured to have played a role.

5.1.2 Absorber-Galaxy Association (Chapter 3)

The spectroscopic catalog of MgII absorbers was cross-correlated with the SDSS imaging catalog of galaxies surrounding QSO sight-lines. In order to avoid biasing effects, only QSO sight-lines with one and only one MgII detection were considered. Absorbers were separated owing to REW and redshift intervals, and galaxy samples with and without setting a magnitude threshold ($r < 21.5$) were adopted. For reference purposes, two control samples of QSOs (random and non-absorbing) were created by matching simultaneously the i-band magnitude and redshift of absorbed QSOs within small intervals. The QSO glare caused incomplete galaxy detection depending on the QSO brightness, the galaxy magnitude, and the QSO–galaxy angular separation. A method to correct for QSO glare effects and possible statistical biases arising from them was developed.

Averaged galaxy number density distributions and QSO-galaxy cross-correlations were computed for various subsets in redshift and REW (with and without setting a magnitude threshold for galaxies) as a function of angle and impact parameter from QSO lines-of-sight. Due to the SDSS shallow galaxy imaging, redshift evolution could not be assessed and most of the results focused on the lowest redshift interval 0.37–0.55. The chance of detecting a galaxy within 10 arcsec of QSO sight-lines almost doubled when MgII absorption was detected in the above mentioned redshift interval, and it was even higher for stronger absorbers. Such a trend was enhanced when only galaxies brighter than $r = 21.5$ were considered. The QSO-galaxy cross-correlation signal was stronger and steeper at small impact parameters for larger REW systems. A weak MgII–star association was found and it was interpreted in terms of faint galaxies misclassified as stars.

A derivation of the luminosity function for absorbing galaxies by a background subtraction technique was attempted in the redshift range 0.37–0.55, but only the bright end ($M_r < -21$) of the luminosity distribution was recovered, because of the shallow galaxy imaging of the SDSS.

Comparing average integrated fluxes of absorbing versus reference galaxies suggested that weak and strong absorbers were associated with more and less luminous galaxies than on average, respectively. Average colors of absorbing galaxies (after removing the contribution from reference galaxies) indicated a bimodal color distribution, about one magnitude bluer in the $u - g$ color and redder in the $i - z$ color, with respect to random as well as non-absorbing reference galaxies. The introduction of a magnitude threshold ($r < 21.5$) slightly decreased the average magnitude offset between absorbing and reference galaxies, as expected from a more contaminated galaxy sample. Such a result agreed with recent findings [Zibetti et al. 2007] which argued that strong absorbers were associated with bluer star-forming galaxies, while weak systems were related to redder and older galaxies. This depicted scenario was further supported by the measured luminosity offset between weak and strong absorbers, as well as by the QSO-galaxy cross-correlation function, suggesting that weaker absorbers were more common at larger impact parameters (at least within the picture of galactic wind kinematics, where longer times are needed to reach larger distances from galactic centers). However, it was recognized that environmental factors might contribute to the observed properties of galaxies associated with MgII absorbers as well.

5.1.3 High-Redshift Galaxies as Absorbers (Chapter 4)

The role of high-redshift galaxies as absorbers was investigated via an indirect method by joining the SDSS MgII statistics with HUDF galaxies, assuming they both represented average properties of the Universe. The luminosity function for HUDF galaxies with $M_B < -17$ and in the redshift range 0.3–2.3 was derived, adopting photometric redshifts and absolute magnitudes from [Cameron & Driver 2007]. Results agreed with those obtained from the FORS Deep Field [Gabasch et al. 2004]. After applying the obtained luminosity function to a simple absorption cross-section model for different REW threshholds, it was deduced that

the redshift evolution increased while gaseous halo sizes decreased at greater REWs.

Results from Chapter 3 suggested that the absorption REW depended on the projected distance of galaxies from QSO sight-lines. An improved statistical model for MgII absorption cross-section depending on both luminosity and REW was proposed. The model was formulated analytically by setting the measured incidence of SDSS absorbers, as a function of REW and redshift, equal to that of HUDF galaxies intercepted by imaginary QSO sight-lines, whose contribution was quantified according to the new cross-section model. Possible scenarios fitting the observed absorption incidence (Chapter 2) were illustrated, and a family of solutions favored by results from galaxy imaging (Chapter 3) was indicated. New observational tests to break parameter degeneracies were discussed and included observations of absorbing galaxies at very small and very large impact parameters.

5.2 FUTURE PROSPECTS

Improvements in the accuracy and range of the results presented in this thesis are prospected to be achieved by integrating complementary analyses and new data sets (as they become available). A selection of topics of particular interest for the near future is described briefly in the next paragraphs.

5.2.1 Clustering of Absorbers

(i) The evaluation of clustering among absorbers for velocity separations greater than 500 km s^{-1} including both radial and transversal components is planned (as mentioned in § 2.2.7). This study is aimed at probing large scales more accurately (e.g., confirming the suspected anti-correlation feature at $\sim 10^3$ km s^{-1}, if it actually exists) and help remove the ambiguity between cosmological expansion and peculiar motion. Results could then be compared with the galaxy-galaxy correlation function.

(ii) The clustering signal detected at velocity separations less than 500 km s^{-1} is anticipated to be partially resolvable by modeling line-blending as a function of REW. The slope of

the two-point correlation function within this range would prove particularly useful for its implications on the origins of MgII absorbers. In fact, a steep dependence $\sim \Delta v^{-4}$ is predicted for absorption lines arising from supernova driven outflows [Shi 1995], and weighing their contribution is crucial for the development of physical models of absorbers.

(iii) The dependence on environment of the clustering signal of MgII absorbers is prospected to be investigated in the near future by cross-matching absorbing SDSS QSOs with deeper infrared imaging surveys, such as the UKIRT Infrared Deep Sky Survey [Dye et al. 2006, Warren et al. 2007], which is described briefly in the next section.

5.2.2 Galaxy Imaging

The galaxy-absorber association study (Chapter 3) was strongly limited by the shallow SDSS imaging. On the other hand, the HUDF analysis (Chapter 4) provided superior imaging depth, but in a small field which did not overlap the SDSS coverage, which left a high degree of freedom in the absorber model.

To better constrain the galaxy-absorber relation and break some of the model degeneracies, large fields within the footprint of the SDSS but at greater depths are needed. Such a requirement is fulfilled by the ongoing Large Area Survey (LAS) of the UKIRT Infrared Deep Sky Survey [Dye et al. 2006, Warren et al. 2007], which aims to cover about 4,000 square degrees in $YJHK$ bands (reaching $Y \sim 20.2$, $J \sim 19.6$, $H \sim 18.9$, $K \sim 18.2$ for the median 5σ point-source brightness integrated within 2", i.e., approximately 3 mag deeper than 2MASS). The LAS is more sensitive than the SDSS to intermediate redshift galaxies and is less affected by dust extinction of bluer light, which is expected to become appreciable for the strongest MgII absorbers [Prochter et al. 2006, Ménard et al., in prep.]. Incompleteness arising from reddening of QSOs by the dust in absorbing galaxies may then be corrected for as well. Thus, the LAS is expected to probe a larger and more complete sample of galaxies corresponding to the SDSS MgII detections.

The combined data set in the nine optical and infrared bands ($ugrizYJHK$) will result in high-quality photometric redshifts, which will help reduce contamination from galaxies not associated with absorption. More accurate galaxy redshift estimations and fainter magnitude

limits are expected to allow a reliable determination of the luminosity function of MgII absorbing galaxies.

5.2.3 Other Surveys

The ongoing Canada-France-Hawaii Telescope Legacy Survey will overlap about 120 square degrees with the SDSS coverage. It is a smaller area than the LAS, but it has greater depth in *ugriz* bands than SDSS (down to $i \sim 25.5$ in the Wide Synoptic Survey and reaching $r \sim 28.5$ in the Deep Synoptic Survey, though the latter only covers 2 square degrees within the SDSS footprint; the limiting magnitude values assume a signal-to-noise ratio of 5 and a 1.15" aperture).

Another program in progress which may help model the evolution of MgII absorbers is the VIMOS VLT Deep Survey [Le Févre et al. 2005]. It consists in an imaging (including $UBVRIJK$ bands) and spectroscopic survey which aims to measure 10^5 spectra within four 4 square-degree fields (complete down to $I_{AB} \sim 22.5$; smaller but deeper areas reach $I_{AB} \sim 25$), achieving an unparalleled description of galaxy evolution from redshift up to $\sim$5 to the present day, as a function of galaxy type, luminosity, and local environment. Due to the small area covered, the evolution of absorbers could be investigated statistically through an indirect method, similarly to the approach adopted for the HUDF data.

BIBLIOGRAPHY

[Abazajian et al. 2004] Abazajian, K., et al. 2004, AJ, 128, 502

[Adelman-McCarthy et al. 2006] Adelman-McCarthy, J.K., et al. 2006, ApJSS, 162, 38

[Aguirre et al. 2001] Aguirre, A., et al. 2001, ApJ, 560, 599

[Bahcall & Spitzer 1969] Bahcall, J.N., & Spitzer, L.J. 1969, ApJ, 156, L63

[Baldry et al. 2004] Baldry, I.K., et al. 2004, ApJ, 600, 681

[Bergeron 1986a] Bergeron, J. 1986, A&A, 155, L8

[Bergeron & Stasinska 1986] Bergeron, J., & Stasinska, G. 1986, A&A, 169, 1

[Bergeron et al. 1987] Bergeron, J., Kunth. D., & D'Odorico, S. 1987, A&A, 180, 1

[Bergeron & Boissé 1991] Bergeron, J., & Boissé, P. 1991, A&A, 243, 344

[Boksenberg & Sargent 1977] Boksenberg, A., & Sargent, W.L.W. 1977, ApJ, 220, 42

[Bond et al. 2001] Bond, N.A., Churchill, C.W., Charlton, J.C., & Vogt, S.S. 2001, ApJ, 562, 641

[Bouché et al. 2004] Bouché, N., Murphy, M.T., & Péroux, C. 2004, MNRAS, 354, L25

[Bowen et al. 1995] Bowen, D.V., Blades, J.C., & Pettini, M. 1995, ApJ, 448, 634

[Bowen et al. 2001] Bowen, D.V., Tripp, T.M., & Jenkins, E.B. 2001, AJ, 121, 1456

[Budavary & Szalay 2000] Budavari, T., & Szalay, A.S. 2000, ApJ, 120, 1588

[Cameron & Driver 2007] Cameron, E., & Driver, S.P. 2007, MNRAS, 377, 523

[Charlton & Churchill 1996] Charlton, J.C., & Churchill, C.W. 1996, ApJ, 465, 631

[Charlton & Churchill 1998] Charlton, J.C., & Churchill, C.W. 1998, ApJ, 499, 181

[Charlton et al. 2000] Charlton, J.C., & Churchill, C.W. 2000, Enc. Astron. Astrophys., 2366 (also, arXiv:astro-ph/0006002)

[Chen 2005] Chen, H.-W. 2005, Proceedings IAU Colloquium No. 199 (Williams, Shu, Ménard, eds., Cambridge University Press), p. 68

[Chen & Lanzetta 2003] Chen, H.-W., & Lanzetta, K.M. 2003, ApJ, 597, 706

[Churchill et al. 1996] Churchill, C.W., Steidel, C.C., & Vogt, S.S. 1996, ApJ, 471, 164

[Churchill et al. 1998] Churchill, C.W., & Le Brun, V. 1998, ApJ, 499, 677

[Churchill 2000] Churchill, C.W. 2000, ASP Conf. Ser. 200, Clustering at High Redshift (Mazure, Le Fèvre, & Le Brun, eds., San Francisco: ASP), p. 271

[Churchill et al. 2000a] Churchill, C.W., et al. 2000, ApJS, 130, 91

[Churchill et al. 2000b] Churchill, C.W., et al. 2000, ApJ, 543, 577

[Churchill 2001] Churchill, C.W. 2001, ApJ, 560, 92

[Churchill & Vogt 2001] Churchill, C.W., & Vogt, S.S. 2001, AJ, 122, 679

[Churchill et al. 2004] Churchill, C.W., Steidel, C.C., & Kacprzak, G.G. 2004, Workshop on Extraplanar Gas, ASP Conference Series (Braun, ed.)

[Churchill et al. 2005] Churchill, C.W., Kacprzak, G.G., & Steidel, C.C. 2005, Proceedings IAU Colloquium No. 199 (Williams, Shu, Ménard, eds., Cambridge University Press), p. 24

[Coe et al. 2006] Coe, D., et al. 2006, AJ, 132, 926

[Cox et al. 2004] Cox, T.J., Primack, J., Jonsson, P., & Somerville, R. 2004, ApJ, 607, L87

[Crott et al. 1997] Crotts, A.P.S., Burles, S., & Tytler, D. 1997, ApJ, 489, L7

[Cristiani 1987] Cristiani, S. 1987, A&A, 175, L1

[Dinshaw & Impey 1996] Dinshaw, N., & Impey, C.D. 1996, ApJ, 458, 73

[Dye et al. 2006] Dye, S., et al. 2006, MNRAS, 372, 1227

[Ellison et al. 2000] Ellison, S.L., Songaila, A., Schaye, J., & Pettini, M. 2000, AJ, 120, 1175

[Ellison et al. 2003] Ellison, S.L., Mallén-Ornelas, G., Sawicki, M. 2003, ApJ, 589, 709

[Ferguson et al. 2000] Ferguson, H.C., et al. 2000, Ann. Rev. Astron. Astrophys., 38, 667

[Ferrara et al. 2000] Ferrara, A., Pettini, M., & Shchekinov, Y. 2000, MNRAS, 319, 539

[Fruchter & Hook 2002] Fruchter, A.S., & Hook, R.N. 2002, PASP, 114, 144

[Frye et al. 2002] Frye, B., Broadhurst, T., & Benitez, N. 2002, ApJ, 568, 558

[Fukugita et al. 1995] Fukugita, M., Shimasaku, K., & Ichikawa, T. 1995, PASP, 107, 945

[Fukugita et al. 1996] Fukugita, M., Ichikawa, T., Gunn, J.E., Doi, M., Shimasaku, K., & Schneider, D.P. 1996, AJ, 111, 1748

[Furlanetto & Loeb 2003] Furlanetto, S.R., & Loeb, A. 2003, ApJ, 588, 18

[Gabasch et al. 2004] Gabasch, A., et al. 2004, A&A, 421, 41

[Giroux & Shull 1997] Giroux, M., & Shull, S.M. 1997, AJ, 113, 1505

[Gonzalez-Delgado et al. 1998] Gonzalez-Delgado, R., Leitherer, C., Heckman, T., Lowenthal, J., Ferguson, H., & Robert, C. 1998, ApJ, 495, 698

[Gunn & Gott 1972] Gunn, J.E., & Gott, J.R. 1972, ApJ, 176, 1

[Heisler et al. 1989] Haisler, J., et al. 1989, ApJ, 347, 52

[Hansen et al. 2005] Hansen, S.M., McKay, T.A., Wechsler, R.H., & Annis, J. 2005, ApJ, 633, 122

[Heckman & Leitherer 1997] Heckman, T.M., & Leitherer, C. 1997, AJ, 114, 69

[Heckman et al. 2000] Heckman, T.M., Lehnert, M., Strickland, D., & Armus, L. 2000, ApJSS, 129, 493

[Heidt et al. 2003] Heidt, J., et al. 2003, A&A, 398, 49

[Hester 2006] Hester, J.A. 2006, ApJ, 647, 910

[Holmberg 1975] Holmberg, E. 1975, Galaxies and the Universe (Sandage, A.&M., eds., University of Chicago Press), p. 123

[Kunth et al. 1998] Kunth, D., Mas-Hesse, J., Terlevich, E., Terlevich, R., Lequeux, J., & Fall, S.M. 1998, A&A, 334, 11

[Landy & Szalay 1993] Landy, S.D., & Szalay, A.S. 1993, ApJ, 412, 64

[Lanzetta et al. 1987] Lanzetta, K.M., Turnshek, D.A., & Wolfe, A.M. 1987, ApJ, 322, 739

[Lanzetta & Bowen 1990] Lanzetta, K.M., & Bowen, D.V. 1990, ApJ, 357, 321

[Lanzetta & Bowen 1992] Lanzetta, K.M., & Bowen, D.V. 1992, ApJ, 391, 835

[Lanzetta 1993] Lanzetta, K.M. 1993, The environment and evolution of galaxies (Kluwer Academic Publishers), p. 237

[Le Brun et al. 1997] Le Brun, V., Bergeron, J., Boissé, P., & Deharveng, J.M. 1997, A&A, 321, 733

[Le Févre et al. 2005] Le Févre, O., et al. 2005, A&A, 439, 845

[Lequeux et al. 1995] Lequeux, J., Kunth, D., Mas-Hesse, J., & Sargent, W. 1995, A&A, 301, 18

[Lin & Zou 2001] Lin, W.-P., & Zou, Z.-L. 2001, ChJAA, 1, 21

[Lin et al. 2004] Lin, L., et al. 2004, ApJ, 617, L9

[Mac Low & McCray 1988] Mac Low, M.-M., & McCray, R. 1988, ApJ, 324, 776

[Madau et al. 2001] Madau, P., Ferrara, A., & Rees, M.J. 2001, ApJ, 555, 92

[Mandelbaum et al. 2005] Mandelbaum R., et al. 2005, MNRAS, 361, 1287

[Ménard et al., in prep.] Ménard, B., et al., in preparation (arXiv:astro-ph/0706.0898)

[Mo & Miralda-Escude 1996] Mo, H.J., & Miralda-Escude, J. 1996, ApJ, 469, 589

[Nestor et al. 2005a] Nestor, D.B., Turnshek, D.A., & Rao, S.M. 2005, ApJ, 628, 637

[Nestor et al. 2005b] Nestor, D.B., Turnshek, D.A., & Rao, S.M. 2005, Proceedings IAU Colloquium No. 199 (Williams, Shu, Ménard, eds., Cambridge University Press)

[Nestor et al. 2006] Nestor, D.B., Turnshek, D.A., & Rao, S.M. 2006, ApJ, 628, 637

[Nestor et al. 2007] Nestor, D.B., Turnshek, D.A., Rao, S.M., & Quider, A. 2007, ApJ, 658, 185

[Peebles 1980] Peebles, P.J.E. 1980, The Large Scale Structure of the Universe (Princeton University Press, Princeton)

[Petitjean & Bergeron 1994] Petitjean, P., & Bergeron, J. 1994, A&A, 283, 759

[Petitjean 1998] Petitjean, P. Proceedings of the Les Houches school "Formation and Evolution of galaxies", (Le Fevre, Charlot, eds., Springer-Verlag); also, arXiv:astro-ph/9810418

[Pettini et al. 2001] Pettini, M., Shapley, A., Steidel, C., Cuby, J.-G., Dickinson, M., Moorwood, A., Adelberger, K., & Giavalisco, M. 2001, ApJ, 554, 981

[Pettini et al. 2002] Pettini, M., Rix, S., Steidel, C., Adelberger, K., Hunt, M., & Shapley, A. 2002, ApJ, 569, 742

[Phillips 1993] Phillips, A. 1993, AJ, 105, 486

[Pier et al. 2003] Pier, J.R., Munn, J.A., Hindsley, R.B., Hennessy, G.S., Kent, S.M., Lupton, R.H., & Ivezić, Ž. 2003, AJ, 125, 1559

[Poggianti 1997] Poggianti, B.M. 1997, AASS, 122, 399

[Prochter et al. 2006] Prochter, G.E., Prochaska, J.X., & Burles, S.M. 2006, ApJ, 639, 766

[Rao & Turnshek 2000] Rao, S.M., & Turnshek, D.A. 2000, ApJS, 130, 1

[Rao et al. 2003] Rao, S.M., Nestor, D.B., Turnshek, D.A., Lane, W.M., Monier, E.M., & Bergeron, J. 2003, ApJ, 595, 94

[Rao 2005] Rao, S.M. 2005, Proceedings IAU Colloquium No. 199 (Williams, Shu, Ménard, eds., Cambridge University Press), p. 125

[Rao et al. 2005] Rao, S.M., Turnshek, D.A., & Nestor, D.B. 2006, ApJ, 636, 610

[Rauch et al. 1996] Rauch, M., Sargent, W.L.W., Womble, D.S., & Barlow, T.A. 1996, ApJ, 467, L5

[Richards et al. 2002] Richards, G.T., et al. 2002, AJ, 123, 2945

[Rigby et al. 2002] Rigby, J.R., Charlton, J.C., & Churchill, C.C. 2002, ApJ, 565, 743

[Rimoldini et al. 2006] Rimoldini, L.G., Ménard, B., Nestor, D.B., Rao, S.M., Sheth, R.K., Turnshek, D.A., Zibetti, S., Feather, S., & Quider, A. 2006, BAAS, 207, #203.07

[Sahu & Blades 1997] Sahu, M., & Blades, J.C. 1997, ApJ, 484, L125

[Sargent et al. 1980] Sargent, W.L.W., et al. 1980, ApJS, 42, 41

[Sargent et al. 1988a] Sargent, W.L.W., et al. 1988, ApJS, 68, 539

[Sargent et al. 1988b] Sargent, W.L.W., Steidel, C.C., & Boksenberg, A. 1988, ApJ, 334, 22

[Scannapieco et al. 2002] Scannapieco, E., Ferrara, A., & Madau, P. 2002, ApJ, 574, 590

[Schechter 1976] Schechter, P. 1976, ApJ, 203, 297

[Shi 1995] Shi, X. 1995, ApJ, 449, 140

[Steidel & Sargent 1992] Steidel, C.C., & Sargent, W.L.W. 1992, ApJS, 80, 1

[Steidel 1993] Steidel, C.C. 1993, The environment and evolution of galaxies (Kluwer Academic Publishers), p. 263

[Steidel et al. 1994] Steidel, C.C., Dickinson, M., & Persson, S.E. 1994, ApJ, 437, L75

[Steidel 1995] Steidel, C.C. 1995, ESO Workshop on Quasar Absorption Lines (Meylan G., ed.), p. 139

[Stoughton et al. 2002] Stoughton, C., et al. 2002, AJ, 123, 485 (erratum 123, 3487)

[Strickland 1998] Strickland, D.K. 1998, Ph.D. thesis, Univ. Birmingham

[Suchkov et al. 1994] Suchkov, A.A., Balsara, D.S., Heckman, T.M., & Leitherer, C. 1994, ApJ, 430, 511

[Tenorio-Tagle & Munoz-Tunon 1998] Tenorio-Tagle, G., & Munoz-Tunon, C. 1998, MNRAS, 293, 299

[Tomisaka & Bregman 1993] Tomisaka, K., & Bregman, J. 1993, PASJ, 45, 513

[Tripp & Bowen 2005] Tripp, T.M., & Bowen, D.V. 2005, Proceedings IAU Colloquium No. 199 (Williams, Shu, Ménard, eds., Cambridge University Press)

[Tytler et al. 1987] Tytler, D., et al. 1987, ApJS, 64, 667

[Warren et al. 2007] Warren, S.J., et al. 2007, MNRAS, 375, 213

[Williams et al. 1996] Williams, R.E., et al. 1996, ApJ, 112, 1335

[Wolfe 1988] Wolfe, A.M. 1988, Proceedings of the QSO Absorption Line Meeting (Blades, Turnshek, Norman, eds., Cambridge University Press), p. 297

[Zabludoff et al. 1993] Zabludoff, A.I., Geller, M.J., Huchra, J.P., & Vogeley, M.S. 1993, AJ, 106, 1273

[Zibetti et al. 2005] Zibetti, S., Ménard, B.; Nestor, D., & Turnshek, D. 2005, ApJ, 631, L105

[Zibetti et al. 2007] Zibetti, S., et al. 2007, ApJ, 658, 161

[Zonak et al. 2004] Zonak, S.G., Charlton, J.C., Ding, J., & Churchill, C.W. 2004, ApJ, 606, 196